Modelling Three-Dimensional Sound Propagation in Wedge Environments

by

Melanie Elizabeth Austin
B.A.Sc., University of British Columbia, 2001

A Dissertation Submitted in Partial Fulfillment of the
Requirements for the Degree of

DOCTOR OF PHILOSOPHY

in the School of Earth and Ocean Sciences

Modelling Three-Dimensional Sound Propagation in Wedge Environments

by

Melanie Elizabeth Austin
B.A.Sc., University of British Columbia, 2001

SUPERVISORY COMMITTEE

Dr. N. Ross Chapman, Supervisor
(School of Earth and Ocean Sciences, University of Victoria)

Dr. Stan Dosso, Departmental Member
(School of Earth and Ocean Sciences, University of Victoria)

Dr. George Spence, Departmental Member
(School of Earth and Ocean Sciences, University of Victoria)

Dr. Adam Zielinski, Outside Member
(Department of Electrical and Computer Engineering, University of Victoria)

Mr. David Hannay, Additional Member
(JASCO Applied Sciences)

SUPERVISORY COMMITTEE

Dr. N. Ross Chapman, Supervisor
(School of Earth and Ocean Sciences, University of Victoria)

Dr. Stan Dosso, Departmental Member
(School of Earth and Ocean Sciences, University of Victoria)

Dr. George Spence, Departmental Member
(School of Earth and Ocean Sciences, University of Victoria)

Dr. Adam Zielinski, Outside Member
(Department of Electrical and Computer Engineering, University of Victoria)

Mr. David Hannay, Additional Member
(JASCO Applied Sciences)

ABSTRACT

Ocean environments with sloped seafloors can give rise to sound paths that do not remain in a constant plane of propagation. Numerical modelling of sound fields in such environments requires the use of computer models that fully account for out-of-plane sound propagation effects. The inclusion of these three-dimensional effects can be computationally intensive and the effects are often neglected in computer sound propagation codes. The current state-of-the art in sound propagation modelling has seen the development of models that can fully account for out-of-plane sound propagation. Such a model has been implemented in this research to provide acoustic consultants JASCO Applied Sciences with an important tool for environmental noise impact assessment in complicated marine environments. The model is described and validation results are shown for benchmark test cases. The model is also applied to study three-dimensional propagation effects in measured data from a realistic ocean environment. Particular analysis techniques assist in the interpretation of the modelled sound field for this physical test environment providing new insight into the characteristics of the test environment.

Contents

List of Tables

List of Figures

ACKNOWLEDGEMENTS

Very sincere thanks are extended to my supervisor Ross Chapman for your wisdom, guidance, and unfailing encouragement throughout the completion of this research. The experience of working with you has been invaluable. I would also like to thank David Hannay for your deep insight in discussing the finer details of aspects of this work. I sincerely appreciate the helpful discussions, input and knowledge gained from David Thomson while coding this algorithm. I also owe gratitude to all of my colleagues at JASCO Applied Sciences for your support, patience and understanding through this long process. Funding for this work was provided by the MITACS Accelerate BC program and the work was very generously supported by JASCO Applied Sciences.

Chapter 1

Problem Definition

1.1 Motivation

The ocean is an efficient medium for sound propagation and many marine animals rely on sound to communicate, navigate, and detect prey. Human activities in the marine environment can generate underwater sound which can potentially be harmful or disturbing to marine fauna. For this reason, environmental impact assessments of offshore industrial activities must often include noise impact studies for regulatory approval. The aim of a noise assessment study is to determine the spatial extent of human generated sound and to evaluate potential impacts from sound levels that exceed specific thresholds. This information is necessary for the effective assessment and management of anthropogenic noise in the marine environment.

Sound level contour maps, such as the example shown in Figure 1.1, are often included in a noise assessment to show graphically the noise footprint of a particular activity. The data underlying these contour maps can be used to determine ranges from a sound source within which animals might be exposed to potentially harmful sound levels and to determine zones of impact. These zones define the areas in which there is potential for auditory injury, disturbance, behavioral effects, and masking. A complete noise assessment generally also includes a mitigation plan to identify measures that can minimize noise impacts. This may include planning of the activities to avoid times and areas with high expected density of animals. Exclusion zones may be defined that delimit the areas of potential for auditory injury with a corresponding set of practices to be followed if a marine mammal is observed within an exclusion zone (for example, a noise source may be ordered to temporarily shut-down until the

mammal exits the zone). If a noise footprint is found to be intolerably large then reasonable means of noise mitigation at the source can be assessed to attempt to reduce the footprint of noise exposure.

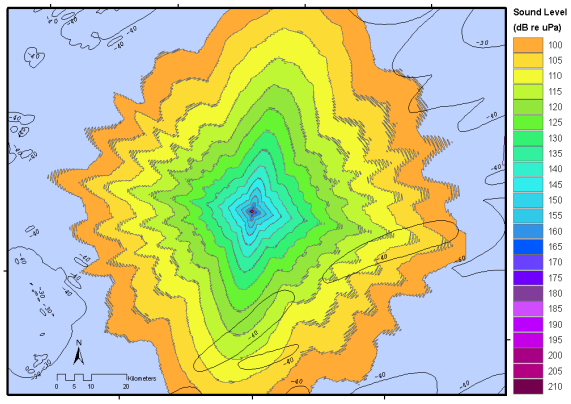

Figure 1.1: Example sound level contour map for a directional sound source. The contours present received sound levels at a single depth computed by subtracting modelled transmission loss from a direction-dependent source level.

Such sound level contour maps are constructed using computer models that calculate the propagation loss between a noise source (with known sound level) and a grid of surrounding receivers. These sound propagation models implement numeric approximations to a formulation of the acoustic wave equation. Different models are based on different formulations and approximations, but each solves for a spatial field of underwater sound pressure as influenced by the properties of the surrounding ocean waveguide environment. Within a model the environment may be assumed to vary as a function of a single dimension (depth), two dimensions (range and depth), or three dimensions (range, depth and azimuth) - each progressively more complex to handle computationally. Three-dimensional (3D) models provide the most accurate representation of a true environment, but are the most computationally intensive since they involve partial differential equations in range, depth, and azimuth.

For radially symmetric environments, in which sound propagation is assumed to be independent of azimuth, two dimensional (2D) acoustic models accurately predict sound propagation at a significant computational savings compared to 3D models. Environments that are not radially symmetric are better represented using pseudo-3D (also called Nx2D) models in which independent 2D fields are solved over a fan of radials surrounding a source, though a derivative in azimuth is not computed. For most applications Nx2D models are preferred over full 3D solutions to avoid

prohibitively long model run times. However, it is known [44, 7, 42], and it will also be shown in this work, that important propagation effects can arise in non-radially symmetric environments which cannot be accounted for with Nx2D models.

Typical noise assessment studies involve modelling noise footprints that surround broadband noise sources over regions of interest which can extend tens of kilometers away from the source. Many individual frequencies are modelled separately and the single frequency results are summed to provide broadband sound level estimates. These repeated, long-range calculations favour the use of Nx2D models, in spite of their reduced accuracy. However many noise assessments are considered for coastal environments with seafloors that slope toward shore. These 'wedge' environments typify the non-radial symmetry that is poorly handled using Nx2D models.

Early work that accounted for 3D effects in underwater modelling was conducted by Weston in 1961 [52] using a ray theoretic approach for a constant sloped seafloor. In 1977 Harrison [26] advanced this theory for more complicated seafloor profiles. Weinberg and Burridge [51] developed a hybrid approach using horizontal rays and modal eigenfunctions to model 3D sound fields. 3D modelling based on the parabolic equation (PE) method began in the late 1970's [4] and continued through the 1990's [15, 34]. An overview of the historical development of 3D PE model was presented by Tolstoy [50] and by Lee and Pierce [35]. However, historically 3D codes were not fully embraced outside of a research context because of the large computation times required for the full 3D solutions. Fully 3D propagation codes are now becoming more appealing with recent advances in propagation modelling and with the improved capabilities of modern computers with multiple processors. Currently several groups in the underwater sound modelling community are considering problems in non-radially symmetric environments that exhibit effects which are best handled with fully 3D propagation codes [19, 47, 29, 10]. This trend towards 3D models points to the importance of considering full 3D models in noise assessment so that decisions in environmental management can be based on state-of-the-art modelling capabilities.

This PhD research has been undertaken to provide Victoria-based acoustic consulting company JASCO Applied Sciences with a cutting-edge tool for noise assessment that will benefit from this evolution toward full 3D underwater sound propagation modelling. This research is specifically focussed on the parabolic equation method as the foundation of the propagation model. JASCO's current standard model for environmental noise assessment is the parabolic equation based Marine Operations Noise Model (MONM). The model applies Nx2D calculations for computational effi-

ciency. The Nx2D approximation is sufficiently accurate for noise assessment in many environments, but a weakness of the model lies in its inaccurate representation of the sound field in non-radially symmetric environments. As part of this thesis work, a 3D extension to the model has been developed (MONM3D).

Several 3D PE codes are in current use within in the underwater sound propagation modelling community [19, 7, 43, 45, 21]. These codes each differ slightly in their underlying algorithms and each was considered as a possible approach at the outset for this work. However, these codes are not publicly available for use within JASCO, nor do they contain some key features in the existing 2D version of MONM. One such feature is that MONM incorporates a tessellated [1] model grid to improve the model's efficiency. Typically a model grid can be thought of as a set of radials emanating from a sound source in a spoke pattern. Close to the source the 'spokes' are densely packed and far from the source the spokes are widely separated. In a tessellated grid the number of radials in the grid varies with range from the source such that the density of radials is bounded over the grid. This strategic definition of the grid aids in reducing the overall model run time by reducing the required number of computation points. Given the computational burden of full 3D calculations, this important feature of the model was maintained in the 3D version (MONM3D) coded for this project. This unique grid design distinguishes MONM3D from other 3D propagation models. The MONM3D algorithm most closely matches those applied in the PECan model [7] and the approaches used by Sturm [45] with slight differences in regards to discretization etc.

The full 3D code will be introduced in this report and the model will be used to simulate 3D propagation effects in a specific test case environment for which experimental data exist. This test case investigation will demonstrate the abilities of the model and will afford opportunity to examine the nature of 3D propagation in a wedge environment providing a strong basis for understanding these effects. Interpretations of the model results will be used to explore the nature of the 3D propagation effects in the test environment and to explain the features observed in the measured data. This particular test environment was selected because it has been the subject of prior propagation studies, and because it is an area of active interest for acoustic experiments at the South Florida Ocean Measurement Facility [38]. Results from the previous investigations for this environment provide some benchmarks against which

[1] "Tessellation" is defined by the New Oxford Dictionary of English as "an arrangement of polygons without gaps or overlapping, especially in a repeated pattern"

the MONM3D calculations can be compared; however, this investigation involves a more detailed examination of the 3D effects. A new approach in this investigation is the inclusion of range-dependent geoacoustic parameters in the model simulations and the strength of the 3D effect has been considered as the sound travels through varying environmental regimes. This provides a better understanding of the relationship between the properties of the environment and the 3D effect.

1.2 Objectives

This research was undertaken to implement a fully 3D parabolic equation code suitable for use in environmental noise assessment. A peer-reviewed description of the model along with validation results has been published [2]. A further goal for this work was to develop a firm understanding of the nature of 3D sound propagation in coastal environments through application of the model in the analysis of a case study. The specific objectives for this research are as follows:

1. Implement and Validate a 3D sound propagation model
    - Modify the code of JASCO's sound propagation model to provide a fully 3D version, MONM3D.
    - Validate the accuracy of MONM3D output using two benchmark test cases.
    - Test the efficiency gains achieved through the of use of tessellation.
2. Use MONM3D to investigate the results from a sound propagation experiment suspected to contain evidence of 3D propagation effects
    - Explore the ability of MONM3D to reproduce features observed in the measured data.
    - Characterize the 3D propagation effect in the test case environment.
    - Investigate the influence that the environmental model parameters have on the 3D effect.
    - Hypothesize an explanation for the model-data mismatch noted from previous investigations of the 3D effect.

1.3 Organization of this Thesis

This thesis is organized as follows. Chapter 2 provides some background that describes 3D sound propagation effects, their causes and reasons that they are important. Next this chapter provides a derivation of the 3D parabolic equation and discusses some techniques in parabolic equation modelling. Chapter 3 provides the details of the model algorithm underlying MONM3D and highlights some of the unique features of this model.

Chapter 4 introduces the capabilities of the model and demonstrates the model accuracy by consideration of two benchmark test cases. The first consists of a simple flat environment to confirm that the 3D version of the model maintains accuracy for environments that do not exhibit an influence from 3D propagation effects. The accuracy of MONM3D is confirmed through comparison with results from other established codes. Next, a test case containing a planar sloping seafloor is considered to illustrate the simulation 3D propagation effects; again, the MONM3D output is compared against accepted results of other 3D PE models.

Having established confidence in the accuracy of MONM3D, Chapter 5 delves into the exploration of a measured data set using MONM3D as an analysis tool to describe and characterize the nature of the observed 3D propagation effect. This chapter contains a comparison of Nx2D and 3D model results, and considers how variations of the model parameters (specifically the geoacoustic definition) influences the strength of the 3D effect. The model output is compared to measured data and explanations for observed model-data mismatches are provided. Finally Chapter 6 provides a summary and discussion of the work completed.

Chapter 2

Background

Sound pressure fields are influenced by the properties of the media through which the sound waves propagate. The speed of sound in the ocean is defined by the temperature, salinity and pressure of the water, and the water's chemical composition affects the sound attenuation. In the seafloor, the sound speed and attenuation are defined by the porosity, density and bulk modulus of the substrate material. Discontinuities and gradients of the medium properties cause reflection and refraction of sound. Appreciable changes of the properties typically occur rapidly with depth but gradually with range.

Ocean sound propagation can be simulated using numerical computer models, the simplest forms of which only consider the influence of environmental properties that vary in depth but neglect the influence of the weak horizontal gradients. These one-dimensional (1D) models represent ocean environments using stratified, range-independent layers. An accounting for weak environmental variations in range requires the use of two-dimensional (2D) models, in which the stratified environment can be separated into locally range-independent segments and the environmental properties can vary between segments [32]. In 2D models it is assumed that the environmental properties do not vary azimuthally.

In reality, ocean environments exhibit spatial variability in all directions and are better represented with the class of models commonly known as Nx2D, or pseudo-3D. Such models solve for 2D sound fields that emanate radially from a sound source in many different vertical planes, each with uniquely defined range-dependent environmental parameters. These Nx2D models assume that the influence of cross-range environmental gradients is too weak to divert sound from planar (range-depth) propagation, and are not fully three-dimensional (3D) since they neglect any potential

sound coupling between adjacent planes. Fully 3D models include terms to account for the out-of-plane propagation that can occur in some environments. These models represent most accurately the true acoustic field in environments with complex spatial variability, but are computationally more intensive than 2D or Nx2D models [7, 21].

This section will explore the environmental conditions that can give rise to 3D propagation effects and demonstrate the influence that 3D effects have on acoustic fields. The focus of this research project is to investigate and interpret the influence of such 3D effects through the use of an acoustic model based on the parabolic equation. Therefore, this section will also provide a derivation of the 3D parabolic equation and methods for its solution will be discussed.

2.1 Three-Dimensional Sound Propagation

There are two main environmental conditions which can lead to out-of-plane sound propagation that should be accounted for in acoustic propagation models. These conditions fall into two classes; namely, volume effects and bathymetric effects. Volume effects refer to influences from physical features in the water column that exhibit three-dimensionally variable sound speeds, that persist in time, and that extend over significant spatial scales. Meso-scale eddies, large ocean fronts, and internal waves exemplify such physical features which can lead to horizontal refraction of sound energy. Experimental evidence of such effects have been reported [23, 3, 36]. Volume effects can be complicated to model since detailed information about the water column is required, but is not often readily available. Also, the water column features responsible for the effect are both spatially and temporally variable. Volume effects have not been specifically considered in the present research, though there is no reason to believe that the model would not accurately predict such effects.

Bathymetric effects refer to influences from gradients in the bathymetry that can lead to horizontal curvature of sound ray paths. This present research has focused on model environments influenced by bathymetric effects. Experimental evidence of bathymetric 3D propagation effects have been reported for environments with canyons [19] and sloping coastal seafloors [29, 46].

For a conceptual understanding of 3D propagation it is instructive to consider the simple case of a gently sloping seafloor and an iso-speed water column. The rest of this section will consider the behaviour of adiabatic modes in this simple case as a basis for understanding the nature and importance of three dimensional propagation.

A sound source located at the bottom of the slope shown in Figure 2.1 emits rays that travel up the slope and are successively reflected off the sea surface and the seafloor. The propagation angle for each reflection, labelled θ in the figure, steepens as the ray travels upslope.

This ray steepening can be described using the ray invariant introduced by Weston [52] and defined by the following equation:

$$\int_0^H \frac{\sin\theta}{c(z)} dz = T \tag{2.1}$$

where θ is the angle measured from the horizontal, c is sound speed and the integral is taken over depth, z, with water depth H. T is constant for gradually changing environments and small bottom slope such that the ray propagation angle is greater than twice the bottom slope [52, 26].

For a gradually sloping and iso-speed environment the ray invariant equation reduces to the following expression relating the propagation angle, θ, and water depth, H, at a particular point along the slope:

$$H \sin\theta = const \tag{2.2}$$

This relationship shows that a given ray's propagation angle increases with each bottom bounce as the ray travels up-slope in the direction of decreasing water depth.

Consider that a propagating normal mode is composed of the sum of two interfer-

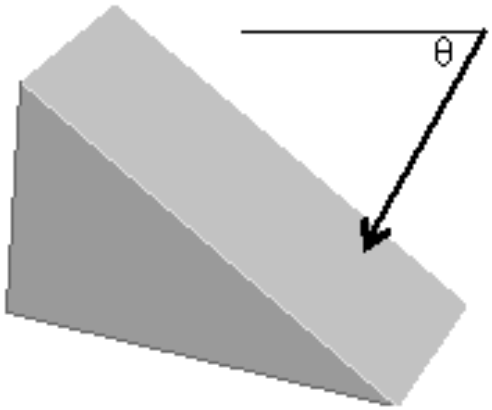

Figure 2.1: Simple wedge geometry and steepening ray travelling upslope with initial propagation angle θ.

ing, multiply-reflected, plane waves whose phases differ by an integer multiple of 2π. Ray paths associated with particular modes travel normal to these wave fronts at specific propagation angles related to the mode wave number. Therefore as these mode propagation angles steepen during up-slope travel there are corresponding changes of the vertical and horizontal components of the mode wave numbers.

For gradual environmental variations the shapes of the adiabatic mode functions adapt to the local water depth such that the number of nodes (or nulls) of the mode remains constant, but the spacing between the nodes increases or decreases as does the water depth. The normal mode phase velocities are greater in the shallow water at the top of the slope (where the rays are steeper) than in the deeper water; therefore, mode paths travelling obliquely upslope tend to turn toward the deeper water in the way that rays turn in refractive media [27].

Each mode has a horizontal wave-number, $k_{horizontal}$, with components that define the horizontal 'heading' of the mode along its path. Let $k_{contour}$ be the component of $k_{horizontal}$ in the direction of the iso-bathymetric contours; this component remains constant. For this sloping wedge example the constant depth contours are straight, parallel, and perpendicular to the slope. Harrison [28] defined the mode heading, ϕ, with respect to the direction of these contours in the following relationship:

$$\cos\phi = \frac{k_{contour}}{k_{horizontal}} = \frac{const}{\cos\theta} \tag{2.3}$$

This leads to a second ray invariant for the wedge example involving the heading, ϕ, and vertical propagation angle, θ:

$$\cos\theta\cos\phi = const \tag{2.4}$$

Similar relationships can be derived for more complicated bathymetries such as troughs and ridges [27]. It is noted that sound ray paths oriented perpendicular to the bathymetric contours (i.e. where $\phi = 90$) remain constant in the orientation and do not experience horizontal bending.

The invariants in Equation (2.2) and 2.4 can be combined to provide a relationship for the heading, ϕ, at any point along the ray path in terms of the local water depth, the initial heading and the initial propagation angle of the ray. The integral defining the distance that a mode travels across the slope (in the direction of the constant depth contours) can be expressed in terms of this relationship. An equation for the relative distance travelled upslope can then be expressed in terms of the initial ray

conditions. For gradually changing environments, the latter equation describes a continuous curve that traces a mode's path in the horizontal plane [26]. For the wedge example, with an iso-velocity water column, the modes follow horizontal paths that are defined by the hyperbolas:

$$y^2(1-\cos^2\theta_0\cos^2\phi_0) = (\frac{1-\cos^2\theta_0\cos^2\phi_0}{\cos\theta_0\cos\phi_0}x - y_0\cos\theta_0\sin\phi_0)^2 + (y_0\sin\theta_0)^2 \quad (2.5)$$

for y in the along-slope direction (i.e. up- and down-slope) and x in the cross-slope direction (i.e. in the direction of the lines of constant contour).

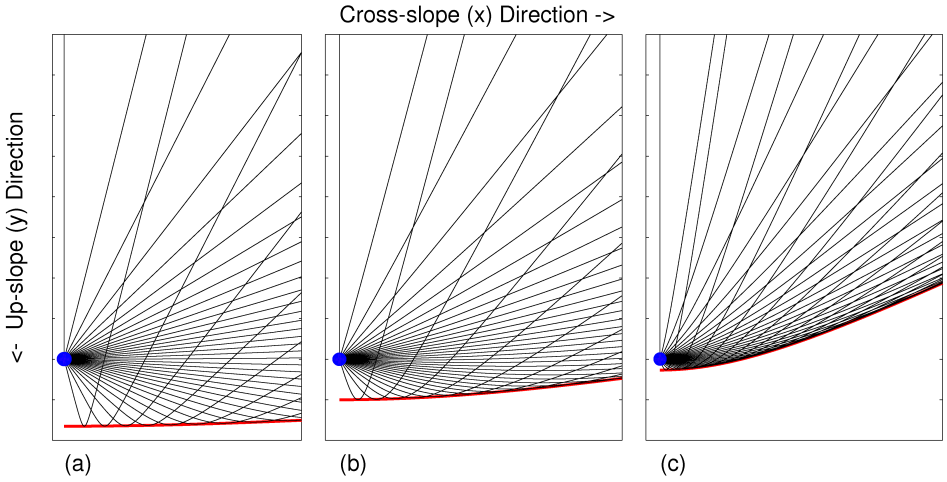

Figure 2.2: Hyperbolic ray paths for fan of initial headings (between 10 and 180 degrees) and for intial propagation angles of 10° (a), 30° (b), and 60° (c). Envelopes delimiting the corresponding shadow zone boundaries are indicated with red curves. Source location indicated with a blue circle.

Figure 2.2 shows three example plots of such hyperbolic curves for three different initial angles of propagation. Each panel in the figure shows a fan of ray paths (with initial headings between 10 and 180 degrees) that emanate from a source located at a position on the y-axis indicated with a blue circle in each plot. The y-axis depicts the along-slope direction (up-slope being toward the bottom of the panel) and the x-axis depicts the cross-slope direction. Rays that leave the source with a heading in the up-slope direction are noted to turn down-slope along hyperbolic arcs. The initial propagation angle used to generate the curves increases from 10° in panel (a), 30° in panel (b) to 60° in panel (c) in the figure. Ray propagation angles increase

with increasing mode number, and therefore each panel also may also be considered to represent a different propagating mode with mode number increasing from (a) to (c). The horizontal paths are noted to turn more sharply as the initial angle of propagation, or the mode number, increases.

As can be seen in Figure 2.2 the horizontal refraction of the ray paths leads to acoustic shadow zones, that is, areas of the slope that are not ensonified by particular modes. It is commonly understood from a 2D perspective that a shadow zone is expected when a mode reaches cut-off as it heads up-slope. That is, if the propagation angle increases beyond the critical angle, or if the water becomes too shallow to support mode propagation. The paths in Figure 2.2 are assumed not to have reached cut-off in this sense. From a 3D perspective, though, the paths in Figure 2.2 show that the shadow zones arising from the horizontal bending of the mode paths can be larger and can differ in shape compared to what is expected in a 2D consideration. As well, each panel contains regions where different ray paths associated with a particular mode intersect. These regions of intra-modal interference and the apparent convergence zones are not predicted from a 2D consideration of the environment.

This discussion has focussed on the example of a simple wedge but similar ray invariants and horizontal path equations can also be derived for other bottom features such as seamounts, basins and ridges [26]. Equations that aid in understanding the 3D field in a very specific and simple environment have been provided. This is instructive for understanding the propagation of sound out of the vertical plane and the resulting shadow zones and convergence zones that influence the acoustic field. Accurate acoustic field calculations for 3D variable environments must be done with models that are able to handle these cross-range propagation effects.

2.2 The 3D Parabolic Equation

Parabolic equation (PE) models are commonly applied to model complex, range-dependent environments and can be set up in a full 3D formulation involving partial differential equations in azimuth as well as in depth [12, 21, 48]. This section provides the derivation of the full 3D form of the PE and the approaches that are commonly implemented for its solution.

Working in cylindrical coordinates with radial component r, azimuthal component φ, and depth component z (defined to be positive downwards), the acoustic field due to a point source is defined by a time-varying pressure field $P(r, \varphi, z, t)$ governed by

the acoustic wave equation. Time harmonic solutions to the acoustic wave equation exist in the form $p(r, \varphi, z)e^{-i\omega t}$. The spatial part of the pressure function, $p(r, \varphi, z)$, is obtained from solutions to the Helmholtz equation, which is written:

$$\frac{1}{r}\frac{\partial}{\partial r}\left(r\frac{\partial p}{\partial r}\right) + \frac{1}{r^2}\frac{\partial^2 p}{\partial \varphi^2} + \rho\frac{\partial}{\partial z}\left(\frac{1}{\rho}\frac{\partial p}{\partial z}\right) + k_0^2 n^2 p = 0. \tag{2.6}$$

In Equation (2.6) $k_0 = \omega/c_0$ is a reference acoustic wave number, ρ is density, $n = c_0/c(r, \varphi, z)$ is the index of refraction, $c(r, \varphi, z)$ is the sound speed of the medium and c_0 is a reference sound speed.
The index of refraction term is replaced with a term $N = n(1 + i\alpha(z))$ to include an attenuation term, $\alpha(z)$, in Nepers. The attenuation can also be expressed in dB/λ, represented by β, in which case $\alpha(z) = \eta\beta$ for $\eta = (40\pi log_{10}e)^{-1}$.

Equation (2.6) is simplified by removing the influence of geometric spreading through substituting

$$p(r, \varphi, z) = \frac{1}{\sqrt{r}}u(r, \varphi, z) \tag{2.7}$$

which gives

$$\frac{\partial^2 u}{\partial r^2} + \frac{1}{r^2}\frac{\partial^2 u}{\varphi^2} + \rho\frac{\partial}{\partial z}\left(\frac{1}{\rho}\frac{\partial u}{\partial z}\right) + k_0^2 N^2 u = 0. \tag{2.8}$$

Following an operator formalism, the following notation is introduced:

$$P_{op} = \frac{\partial}{\partial r} \tag{2.9a}$$

and

$$Q_{op} = \sqrt{\mu + \epsilon + \upsilon + 1} \tag{2.9b}$$

where

$$\epsilon = N^2 - 1 \tag{2.9c}$$

$$\mu = \frac{1}{k_0^2}\rho\frac{\partial}{\partial z}\left(\frac{1}{\rho}\frac{\partial}{\partial z}\right) \tag{2.9d}$$

$$\upsilon = \frac{1}{k_0^2 r^2}\frac{\partial^2}{\partial \varphi^2} \tag{2.9e}$$

Equation (2.8) then becomes:

$$\left(P_{op}^2 + k_0^2 Q_{op}^2\right) u = 0, \tag{2.10}$$

which expands to:

$$(P_{op} + ik_0 Q_{op})(P_{op} - ik_0 Q_{op})u + ik_0(P_{op}Q_{op} - Q_{op}P_{op})u = 0 \tag{2.11}$$

For range-independent media, the last term in Equation (2.11) is zero, and it is negligible for weakly range dependent environments. By also assuming that backscattered energy can be neglected in the model, the final equation for outgoing waves is given by:

$$P_{op}u = ik_0 Q_{op}u$$

or

$$\frac{\partial}{\partial r}u = ik_0 Q_{op}u \tag{2.12}$$

Equation (2.12) is in parabolic form and it is the standard equation that underlies all PE acoustic models. The equation as expressed is in full 3D form since it includes the azimuthal operator term in Equation (2.9e) to account for the influence of out-of-plane sound propagation. In contrast, 2D PE models neglect this term and account only for the effects of refraction and diffraction through the terms in Equation (2.9c) and Equation (2.9d) respectively.

The parabolic form of Equation (2.12) is an initial and boundary value problem. A pressure release boundary is commonly defined at the sea surface and a bottom boundary condition is defined such that sound energy radiates away to infinity in the sub-bottom. The equation contains only first-order derivatives in r and is amenable to standard numerical marching solutions. Given an initial starting field at range $r = r_0$ the solution is evolutionary in range. However, the equation contains a square root that cannot be solved directly with numerical methods and must be further approximated. Various approximations of this square root term give rise to different algorithms for solving the parabolic wave equation, each of which differ with respect to their accuracy and their applicability to specific problems.

Some PE acoustic models approximate the square root by a rational polynomial expansion and generate solutions using finite difference approaches. These finite difference models (e.g. FOR3D [6]) provide high asymptotic accuracy (that is they accurately represent solutions for a wide range of propagation angles) but they require high resolution computational grids for numerical accuracy, reducing their computational efficiency. In contrast, split-step methods consider the formal solution to

Equation (2.12) written as:

$$u\left(r+\Delta r,\psi,z\right)=\exp[ik_0\Delta rQ_{op}]u\left(r,\psi,z\right) \tag{2.13}$$

This formulation allows for coarser grids (limited by the variability of the environment) and can be more efficient for many problems. The split-step Fourier technique [43, 48] applies a linear expansion to approximate the square root and then affects the exponentials and the depth derivative via Fourier transforms. This technique is numerically efficient but models based on this approach are limited in their ability to handle discontinuities in depth and are not appropriate for problems involving vertically steep propagation angles [43, 14]. Split-step Fourier models are, therefore, not well suited to shallow-water problems in which the fields are strongly influenced by steeply-propagating, bottom interacting sound paths.

Alternatively, split-step Padé models (e.g. RAM, Collins [13]) use a Padé expansion to approximate the exponential term in Equation (2.13) and handle the depth derivative using finite-difference or finite-element techniques. The approximation of the propagator used in this approach allows for large range steps. The split-step Padé approximation provides a combination of efficiency and accuracy even for relatively steep propagation angles. The MONM3D algorithm solves Equation (2.13) via the split-step Padé approach of Collins due to its efficiency and suitability for many range-dependent, shallow water acoustic propagation problems [12, 14].

Chapter 3

Model Description

The first part of this research project involved coding and implementing a full 3D PE model, MONM3D. This section outlines the algorithm that is implemented in MONM3D, describes some unique features of the model, and provides an overview of some of the analysis techniques that are used throughout this report to present and interpret the MONM3D output.

3.1 MONM3D - Model Algorithm

Recall from Section 2.2 that the PE can be expressed in operator form as:

$$\frac{\partial}{\partial r}u = ik_0 Q_{op} u \tag{3.1}$$

where Q_{op} is the operator term

$$Q_{op} = \sqrt{\mu + \epsilon + \upsilon + 1}. \tag{3.2}$$

The 3D algorithm that is applied in MONM3D assumes that the field variations in azimuth are sufficiently gradual that the square root term, Q_{op}, can be re-written:

$$Q_{op} = \sqrt{1 + (\epsilon + \mu) + \upsilon} \approx \sqrt{1 + \epsilon + \mu} + \left(\frac{\upsilon}{2}\right) \tag{3.3}$$

This approximation is considered 'narrow angle' in azimuth. With this substitution

Equation (3.1) becomes:

$$\frac{\partial}{\partial r}u = ik_0\left(\sqrt{1+\epsilon+\mu}+\frac{\upsilon}{2}\right)u \tag{3.4}$$

which has a formal solution written as

$$u(r+\Delta r,\varphi,z) = \exp\left[ik_0\Delta r\left(\sqrt{1+\epsilon+\mu}+\frac{\upsilon}{2}\right)\right]u(r,\varphi,z). \tag{3.5}$$

Field solutions can then be obtained using an alternating directions approach [16, 21, 44]. In this approach the following two systems are solved separately and sequentially in the 3D algorithm:

$$w(r+\Delta r,\varphi,z) = \exp\left[ik_0\Delta r\sqrt{1+\epsilon+\mu}\right]u(r,\varphi,z) \tag{3.6a}$$

$$u(r+\Delta r,\varphi,z) = \exp\left[ik_0\Delta r\frac{\upsilon}{2}\right]w(r+\Delta r,\varphi,z). \tag{3.6b}$$

Each step in the range-marching algorithm involves two calculations. First the 2D solution as a function of depth is calculated at each point in azimuth using Equation (3.6a), and then the cross-radial correction factor is applied using the azimuthal operator in Equation (3.6b) to account for influences from out-of-plane sound propagation.

3.1.1 Depth Operator

Consider first the Nx2D solutions from Equation (3.6a). Following the approach of Collins [12], the exponential of the square root term is approximated with a rational Padé expansion and the solution can be written as follows:

$$w(r+\Delta r,\varphi,z) = \exp\left(ik_0\Delta r\right)\left(1+\sum_{j=1}^{n_p}\frac{\alpha_{j,n_p}(\epsilon+\mu)}{1+\beta_{j,n_p}(\epsilon+\mu)}\right)u(r,\varphi,z). \tag{3.7}$$

The coefficients α and β in Equation (3.7) are defined such that the solutions satisfy accuracy and stability constraints that are imposed to annihilate the evanescent part of the spectrum [11, 17]. In Equation (3.7), n_p represents the number of Padé terms that are included in the expansion. The greater the number of included Padé terms, the more accurate the approximation and the more 'wide-angle' is the solution (in

depth).

Upon solution of Equation (3.7) the Nx2D fields have been defined at locations $(r + \Delta r, \varphi, z)$, based on the known values at points (r, φ, z). The 3D algorithm proceeds with the solution of Equation (3.6b) before progressing to the next range step.

3.1.2 Azimuthal Operator

The azimuthal derivative term in Equation (3.6b) is implemented in MONM3D either using a Fourier approach or using centered finite differences. The choice of implementation is a configurable parameter of the model. In general, the Fourier approach will allow wider spacing between azimuthal planes, requiring fewer points in azimuth and making this approach more efficient than a standard finite difference approach. Fourier transforms are used to solve Equation (3.6b) by re-writing the equation in the following manner:

$$u(r + \Delta r, \varphi, z) = F_{\varphi}^{-1} \left(\Theta_{\varphi} F_{\varphi} w(r + \Delta r, \varphi, z) \right) \tag{3.8}$$

where

$$\Theta_{\varphi} = \exp\left(\frac{-ik_{\varphi}^2 \Delta r}{2k_0 r(r + \Delta r)} \right) \tag{3.9}$$

F_{φ} and F_{φ}^{-1} are the forward and inverse Fourier transforms with respect to φ, and k_{φ} is the azimuthal wave number [21].

The efficiency of a finite-difference approach can be comparable to that of a Fourier approach if an approximation is applied that is accurate to higher order [45]. The finite -difference approach involves making the substitution

$$\exp\left[ik_0 \Delta r \frac{\upsilon}{2} \right] = \frac{1 + (ik_0 \frac{\Delta r}{4})\upsilon}{1 - (ik_0 \frac{\Delta r}{4})\upsilon} \tag{3.10}$$

and re-arranging Equation (3.6b) to obtain the following equation:

$$\left(I - \frac{ik_0 \Delta r}{4} \left(\frac{1}{k_0^2 r^2} \frac{\partial^2}{\partial \varphi^2} \right) \right) u(r+\Delta r, \varphi, z) = \left(I + \frac{ik_0 \Delta r}{4} \left(\frac{1}{k_0^2 r^2} \frac{\partial^2}{\partial \varphi^2} \right) \right) w(r+\Delta r, \varphi, z) \tag{3.11}$$

where $w(r + \Delta r, \varphi, z)$ represents the Nx2D solution obtained from Equation (3.6a).

Consider the grid points $u_{\varphi\pm n\Delta\varphi}$, surrounding u_φ, for integer $n > 0$. Taylor series expansions for $u_{\varphi+n\Delta\varphi}$, $u_{\varphi-n\Delta\varphi}$ are written:

$$u_{\varphi+n\Delta\varphi} = \sum_{m=0}^{\infty} n^m \frac{\Delta\varphi^m}{m!} \left(\frac{\partial^m u}{\partial\varphi^m}\right)_\varphi = u_\varphi + n\Delta\varphi \left(\frac{\partial u}{\partial\varphi}\right)_\varphi + n^2 \frac{\Delta\varphi^2}{2!} \left(\frac{\partial u}{\partial\varphi}\right)_\varphi + ... \quad (3.12a)$$

$$u_{\varphi-n\Delta\varphi} = \sum_{m=0}^{\infty} (-n^m) \frac{\Delta\varphi^m}{m!} \left(\frac{\partial^m u}{\partial\varphi^m}\right)_\varphi = u_\varphi - n\Delta\varphi \left(\frac{\partial u}{\partial\varphi}\right)_\varphi + n^2 \frac{\Delta\varphi^2}{2!} \left(\frac{\partial u}{\partial\varphi}\right)_\varphi - ... \quad (3.12b)$$

Summing Equation (3.12a) and (3.12b) with $n = 1$ and re-arranging provides a standard centered-difference three-point stencil scheme that approximates the second derivative:

$$\frac{\partial^2 u}{\partial\varphi^2} = \frac{u_{\varphi-\Delta\varphi} - 2u_\varphi + u_{\varphi+\Delta\varphi}}{\Delta\varphi^2} + O(\Delta\varphi^2). \quad (3.13)$$

Terms up to second order are retained and the result approximates the derivative to second-order accuracy.

Greater accuracy for the derivative approximation can be obtained by combining Taylor series expansions of more points surrounding u_φ, retaining more terms in the Taylor series expansion for each point. For example, a five point stencil scheme for the second derivative that is given by:

$$\frac{\partial^2 u}{\partial\varphi^2} = \frac{-u_{\varphi+2} + 16u_{\varphi+1} - 30u_\varphi + 16u_{\varphi-1} - u_{\varphi-2}}{12\Delta\varphi^2} + O(\Delta\varphi^4). \quad (3.14)$$

The centered difference scheme in Equation (3.14) retains terms up to fourth order and thus provides a better approximation of the derivative. This process can be extended to any higher-order approximation of order $2l$ using the following equations to formulate a ($2l$-1)-point stencil:

$$\frac{\partial^2 u}{\partial\varphi^2} = \frac{\sum_{k=1}^{l} \gamma_k u_{\varphi+k\Delta\varphi} - \kappa u_\varphi + \sum_{k=1}^{l} \gamma_k u_{\varphi-k\Delta\varphi}}{\Delta\varphi^2} + O(\Delta\varphi^{2l}) \quad (3.15)$$

where $\kappa = \sum_1^k \gamma_k$ for $\gamma_1, \gamma_2, \gamma_3, ...$ satisfying:

$\gamma_1 + 2^2\gamma_2 + ... + (l-1)^2\gamma_{l-1} + l^2\gamma_l = 1,$

$\gamma_1 + 2^4\gamma_2 + ... + (l-1)^4\gamma_{l-1} + l^4\gamma_l = 0,$
$\gamma_1 + 2^6\gamma_2 + ... + (l-1)^6\gamma_{l-1} + l^6\gamma_l = 0,...$
$\gamma_1 + 2^{2l}\gamma_2 + ... + (l-1)^{2l}\gamma_{l-1} + l^{2l}\gamma_l = 0.$

The centered-difference scheme leads to systems of linear algebraic equations of order N_φ (the number of computation points in azimuth) that are solved for each point in depth. The systems of equations are in the form of banded diagonal matrices with band-widths equal to the size of the stencil scheme used. The three-point scheme leads to tri-diagonal systems and the five-point scheme leads to penta-diagonal systems. There are also entries in the upper right and the bottom left corners of the diagonal matrices to satisfy the following continuity condition:

$$u_{\varphi=0} = u_{\varphi=360}. \tag{3.16}$$

The banded matrices are solved in MONM3D using LU decomposition and forward and back substitution. The coefficient of the azimuthal derivative in Equation (3.11) is a function only of range, therefore the LU decomposition need only be carried out once at each range step and is then used to apply the azimuthal corrections at each depth.

Sturm and Fawcett [45] showed by way of a test case that an increased azimuthal grid spacing is acceptable with higher-order differencing schemes due to the increased numerical accuracy of the derivative approximation. Thus higher-order finite-difference schemes permit the use of fewer azimuthal grid points compared to the number required for the same level of accuracy with lower-order approximations. To capitalize on this increase in efficiency, MONM3D incorporates the user-selectable option of either a three-point (second-order accurate) or a five-point (fourth-order accurate) stencil for the azimuthal derivative approximation.

Regardless of the approach taken to approximate the derivative term, the overall computation time for the algorithm scales with the number N_φ. A thoughtful selection of this value aids in improving efficiency. The tessellated pattern of the MONM3D grid (described in Section 3.2.1) is designed to provide an appropriate value of N_φ at all ranges.

3.2 Model Features

MONM3D is an extension of the existing Nx2D Marine Operations Noise Model (MONM) developed by JASCO Research Ltd and used to characterize underwater sound fields surrounding marine industrial noise sources, mainly for environmental assessment purposes. MONM incorporates the split-step Padé algorithm (ref. Section 2.2) that is used in the RAM model developed by Michael Collins [13]. The Nx2D model has undergone extensive benchmarking and testing at JASCO Research, and is believed to be a stable and reliable code for many problems [25]. MONM features the ability to account for the influence of shear waves in elastic seafloors through an "equivalent fluid" approximation, introduced by Zhang and Tindle [55], whereby the density in the seafloor is made complex to match the reflection coefficient to that of a real solid bottom with shear wave losses. All of the existing features in MONM have been maintained while the existing Nx2D code has been extended into full 3D form.

A unique feature of MONM, which becomes very important for full 3D calculations, is the incorporation of a tessellated model grid. This section explains the concept of tessellation and an associated interpolation scheme that becomes necessary with this approach. This feature enhances the efficiency of the MONM3D algorithm and distinguishes this model from other PE models.

3.2.1 Tessellation

The model grid in MONM3D is composed of layers of Cartesian grid points lying upon concentric rings about the source location. As the range-stepping algorithm marches outward from the source, depth-distributed solutions are obtained along paths that pass through radially-aligned grid points. Of course, adjacent radial paths diverge and the arc-length separation between them increases with range away from the source.

For 3D calculations the numerical accuracy of the azimuthal operator limits the acceptable arc-length separation between radials. The grid must contain a sufficient radial density to maintain the accuracy of the operator at the maximum range. Using a fixed number of radial paths (N_φ independent of range) the grid is excessively dense at ranges close to the source and computation time is wasted. To ensure that the number of calculations at each range step is desirable from both numerical and computational considerations, the arrangement of the computation grid in MONM3D is defined using a range-dependent $N_\varphi(r)$. This concept, here referred to as tessellation, differentiates MONM3D from many other models. Through tessellation the field is

neither over-sampled at ranges close to the source nor is it under-sampled at long ranges, striking a balance between numerical accuracy and computational burden.

Three example grid patterns for a single depth in a computational domain are shown in Figure 3.1 below; these patterns are replicated at each depth in the grid. The grid patterns in Figure 3.1 (a) and (b) contain fixed numbers of radial paths, 32 and 8 respectively. The first grid pattern is overly dense near the source and the second pattern is too sparse at range. Neither pattern provides a model with an effective combination of numerical accuracy and computational efficiency. Figure 3.1 (c) presents a tessellated grid pattern that begins with 8 radial paths at the first range step, the grid size increases to 16 radial paths at the fourth range step and contains 32 radial paths beyond the sixth range step. The tessellated pattern in Figure 3.1(c) is noted to exhibit a more desirable radial density at all ranges compared to the patterns in (a) and (b).

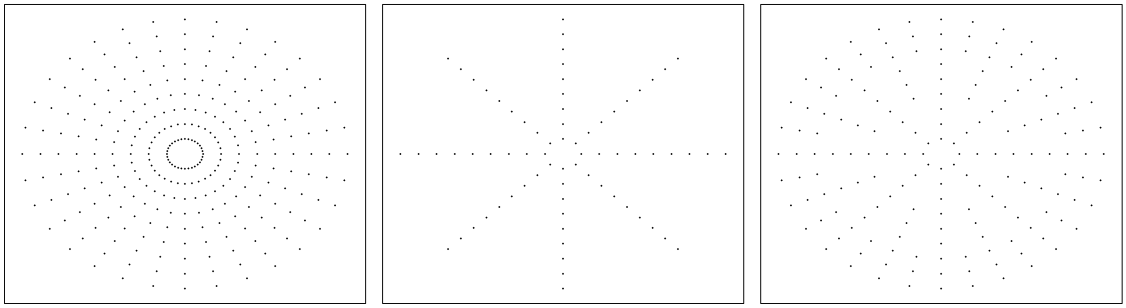

Figure 3.1: Computation grid patterns at a single depth. Fixed number [32 (a) and 8 (b)] of radial paths compared with a tessellated grid (c) using 8, 16 and then 32 radials as a function of range.

A MONM3D input configuration file is used to define $N_\varphi(r_0)$, that is, the number of radials in the grid at the first range step. Also specified is the maximum acceptable arc-length separation for the problem, Δs_{max}. This value will depend on the environment of the particular problem being modelled and will be a function of frequency. As with the determination of the appropriate range and depth grid spacing, the maximum acceptable azimuthal spacing is best determined for each problem through convergence testing.

A tessellator routine inside MONM3D automatically arranges the computation grid points in a tessellated pattern. The tessellator begins by assigning x-y-z posi-

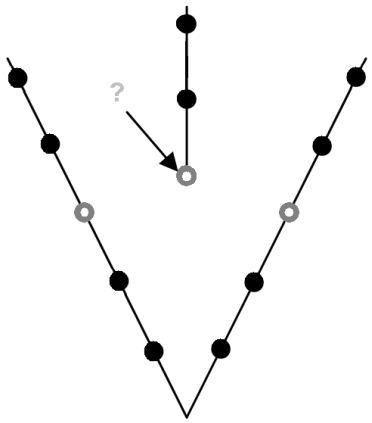

Figure 3.2: Newly-seeded radial path (center) requiring the definition of a starting field.

tion values to the $N_\varphi(r_0)$ points at the initial range. These points are equi-spaced about the source, at a radius dr, and the pattern is replicated at all depths in the grid. The routine proceeds in increments of dr, extending existing radial paths and assigning x-y-z position values to the grid points in each successive ring (distributed over depth). At every range step, the algorithm computes the arc-length separation between adjacent points in the ring. If the separation between points exceeds the user-defined threshold value then the routine doubles the number of points in that ring, halving the arc-length separation between the points and seeding new radial paths.

The implementation of the tessellated model grid is complicated by the fact that the PE range-marching algorithm requires, but does not define, the starting fields for the radial paths that commence beyond the first range step. Figure 3.2 shows a sector in the horizontal plane at a single depth of an example model grid containing only three radial paths for illustrative purposes. In this figure the solid black circles represent model grid points. At the range step here indicated with the hollow grey circles a new radial path is seeded (the central path in the figure). The PE algorithm requires a defined starting field for the new radial path in order to proceed to the next step in range. An interpolation scheme is implemented in MONM3D to estimate these required starting field values.

3.2.2 Radial Interpolation

The interpolation method applied in MONM3D is known as 'band-limited interpolation', a method commonly used in digital signal processing to reconstruct continuous functions from a set of sampled values. Consider a function p(φ) with Fourier transform P(w). If p(φ) is "band limited", such that P(w) = 0 for $|w| > W$ and if P(w) is sampled at a sampling frequency, WS, greater than or equal to $2W$ then it is known from sampling theory [41] that p(φ) can be reproduced by convolving the set of sampled points with a sinc function. The sinc function is unity at t=0, is 0 at all other points sampled at $2W$, its spectrum is constant inside the band W and is zero outside that band. Under the above conditions, a continuous function can be reconstructed without errors using a convolution of the form:

$$p(\varphi) = \sum_{n=-\infty}^{\infty} p_n \frac{\sin(2\pi w(t - nT_s))}{2\pi w(t - nT_s)} \tag{3.17}$$

for $W \leq w \leq WS - W$. This equation can be used as an interpolation tool to obtain the signal p(φ) from a set of sampled points. Hovem[30] showed that this convolution can be equivalently carried out in the transformed, P(w), domain. By increasing the period of the band-limited function P(w) the sampling frequency of p(φ) is also increased.

The period of P(w) is increased in the transformed domain through zero-extending. The function p(φ) is then recovered with an increased number of sample points by an inverse Fourier transform. The interpolation scheme is implemented in MONM3D using this Fourier transform approach.

When the range marching algorithm reaches a range step at which a tessellation occurs (i.e. a range step at which new radial paths are inserted into the computation grid because the maximum acceptable arc-length separation between radials has been exceeded) the field is interpolated to fill in the starting fields of the nascent radial paths.

At this point the Fast Fourier Transform (FFT) of the complex pressure field is taken over the ring of $N_\varphi(r)$ points and the transformed spectrum is zero-extended to double its period. The zero-extending involves dividing the Nyquist value evenly between the positive and negative parts of the spectrum then inserting $N_\varphi(r)$ zeros in between the positive and negative halves. The inverse FFT is then taken to return to the azimuth domain. Through this process the circumferential spacing between

grid points is halved, restoring compliance with the maximum arc-length separation specification, and starting field values are defined for each new radial path.

The pressure field is 2π continuous in each ring in the MONM3D computation grid making it very suitable for this interpolation approach based on the Fourier transform. For signal processing purposes, if $N_\varphi(r)$ is not a power of 2 then the signal is zero-padded to make the Fourier transform more efficient. In this case, a Tukey filter is then applied to artificially taper the edges of the 'signal' prior to taking the FFT.

3.3 MONM3D - Model Output

Propagation model results will be presented in this document using various analysis techniques. The results derived straight from the MONM3D output are in the form of transmission loss (TL) and will be presented in plots of TL either as a function of range for a single depth and azimuth, as a function of range and depth for a given azimuth, and/or as a function of azimuth and range for single depth. In addition to consideration of the TL, the techniques described in this section have also been applied in Chapter 5 for further interpretation of the model results.

3.3.1 Modal Decomposition

The structure of the total field computed with a PE model can sometimes be difficult to interpret and often it is useful to examine the behaviour of the individual normal modes that the field comprises. Since each mode is associated with a different initial angle of propagation, each mode is differently influenced by its interaction with the environment. Understanding of the behaviour of individual modes provides a basis for interpreting changes in the total field structure as sound propagates through an environment. The approach described here has been applied as a tool to interpret the PE fields generated for the Florida Strait test environment considered in Chapter 5.

The field output from a PE model can be separated into its modal components using an approach first introduced for spectral analysis of electromagnetic waves in optical waveguides [22] which involves taking the transform of a PE amplitude correlation function into the wavenumber domain [20, 49]. The decomposition can be applied at any desired range step; for this discussion it will be called r_0. An array of vertical complex pressure values is extracted from the field at range r_0 and is used as

the starting field for an investigative 2D PE model run. 2D calculations are then carried out to some range, r_d, in a hypothetical environment that is range independent and characterized by the local properties of the real environment at range r_0. The amplitude correlation function relating the complex pressure fields $p(r, z)$ at r_0 and r_d is written:

$$\Gamma\left(r_0, r_d\right) = \int_0^\infty \rho^{-1} p^*(r_0, z) p(r_d, z) dz \tag{3.18}$$

where * denotes the complex conjugate.

The field $p(r, z)$ can be written as a sum of normal modes:

$$p(r, z) = \sum_j a_j u_j(z) \exp(ik_j r) \tag{3.19}$$

where the a_j are the mode amplitudes and u_j are the eigenfunctions. The weighting factor ρ^{-1} in Equation (3.18) ensures that the eigenfunctions are orthonormal and the correlation function integral can then be written in the analytic form:

$$\Gamma\left(r_0, r_d\right) = \sum_j \left|a_j\right|^2 \exp\left(ik_j(r_d - r_0)\right). \tag{3.20}$$

Taking the Fourier transform of this equation then yields

$$F\{\Gamma\} = \int_0^\infty \Gamma(r_0, r_d) exp(-ikr_d) dr = \sum_j \left|a_j\right|^2 \delta(k - k_j) \tag{3.21}$$

indicating that the spectrum of Γ has peaks at the wavenumbers k_j with amplitudes a_j.

Using this approach the depth-variable sound field at any range, computed by a PE model, can be decomposed into the field's horizontal wavenumber components. Unlike other decomposition methods based on least-squares fitting or eigenvector decomposition, this approach does not require the separate use of a normal-mode model to compute the wavenumbers and eigenfunctions. By applying this method at a selection of ranges, the modal spectrum of a PE field can be monitored along a path from the source, and the emergence or reduction of different spectral components can be tracked as a function of range in any azimuthal direction.

3.3.2 Fourier Synthesis

Time-domain waveforms can be constructed using Fourier synthesis to simulate signal propagation through a model environment. This approach is used in Chapter 5 to reconstruct waveforms at a receiving array.

Consider that solutions $p(r, z, \omega)$ to the Helmholtz equation,

$$[\nabla^2 + k^2(r)]p(\mathbf{r}, z, \omega) = 0 \tag{3.22}$$

are the time harmonic solutions of the standard wave equation

$$P(\mathbf{r}, z, t) = p(\mathbf{r}, z, \omega)e^{-i\omega t} \tag{3.23}$$

where $P(\mathbf{r}, t)$ and $p(\mathbf{r}, \omega)$ are conjugate Fourier transform pairs

$$p(\mathbf{r}, \omega) = \frac{1}{\sqrt{2\pi}} \int_{-\infty}^{\infty} P(\mathbf{r}, t)e^{i\omega t}dt \tag{3.24}$$

$$P(\mathbf{r}, t) = \frac{1}{\sqrt{2\pi}} \int_{-\infty}^{\infty} p(\mathbf{r}, \omega)e^{-i\omega t}d\omega \tag{3.25a}$$

$$= \frac{1}{\sqrt{2\pi}} \int_{-\infty}^{\infty} S(\omega)g(\mathbf{r}, \omega)e^{-i\omega t}d\omega \tag{3.25b}$$

for Green's function $g(r, \omega)$ and source spectrum $S(\omega)$.

Using MONM3D results computed for a discrete band of frequencies, and given a source spectrum $S(\omega)$ defined over that band, waveforms in the time domain can then be constructed by performing an FFT of the fields $p(\mathbf{r}, z, \omega)$.

Chapter 4

Model Validation

This section contains MONM3D model results for two 'benchmark' test cases that demonstrate the accuracy of the Nx2D and the 3D portions of the code. The results are compared against values obtained using the 3D PE model PECan, which has itself been validated against exact and benchmark solutions for various test cases[7]. Results obtained with the 2D PE model RAM [13] are also presented to highlight the 3D effects.

4.1 2D Flat-Bottom Validation Test

MONM3D results for a simple benchmark problem, that does not contain 3D effects, illustrate the accuracy of the Nx2D portion of the range-stepping algorithm in MONM3D. The test case is the Flat Test Case 3A from the 1981 NORDA Parabolic Equation Workshop [18]. The test case environment consists of an isospeed water column with sound speed $c_w = 1500$ m/s and density $\rho_w = 1.0$ g/cm^3 with a constant water depth of 100 m. The seafloor is modelled as a homogeneous half-space with sound speed $c_b = 1590$ m/s, density $\rho_b = 1.2$ g/cm^3 and bottom attenuation $\alpha = 0.5$ dB/λ. A 250 Hz point source is placed at a depth of 50 m.

Transmission loss values as a function of range for a receiver at 50 m depth are shown in Figure 4.1 as computed using three separate PE models and one normal mode code. The maximum range of propagation for this test case is 10 km. The results from MONM3D are plotted with a solid black curve. For comparison, results using RAM are shown with the dashed blue curve and results from PECan are plotted with a dotted red curve. All three models show excellent agreement. The MONM3D

and RAM results are in exact agreement, which is expected since the Nx2D portion of MONM3D is based on the RAM algorithm. Finally, results from the normal mode code Kraken [39] are also plotted with a dashed green line. The Kraken solution can be considered exact for this case and is in excellent agreement with each of the other three models.

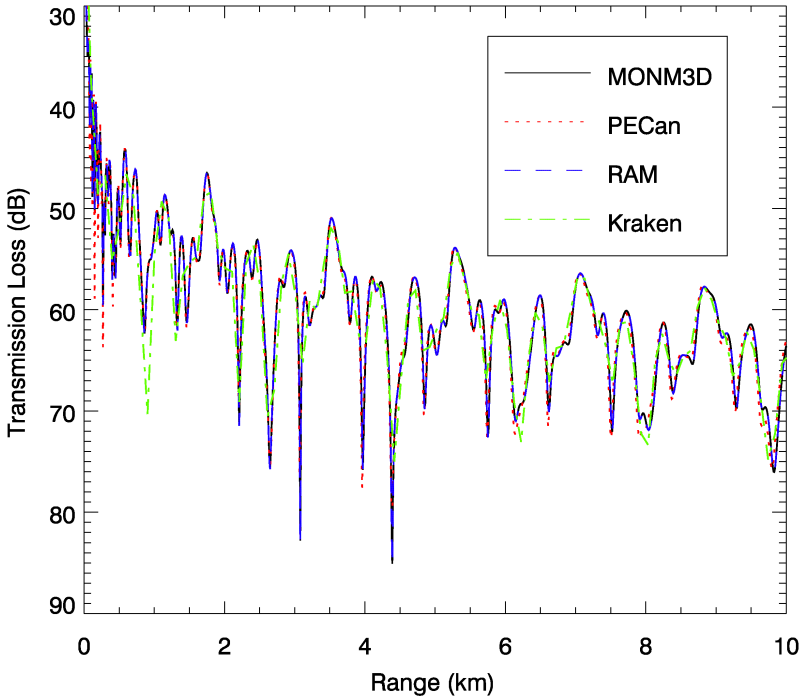

Figure 4.1: Transmission loss as a function of range for a 250 Hz point source in the 1981 NORDA PE Workshop Flat Bottom Test Case 3A. 2D results are shown for three different PE models: MONM3D (solid black), PECan (dotted red) and RAM (dashed blue), and one normal mode code, Kraken (dash-dotted green).

4.2 Truncated Wedge Validation Test

This section presents results that demonstrate the accuracy of MONM3D for an environment containing bathymetry that gives rise to 3D effects. The test environment considered here is described as a truncated wedge and is a modified version of the 2D ASA penetrable wedge benchmark problem [32]. This adaptation, designed for 3D

considerations, was considered by Fawcett[21] and has since been used as a benchmark for many 3D PE models [44, 7, 42].

The model environment consists of an isospeed water column with sound speed $c_w = 1500$ m/s and density $\rho_w = 1.0$ g/cm^3 overlying a sediment half-space with sound speed $c_b = 1700$ m/s, density $\rho_b = 1.5$ g/cm^3 and bottom attenuation $\alpha = 0.5$ dB/λ. A source is located at the center of the slope ($r = 0$) where the water depth is 200 m. The water depth increases linearly down-slope from the source a distance of 3600 m, beyond which the depth is constant at 380 m. Similarly, the water depth decreases linearly over 3600 m in the up-slope direction to a minimum water depth of 20 m. The seafloor slopes at an angle of 2.86°. The environment is shown graphically in Figure 4.2.

Consider a 25 Hz point source placed at a depth of 40 m. The following model parameters are defined identically in each PE model (MONM3D, PECan and RAM): $\Delta r = 10$ m, $\Delta z = 1$ m, and $n_p = 2$ (the number of Padé terms). Also, each model setup includes an absorbing sponge layer starting at a depth of 450 m below the sediment within which the bottom attenuation increases linearly to a value of 5.0 dB/λ at 600 m below the seafloor to prevent reflections from the bottom of the model grid.

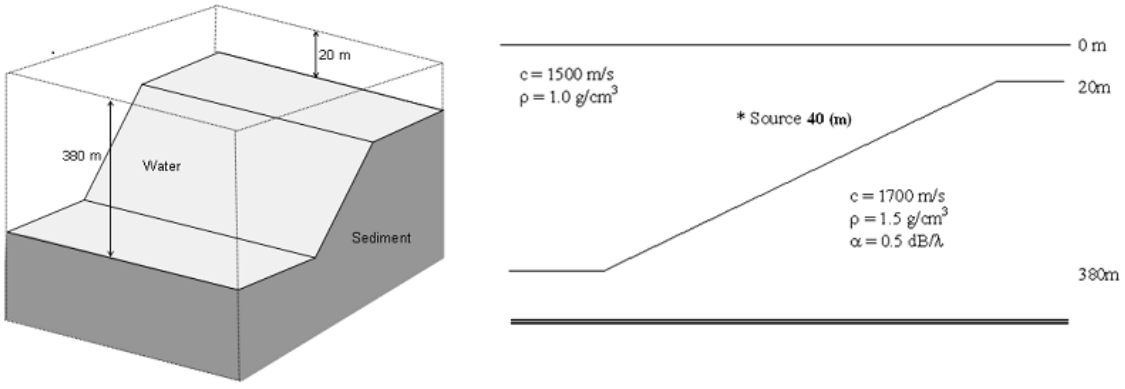

Figure 4.2: Model environment definition for the truncated wedge test case.

Figure 4.3 shows TL values as a function of azimuth at 2500 m range and 35 m depth, calculated using MONM3D with 720 points in azimuth for the truncated wedge test case environment. Also plotted, for comparison, is an interpolated field at 2500 m range obtained through up-sampling the 720 points onto a 1440-point grid using the zero-extending process described above. The two are indistinguishable in the plot

indicating that the interpolation scheme has not altered the original sample points, and has not introduced spurious artifacts into the field.

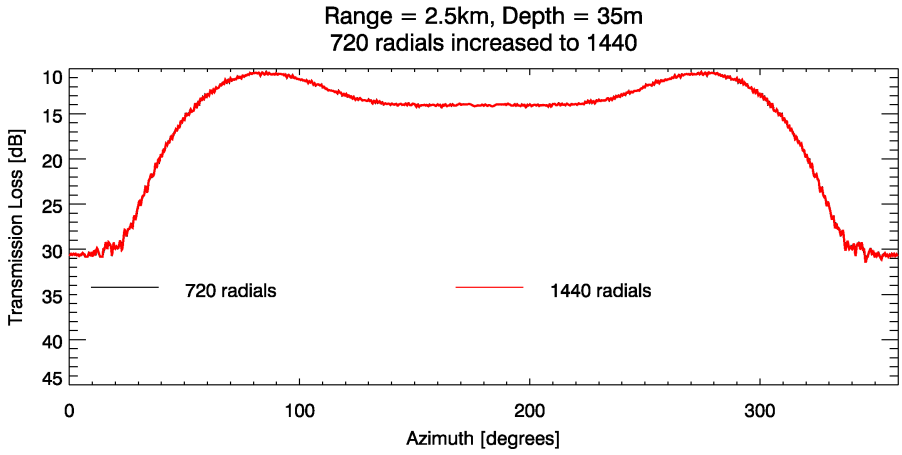

Figure 4.3: Transmission loss as a function of azimuth for a pressure-field at 2500 m range modelled using 720 points in azimuth (black) and an interpolated pressure field with 1440 points at the same range (red).

To further examine any potential influence on the field introduced through the tessellation approach, Figure 4.4 presents TL values as a function of azimuth for two model runs for the truncated wedge test case environment. One model run was performed without tessellation and included 1440 radial paths in the computation grid at all ranges. The computation grid for the second model run contained 720 radial paths for the first 80 steps of the algorithm (that is, to a range of 800 m). At this range an arbitrarily specified (for computation time convenience) acceptable arc-length separation of 8 m was exceeded. The field was thus interpolated onto 1440 radials. The curves shown in the plot present both of the 1440-point fields at 800 m range obtained from each model run (tessellated vs non-tessellated). The curves are in excellent agreement.

Sturm and Fawcett's [45] results using a fourth-order differencing scheme in azimuth indicated that 5760 radials were sufficient for this 3D problem. For a maximum range of 25 km, this corresponds to a maximum acceptable arc-length separation of 27 m. MONM3D was thus initiated in its tessellated configuration with 360 points in azimuth and with Δs_{max} set to 27. In this configuration tessellations (azimuthal grid size increases) occurred at the ranges indicated in Table 4.1. For comparison, MONM3D was also run without tessellation using a constant number of 5760 radials,

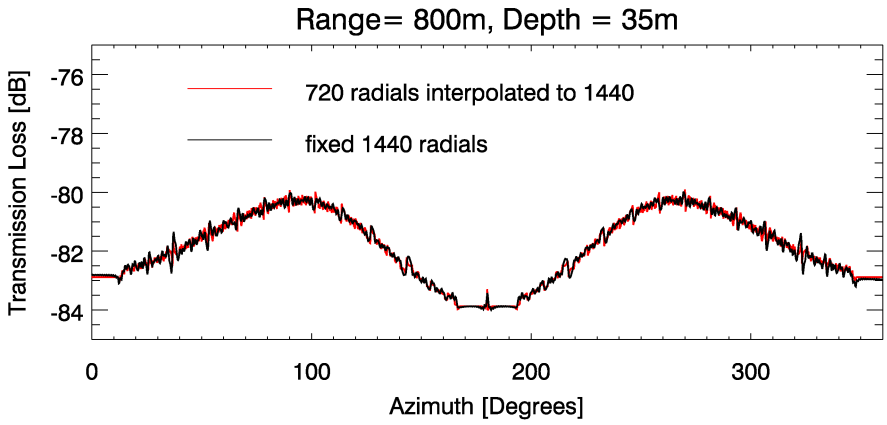

Figure 4.4: Transmission loss as a function of azimuth for a model run using a fixed number of 1440 radials (black) and for a tessellated model run with an increase in radial paths from 720 to 1440 radials involving interpolation at 800m range (red).

as was the 3D version of PECan. "Non-tessellated" MONM3D results were obtained with the maximum acceptable arc-length separation (Δs_{max}) set to 100000 and the initial number of radials set to 5760. With this configuration, the computation grid contained a fixed number of grid points in azimuth at all ranges.

Table 4.1: MONM3D tessellation points for truncated wedge test case with Δs_{max} set to 27.

Range	Number of Points in Azimuth
0 km	360
1.54 km	720
3.09 km	1440
6.18 km	2880
12.37 km	5760

Figure 4.5 shows TL in the horizontal plane at a depth of 30 m for an Nx2D run of MONM3D as well as for a full-3D, tessellated run. The source is located at the center of the maroon circle in the middle of each figure. The plots extend ±4 km from the source in the along-slope direction (up- and down-slope) and ±25 km from the source in the across-slope direction. It is noted that the 3D field results in the top panel

show a larger shadow area toward the top of the slope that extends further down-slope with increasing cross-slope range. This is due to horizontal refraction of sound in the down-slope direction. The interference patterns observed in the across-slope directions also differ between the Nx2D and the 3D fields.

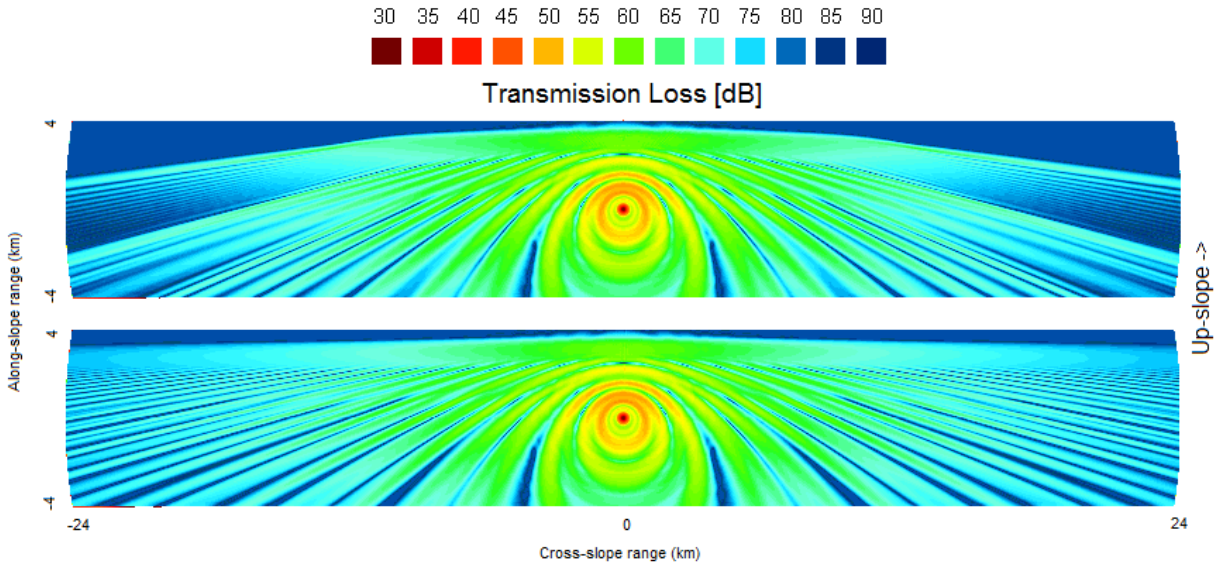

Figure 4.5: Transmission loss in the horizontal plane at 30 m depth for the truncated wedge test case from (bottom) Nx2D and (top) 3D calculations.

The above results are now considered along transects that extend away from the source following along-slope and cross-slope headings. Figures 4.6 and 4.7 show transmission loss as a function of range at 30 m depth in the up-slope and the cross-slope directions respectively. In the up-slope direction the 30 m receiver moves into the seafloor at a range of 3.4 km; therefore the maximum range plotted in this direction is 4 km. In the cross-slope direction transmission loss is plotted to a maximum range of 25 km. Each plot contains curves of the full-3D MONM3D results, both with and without the use of tessellation. A solid black curve of the 3D results obtained with PECan is also shown to validate the accuracy of the MONM3D calculations. Finally, results from the 2D model RAM are also plotted for comparison.

The 3D PECan and the MONM3D results are in excellent agreement for both transects. Also, the tessellated and non-tessellated MONM3D results in each figure are in exact agreement. Comparison of the 3D model results and the 2D model results in each plot reveals that the influence of 3D effects is dependent on the azimuthal heading relative to the orientation of the slope. Sound that travels directly up-slope

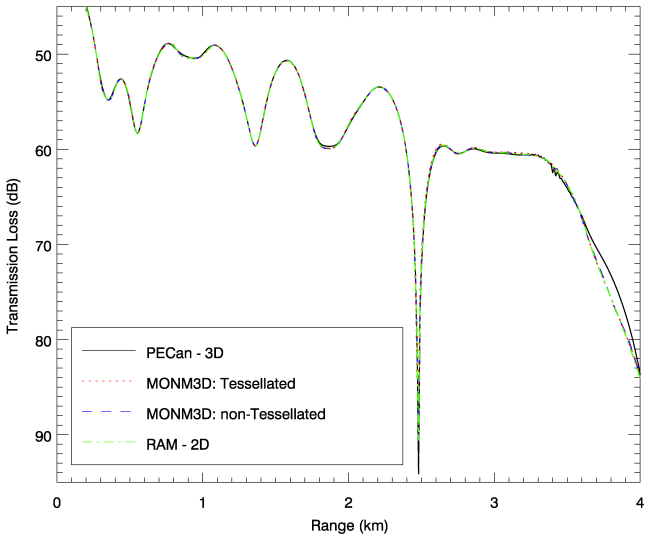

Figure 4.6: Transmission loss as a function of range in the up-slope direction at a depth of 30 m for the truncated wedge test case with a 25 Hz point source at 40 m depth.

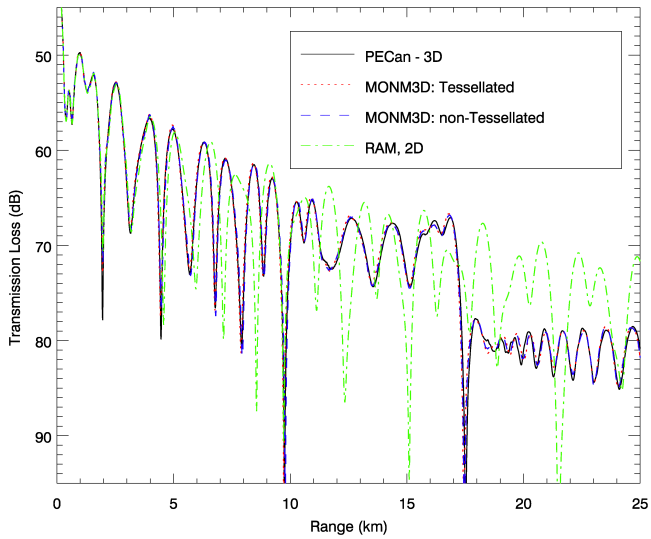

Figure 4.7: Transmission loss as a function of range in the cross-slope direction at a depth of 30 m for the truncated wedge test case with a 25 Hz point source at 40 m depth.

does not experience horizontal refraction and there are no 3D effects of the sound field in the up-slope direction. This is the reason that the 3D results in the up-slope direction obtained using both PECan and MONM3D are in excellent agreement with the 2D RAM results in Figure 4.6. By contrast, Figure 4.7 shows that the 3D results are very different from the 2D results for cross-slope propagation, particularly at ranges greater than 10 km.

The differences between the 2D and 3D results in the cross-slope direction can be examined more carefully through consideration of a vertical slice of the transmission loss as a function of range at all depths in the computation grid. Such range-depth slices obtained from an Nx2D version of MONM3D and from the full 3D version of MONM3D are presented in Figure 4.8.

The vertical slice plot for the Nx2D result is comparable to that for the 3D result out to a range of 4 or 5 km, beyond which the interference patterns in the two plots are noticeably different. The 3D result in Figure 4.8 above exhibits three distinct interference pattern regions; the first between 0 and 10 km range, the second between 10 km and 17 km and the third region beyond 17 km. These transitions in the 3D field pattern occur at ranges where there are changes in the mode composition of the field [44].

To better understand the origin of these transitions, and the behaviour of the individual modes, a 3D field calculation was carried using an extension of the normal mode code Kraken [39]. At the source position, where the water depth is 200 m, a 25 Hz source initiates three propagating normal modes. The horizontal trajectories for each of these three modes as calculated with the Kraken code are plotted in Figure 4.9 below. Trajectories are shown for sound paths that leave the source at a fan of headings between 15° and 135° clockwise from the up-slope direction.

The source is located at the point (0,0) in the plot. Following a line travelling away from the source and parallel to the across-slope axis (plotted in grey), the mode 3 trajectory paths (white curves) in Figure 4.9 do not extend beyond ∼10 km range. Similarly, the mode 2 trajectory paths (red curves) do not extend beyond ∼17 km range and the field beyond 17 km range only contains mode 1 trajectory paths (black curves). These ranges correspond with the interference pattern transition ranges that were identified previously for the 3D calculation in Figure 4.8 above. It is noted that there are also regions of the 3D plot in Figure 4.9 where different horizontal trajectory paths intersect. These regions represent areas of the field that exhibit both inter- and intra-modal interference which generates the patterns observed in Figure 4.8.

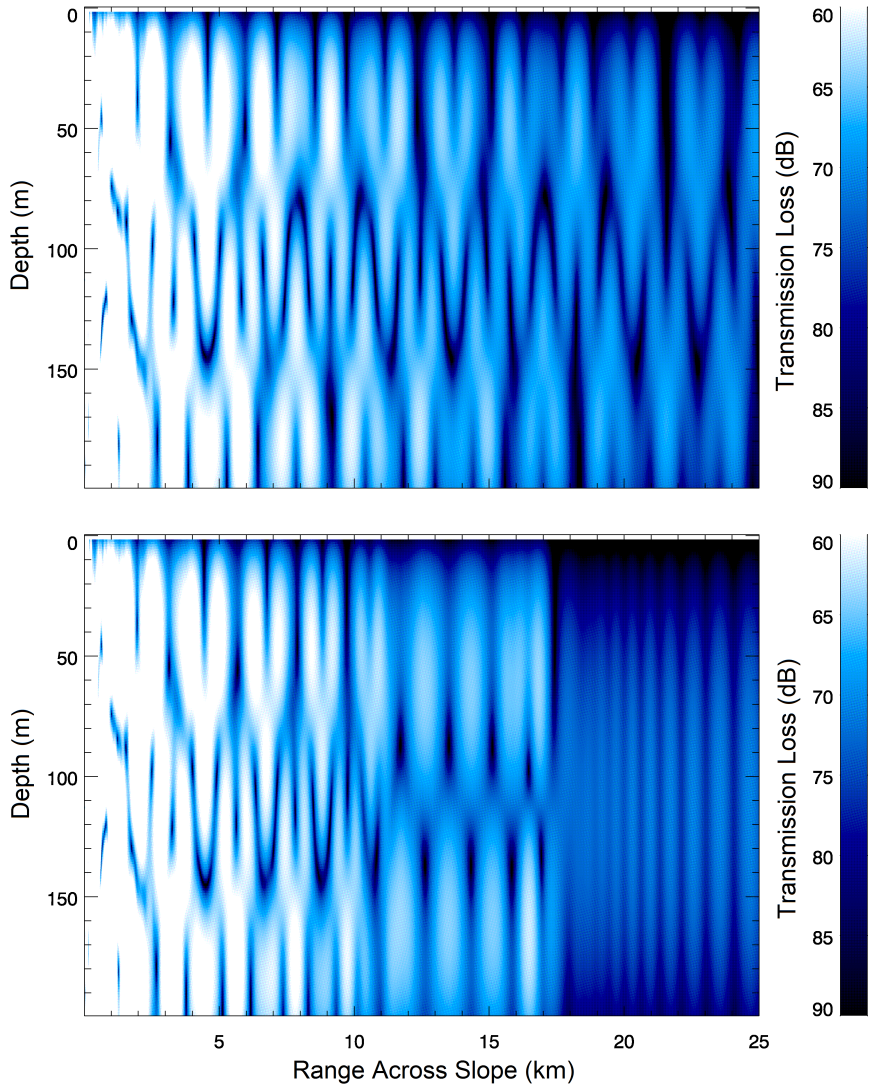

Figure 4.8: Transmission loss as a function of range and depth in the cross-slope direction for the truncated wedge test case with a 25 Hz point source at 40 m, obtained using MONM3D applying Nx2D calculations (top) and full 3D calculations (bottom).

Following the approach of Fawcett [21] the composition of the 3D PE field was investigated by propagating individual modes through the environment. To do this, the MONM3D starting field was defined using the functional form of the vertical

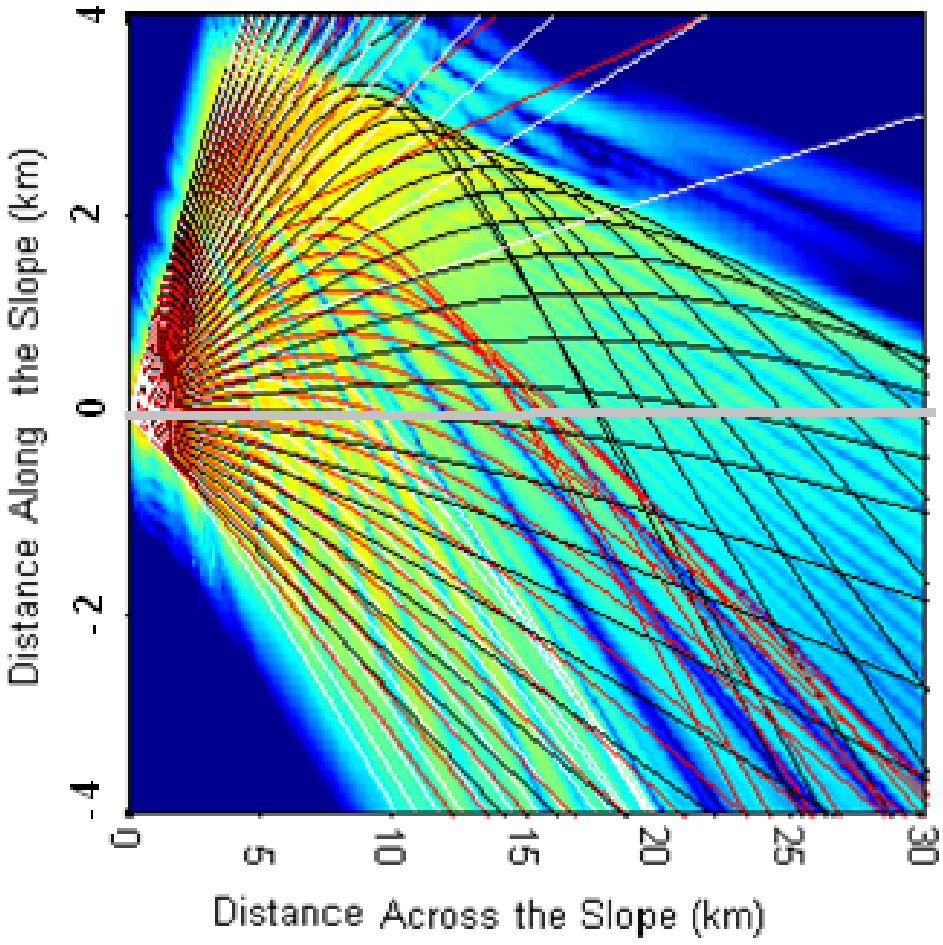

Figure 4.9: Horizontal trajectories obtained from a 3D field calculation based on the adiabatic normal modes computed using Kraken for the truncated wedge test case. Trajectories are shown for mode 1 (black), mode 2 (red) and mode 3(white).

mode shapes according to the equation:

$$u(0,\varphi,z) = \begin{cases} \sin(\gamma_w z) & ;\ 0 \le z \le z_b \\ \sin(\gamma_w z_b)\exp\left(-\gamma_b(z-z_b)\right) & ;\ z > z_b \end{cases} \tag{4.1}$$

where $\gamma_w = \sqrt{\frac{\omega^2}{c_w^2} - k_n^2}$ and $\gamma_b = \sqrt{k_n^2 - \frac{\omega^2}{c_b^2}}$, k_n is the n-th modal wavenumber and z_b is the bottom depth at the source location. For a transect heading from the source directly across slope, the water depth is constant at 200 m and three propagating modes are supported. MONM3D was configured to propagate outward from the source each of these three modes individually. For each mode, the PE reference sound

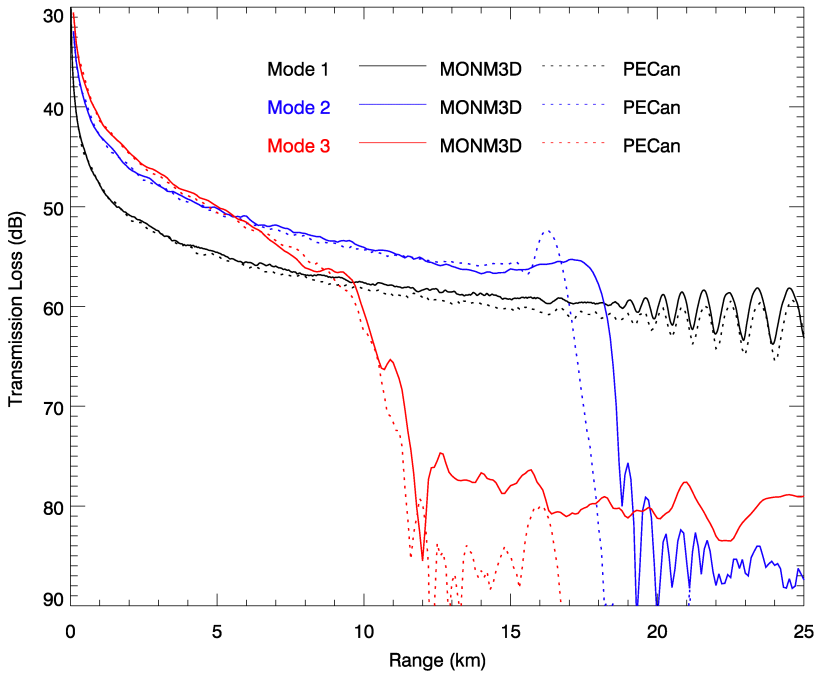

Figure 4.10: Transmission loss as a function of range for the propagation of individual modes in the cross-slope direction of the truncated wedge test case, obtained applying full 3D calculations using MONM3D and using PECan for comparison.

speed was set equal to the phase speed of the mode being modelled so that the phase errors inherent in PE approximations would not alter the modal propagation [44]. For mode 1 the PE reference sound speed was set to 1512.94 m/s, it was set to 1554.44 m/s for mode 2 and 1632.42 m/s for mode 3.

Figure 4.10 shows TL versus range in the cross-slope direction for each of the three individual modes as generated using the modal starting field and the tessellated version of MONM3D. Results generated using PECan are also plotted for comparison. The results from the two 3D PE models are in very good agreement.

In this wedge environment horizontal refraction focuses the sound energy down-slope. Sound rays leaving the source, with initial horizontal headings that are obliquely up-slope, follow paths that are refracted toward the down-slope direction. The amount of down-slope refraction is a function of the initial horizontal heading of the sound ray paths and of the initial vertical angle of propagation, which also corresponds with mode number. Due to this down-slope refraction there are shadow zones associated with each mode. The ranges to the shadow zones in the cross-slope direc-

tion for modes 1, 2, and 3 are indicated by the sharp level drops in the transmission loss curves in Figure 4.10. Images of vertical slice of TL versus range and depth for each mode are shown in Figure 4.11.

Higher-order modes propagate at steeper vertical angles and are more strongly influenced by the sloping bathymetry that is responsible for the horizontal refraction. Hence higher-order modes turn more sharply toward the down-slope direction and the shadow zone for mode 3 occurs closer to the source than that for mode 2 or for mode 1. The observed shadow zone cut-off ranges for each mode correspond with the transition zone points in the 3D range-depth plot that was shown in Figure 4.8. The first region (0-10 km range cross-slope) contains inter-modal interference of all three modes, as well as intra-modal interference of different mode 3 trajectories. It is the self-interference of the mode 3 trajectories that causes the differences of the 3D and the Nx2D fields at ranges < 10 km. The second region (10 - 17 km range cross-slope) contains inter-modal interference of modes 1 and 2 as well as intra-modal interference of different mode 2 trajectories. The final region (> 17 km) exhibits the self-interference of different mode 1 trajectory paths, resulting in the modulation of the mode 1 transmission loss curve in Figure 4.10 at the longer ranges.

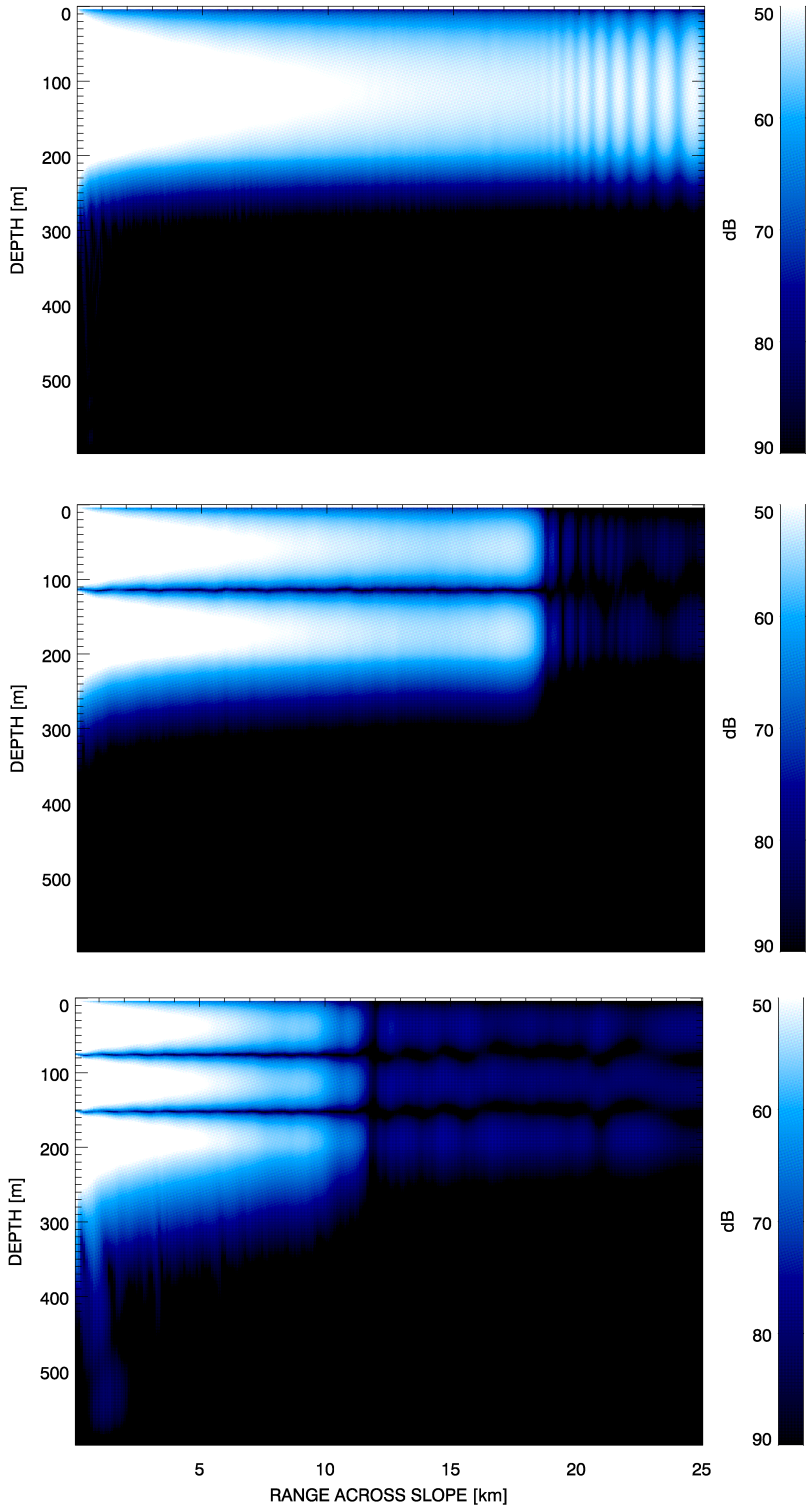

Figure 4.11: Transmission loss as a function of range and depth in the cross-slope direction for mode 1 (top), mode 2 (middle) and mode 3 (bottom) in the truncated wedge test case with a 25 Hz point source at 40 m.

Chapter 5

Florida Strait Test Environment

The physical test case that has been modelled using MONM3D involves a coastal environment near the South Florida Ocean Measurement Center in the Florida Straits. Prior investigations of acoustic propagation at this site led to a hypothesis that the shoreward slope of the seafloor gives rise to an acoustic field that is influenced by 3D, out-of-plane, propagation [33, 46]. However the important environmental influences on the sound propagation were not fully described. The MONM3D model has been applied to further investigate the propagation regime at this site.

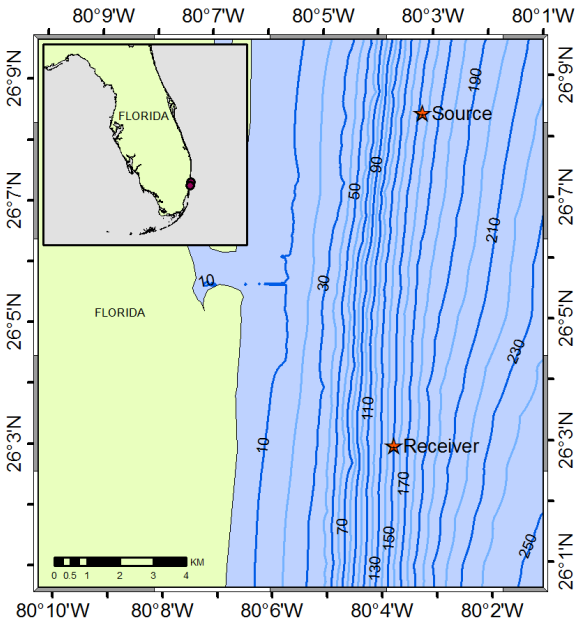

Figure 5.1: Florida Strait test case environment.

In 1999 deFerrari et al. [38] collected TL data at this site using a vertical receiving array deployed at 10 km range from a moored deep-water acoustic source. The source and the receivers lay in a plane oriented parallel to the shore with nearly constant bathymetry between 150-160 m depth, as illustrated in Figure 5.1. The source transmitted M-sequence coded pulses at centre frequencies between 100 and 3200 Hz. High-sensitivity data were received at 13 hydrophones on the receiving array corresponding to the depths in Table 5.1. The M-sequence for each carrier frequency was designed with a period of approximately 2.55 s and a digit length determined by the 'q' factor of the transducers (the ratio of the carrier frequency to the bandwidth), which was 4 for all frequencies. This means there are 4 carrier cycles per digit in the sequence. The M-sequence was repeated for an hour at each center frequency. Received signals were coherently averaged for 1 minute and the pulse responses were obtained through a Hadamard transform. At frequencies below 800 Hz the received signals consisted of a set of primary arrivals that were followed by a strong set of secondary arrivals with a time separation of approximately 0.4 seconds [38].

Table 5.1: Receiver depths with data available for the Florida Strait test case.

Hydrophone	depth (m)	Hydrophone	depth (m)	Hydrophone	depth (m)
1	40.0	6	54.0	10	118.0
2	44.0	7	73.0	11	124.0
3	45.0	8	80.0	12	129.5
4	47.5	9	110.0	13	137.0
5	50.0				

In a subsequent geoacoustic inversion study, Jiang et al. [33] were unable to determine a geoacoustic model that matched the late arrivals in the received pulses using a 2D forward model. They speculated that the strong secondary arrivals originated from horizontally-refracted sound paths which initially travelled away from the source along a shoreward heading. Such arrivals lag the direct (source to receiver) primary arrivals due to their longer propagation paths. Through vertical beam-forming Jiang et al. showed that the propagation angles contributing to the secondary arrivals were steeper than those for the predominantly low angle primary arrivals. This allowed them to filter the data to shallow arrival angles (less than 8° from horizontal) and

to conduct the geoacoustic inversion using only the primary arrival data, assumed to travel in the source-receiver plane.

A 3D acoustic modelling study was later conducted by Sturm et al. [46] to validate the assumption that the propagation paths for the secondary arrivals travelled out of the source-receiver plane. Sturm used Fourier synthesis to reconstruct the waveforms and simulate the transmitted pulses using 2D and 3D solutions to the parabolic wave equation. The results from the 3D calculations did predict strong secondary arrivals that were absent in the 2D simulations. However the characteristics of the 3D-simulated secondary arrivals did not exactly match those observed in the measured data. Specifically, the time delay between the primary and secondary peaks was overestimated in the model simulation, and the arrivals were noted to occur at all depths in the water column although the measured data recorded their presence more strongly in the top of the water column. Nevertheless this result did provide support for the hypothesized 3D propagation effects.

This present investigation has been carried out to build on the work of Sturm et al. and to characterize more specifically how out-of-plane sound paths contribute to the measured waveforms. This investigation is of interest specifically to those conducting experiments at the Florida Strait test site, but more broadly provides a practical example to explore the influence of the 3D propagation effects in a realistic coastal environment.

MONM3D has been configured using several geoacoustic definitions and the results have been interpreted to better understand the influence that the environment has on the sound propagation. A new development in this investigation has been the introduction of a range-variable geoacoustic model in which the properties of the environment vary as a function of offshore range. Fourier synthesis has been applied to simulate the waveforms received at 10 km range for each model configuration. Techniques have been implemented to decompose the computed PE fields into their modal components and the simulated waveforms have been considered in terms of the mode arrival structure.

From this analysis I have been able to:

- Comment on the model-data mismatch for the secondary arrivals observed by Sturm,
- Characterize the propagation paths responsible for the secondary arrivals,

- Comment on how the environmental parameters influence the nature of the secondary arrivals.

5.1 Model Environment

5.1.1 Sound Speed Profile

The sound speed profile input to the model, shown in Figure 5.2, was derived from measurements collected in the source-receiver plane during the 1999 propagation loss experiment [33]. The top of the profile (to a depth of 80 m) is essentially isospeed, below which there is a strongly downward-refracting structure that creates a duct at the bottom of the water column for low order modes.

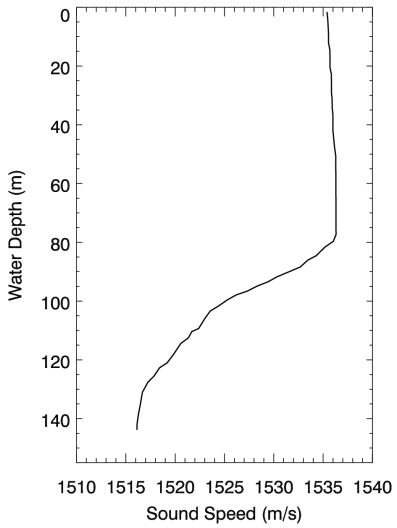

Figure 5.2: Sound speed profile used as model input for Florida Strait test case.

The gradient of the downward-refracting portion of the sound speed profile traps modes that propagate with grazing angles shallower than θ_{max}, defined from Snell's law as

$$\theta_{max} = \cos^{-1}\left(\frac{c_s}{c_i}\right) \tag{5.1}$$

where c_s is the sound speed at the source depth (1523.6 m/s) and c_i is the sound speed at the depth of the thermocline (1536.3 m/s). Substituting these values, this lower sound channel will only trap modes with propagation angles less than 7.4°. The

mode propagation angles can be approximated from the equation:

$$k_r = k\cos\theta_n = \frac{\omega}{c}\cos\theta_n \tag{5.2}$$

$$\theta_n = \cos^{-1}\left(\frac{c}{\omega}k_r\right) \tag{5.3}$$

for horizontal wavenumber k_r, angular frequency ω, sound speed c and grazing angle θ_n. At 100 Hz, mode 1 has wavenumber $k_r = 0.4121$ m^{-1} at the source range. Setting $c = 1523.6$ m/s gives $\theta_1 = 2.1°$. For Mode 2 $k_r = 0.4086$m^{-1} and $\theta_2 = 7.8°$. This means that modes 2 and higher escape this bottom sound channel.

The structure of the sound speed profile was assumed to be constant over the modelled region but the profile was truncated from the bottom with decreasing water depth. This shoreward profile truncation is consistent with sound speed profile measurements collected in 2007 by Heaney et al. [29] during an unrelated study at a nearby location.

5.1.2 Bathymetry

Bathymetry data for the model were obtained from the NOAA NGDC US Coastal Relief Model [8] online database and are shown in Figure 5.3. This dataset has a 3 arc-second resolution and the water depth at each model grid point was obtained through bilinear interpolation of the bathymetry data.

Unlike the constant slope of the standard 'wedge' environment from Section 4.2, the seafloor in this environment exhibits a variable shoreward slope. Figure 5.4 shows the bathymetry profile between the source and the shore. Within 750 m of the source the seafloor slopes toward shore at an angle of 2.5°, then the slope increases to an angle of 4° for approximately 1 km before reaching a much shallower slope less than 1° at the near-shore ranges.

It is instructive to consider horizontal ray paths for modes travelling over this variable slope as a basis for interpreting the output from the PE model. In Section 2.1 it was shown that propagation paths travelling over a constant slope follow hyperbolic arcs. In the Florida Strait environment the propagation paths that travel towards shore will be differently influenced by different parts of the slope and will not trace perfect hyperbolas. The expected propagation paths in this test environment were estimated by approximating the shoreward bathymetry profile (to the top of the steep slope) using two segments of constant slope: a 750 m segment with 2.5° slope and an

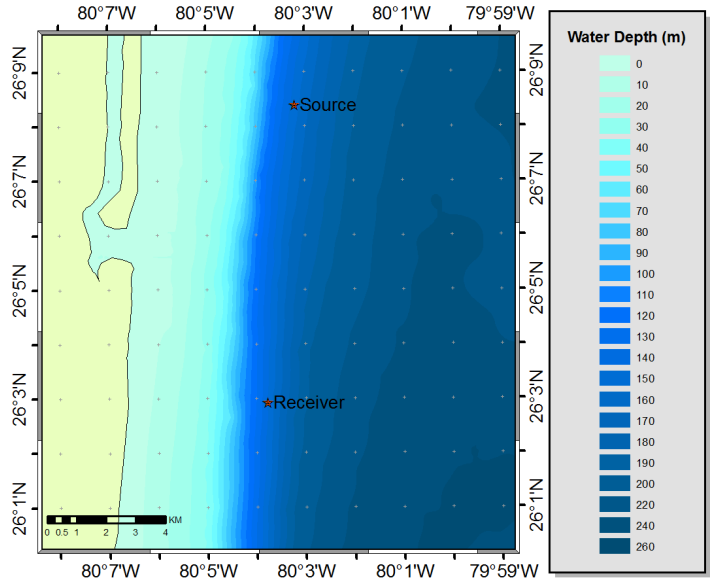

Figure 5.3: Bathymetry used as model input for Florida Strait test case.

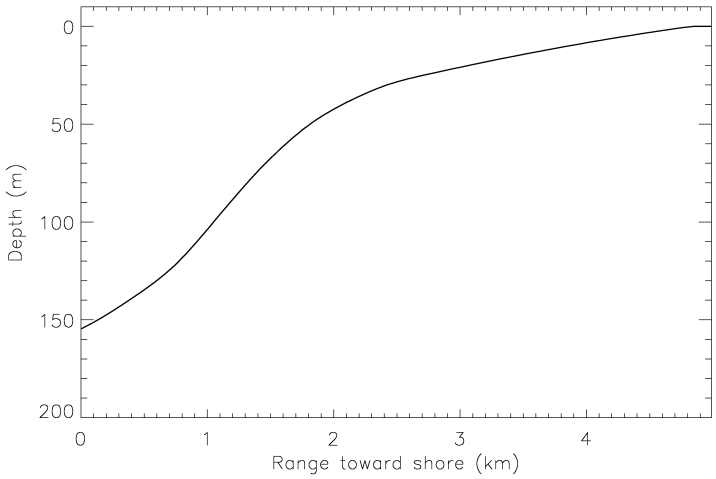

Figure 5.4: Bathymetry profile for Florida Strait test case showing water depths along a track up-slope from the source to the shore.

adjoining 1 km segment with a slope of 4°. Horizontal ray paths for each slope segment were computed using Harrison's equation for horizontal rays in a wedge environment (Equation (2.5) from Section 2.1) and the results were combined to predict the total propagation paths.

The Harrison equation requires initial propagation angles in the vertical and hor-

izontal planes. The vertical launch angles were defined to correspond with the mode propagation angles of the first eight modes. These angles were calculated from the mode horizontal wave numbers computed using the Kraken normal mode model [39] for the local environment at the source using the geoacoustic parameters from the initial inversion study čitejiang. Using these angles, the Harrison equation was applied to trace propagation paths over the shallow slope segment for a fan of horizontal launch angles between 0° (up-slope) and 90° (cross-slope). The resulting paths for each mode are plotted in black in the panels of Figure 5.5. In each panel of this figure the upper, darker green line indicates the source-receiver plane and the lower, lighter blue-green line marks the top of the steep-slope segment. The "shallow-slope paths" (black curves) for modes 1 through 4 only deviate very slightly from straight line, in-plane propagation. The black curves for modes 5 through 8 are noted to experience more refraction due to their steeper mode angles.

Paths that travel toward the steep-sloped segment encounter a change of slope at the segment interface and experience a path deviation. At this transition to the steep-sloped segment, the value for y_0 in the Harrison equation was updated to model a slope of 4°. New vertical launch angles were calculated based on the local mode functions at the transition point and the horizontal propagation angles were held fixed across the slope transition. These angles were used to launch the path continuations traced over the steep-sloped segment that are shown in blue in Figure 5.5. Many of these paths refract in the steep-sloped segment and turn back toward the source-receiver plane. At the points where these refracted paths re-enter the shallow-sloped segment the propagation angles were updated accordingly and the Harrison equation was applied once again for the shallow-slope segment. These paths are plotted in red in the figure. Paths that do not turn within the steep portion of the slope will continue in a shoreward direction. They will not return to the source-receiver plane within 10 km range (the location of the receiving array) and, therefore, are not of interest here. These paths are not plotted to avoid cluttering the plot.

The stars in the panels indicate the cross-slope ranges at which the out-of-plane paths first couple into the source-receiver plane. This occurs at shorter ranges for the higher-order modes than for the lower-order modes; for example 0.07 km range for mode 8 and 8.3 km range for mode 2. Mode 1 does not exhibit any out-of-plane coupling at the 10 km receiver range but for all other modes separate sets of arrivals are expected at 10 km range; the first set from the shallow-slope paths (all-black curves) and the second set from the steep-slope paths (black/blue/red curves). At

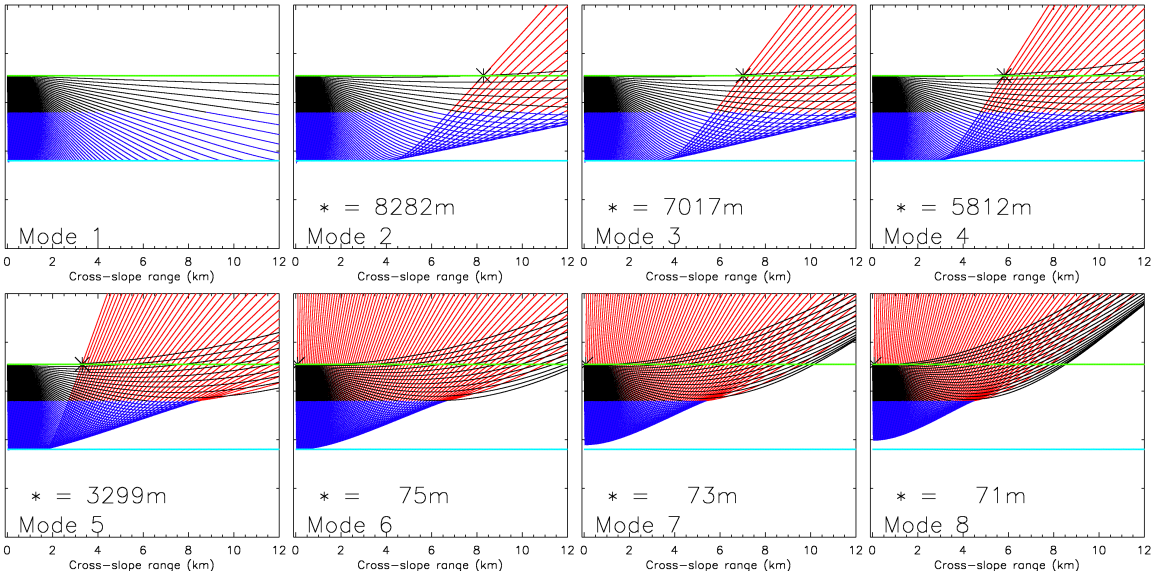

Figure 5.5: Horizontal propagation paths for each mode in the Florida Strait test environment for paths travelling up-slope from the source-receiver plane (green line) to the top of the steepest part of the shoreward slope (light blue-green line).

10 km range the time separation between these sets of arrivals will be shorter for the higher modes since the up-slope deflection of these interfering paths is smaller for higher-modes than for the lower-modes. It is noted that there is a caustic of refracted mode 7 paths at 10 km so a strong signal due to mode 7 can be expected at the receiver range. Mode 8 refracts out of the source-receiver plane and is no longer present in the plane beyond 8.5 km range. Mode 7 disappears from the source-receiver plane just beyond 10 km range. The other modes also exit the plane at longer ranges. At the caustics for mode 7 and mode 8 several different shallow-slope paths intersect so multiple arrivals of different shallow-slope paths are expected at these ranges.

5.1.3 Geoacoustics

An incomplete or inaccurate model of the acoustic environment can lead to model-data mismatch. The water-column sound speed and the bathymetry data used in the model were assumed to be fairly well defined since they were derived from measured data. However, since less is known about the geoacoustic properties of the seabed some thought was given to potential alternate geoacoustic definitions. In particular, the compressional attenuation and the shear parameters were found to be weakly

constrained in the Jiang et al. inversion [33] so focus was given to these parameters. Five geoacoustic models will be described here, each of which was applied separately in MONM3D for a comparative analysis.

Base Model Case

Very little is known about the geoacoustic properties at the study site aside from the inversion work conducted by Jiang et al. [33]. Sturm's model for this environment [46] included the range-independent geoacoustic halfspace from the Jiang et al inversion. The same parameter values are applied as a 'base case' for the present model investigation and are shown in Table 5.2. An artificial absorbing layer is placed at the bottom of the model grid between 650 and 1000 m below the seafloor. Within this layer the absorption increases with a linear gradient to a maximum value of 5 dB/λ to avoid the effect of artificial reflections from the boundary of the numerical grid. This geoacoustic model contains no shear parameters and has a very low value for compressional attenuation. Such a model is representative of very fine grained sand [31].

Table 5.2: Geoacoustic parameters used as the 'base case' in MONM3D for the Florida Strait test environment.

depth (m)	ρ (g/cm^3)	c_p (m/s)	α_p (dB/λ)	c_s (m/s)	α_s (dB/λ)
0	1.779	1676.0	0.05	0.0	0.0
650	1.779	1676.0	0.05	0.0	0.0
1000	1.779	1676.0	5.0	0.0	0.0

Model Case A

It is not likely that the Florida Strait environment is conducive to the deposition of fine grain sands due to the very strong Gulf Stream current and due to the absence of a viable nearby terrigenous source of such sediments (John Goff, personal communication, 2011). Therefore a geoacoustic profile was constructed that contains a higher value for the compressional attenuation as would be expected for coarser grained sands. This was done to assess the influence that this compressional attenuation has on the 3D field. This profile, shown in Table 5.3, is referred to as model

case A. Parameter values that differ from the base case are bolded and shown in red in the table.

Table 5.3: Geoacoustic parameters used for model case A for the Florida Strait test environment with coarser grained sands.

Case	depth (m)	ρ (g/cm^3)	c_p (m/s)	α_p (dB/λ)	c_s (m/s)	α_s (dB/λ)
A	0	1.779	1676.0	**0.6**	0.0	0
	650	1.779	1676.0	**0.6**	0.0	0
	1000	1.779	1676.0	5.0	0.0	0

Reflection-coefficient curves as a function of grazing angle were calculated for the base model case and model case A, these are shown in Figure 5.6. The propagating modes in this test environment correspond to mode angles less than approximately 20°. The higher-order propagating modes are associated with larger grazing angles. From the curve for model case A it can be seen that these higher-order propagating modes will experience more reflection loss than the low-order propagating modes when the compressional attenuation is increased.

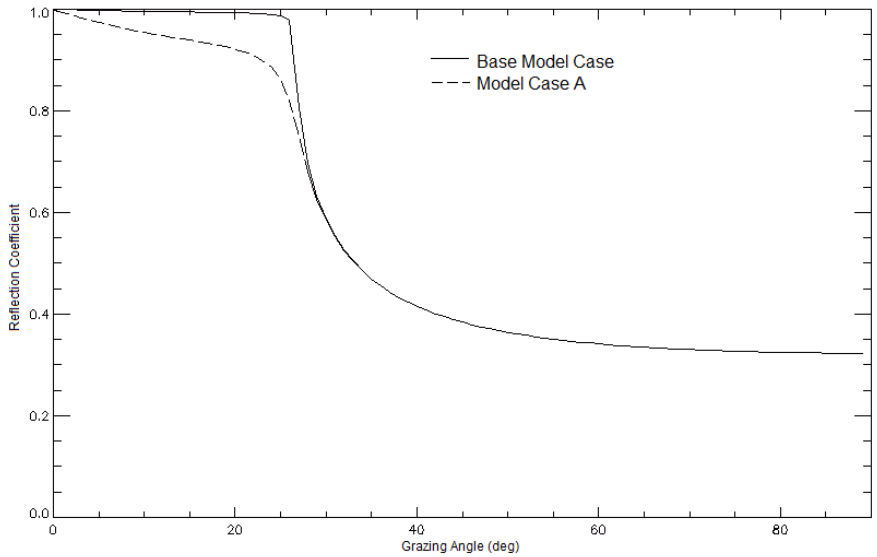

Figure 5.6: Reflection coefficient as a function of grazing angle for the base model case and for model case A.

Model Case B

Coarser grained sediments could also be capable of supporting shear propagation. Therefore a separate geoacoustic profile was constructed to investigate the influence of adding shear to the model; this will be referred to as model case B. This profile is shown in Table 5.4, again parameter values that differ from the base case are bolded in red. In model case B the compressional attenuation has been slightly increased from the base case since it would be unrealistic to expect sediment with very low attenuation to support shear propagation. This small increase of the compressional attenuation alone does not significantly alter the base case results and model case B is considered to illustrate the influence of shear only.

Table 5.4: Geoacoustic parameters used for model case B for the Florida Strait test environment with coarser grained sands.

Case	depth (m)	ρ (g/cm^3)	c_p (m/s)	α_p (dB/λ)	c_s (m/s)	α_s (dB/λ)
B	0	1.779	1676.0	**0.1**	**350.0**	**4.0**
	650	1.779	1676.0	**0.1**	**350.0**	**4.0**
	1000	1.779	1676.0	5.0	**350.0**	**4.0**

The reflection coefficient curve for model case B is plotted in Figure 5.7. In this case the highest- and lowest-order modes are least affected by the addition of shear to the profile and the modes in between are more strongly attenuated.

Model Case C

The base case environment consists of a homogeneous seafloor with a single geoacoustic layer. As was previously noted, the inversion study from which the base case parameters are obtained [33] was restricted to information from the shallow-angle primary arrival data. These shallow-angle propagation paths do not penetrate very deep into the seafloor and therefore these data do not contain information about the deeper seafloor structure. The ray path diagram in Figure 5.5 indicates that modes 2 through 8 contribute to the 3D propagation effect. Since these higher-order modes travel at steeper propagation angles, it is important that the geoacoustic definition also be appropriate for modes that penetrate more deeply into the seafloor.

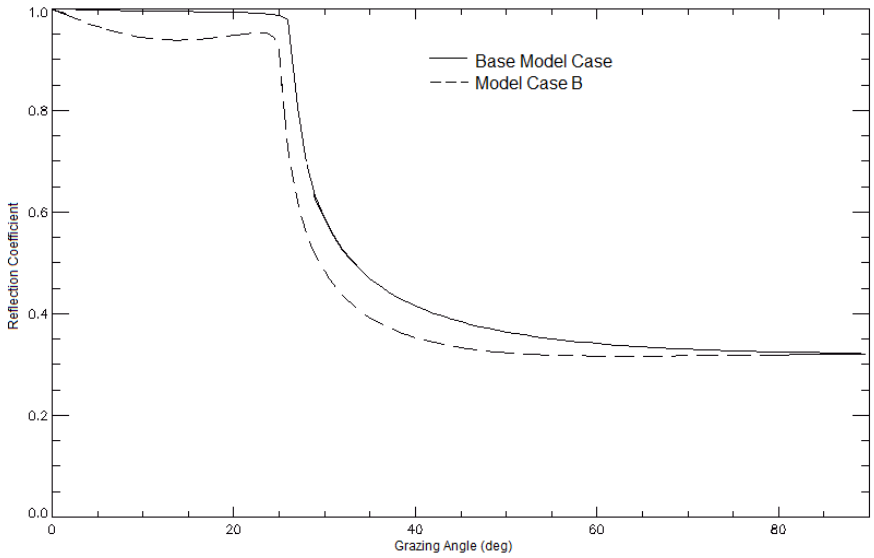

Figure 5.7: Reflection coefficient as a function of grazing angle for model case B and the base model case.

A review of the literature on the geology of the surrounding area was conducted to determine a realistic estimation for the deeper seafloor structure [37, 9]. The study location is located along the Florida-Hatteras slope. Slightly further offshore from the study location, at water depths greater than approximately 250 m, lies the Miami Terrace which consists of limestone outcrops. It is reasonable, therefore, to assume that there may be a presence of limestone beneath the seafloor in the study area. In 1965 core samples were collected from drilling on the Florida-Hatteras slope at locations several kilometres north of the study location, off of Jacksonville, Florida [9]. In one of these cores (hole J2), sampled at the top of the slope, consolidated limestone and dolomite were encountered at a depth of 150 m below the seafloor. In a core collected near the bottom of the slope (hole J5) alternating layers of limestone and unconsolidated calcareous ooze were found starting at a depth of approximately 67 m beneath the seafloor sediments. These cores indicate that a relatively thick sediment layer should be defined for this model case.

The thinner the sediment layer, the more likely it is that the propagating modes will be influenced by the presence of the limestone. Therefore a sediment thickness was chosen to represent the minimum thickness that is realistic based on the aforementioned core samples, but also conservative in terms of estimating the influence of a deep limestone layer. For this case a 50 m thick sediment layer (with geoacoustic

parameters from the base model case) was placed over top of a homogeneous layer with properties consistent for limestone [24].

To get an idea of the expected influence of the high sound speed limestone layer, the mode functions under this model parametrization were generated using the ORCA normal mode code [54] with a water depth of 155 m. The addition of the limestone layer increases the number of propagating modes from 9 in the base case to 23 for the layered seafloor. Based on the ray path diagram from Figure 5.5 it is not expected that modes higher than mode 8 will contribute to the 3D field at 10 km range in the source-receiver plane since that range is within the expected shadow zone for those modes. The mode functions calculated with ORCA for the first ten modes are shown in the left panel of Figure 5.8 plotted to a depth of 205 m below the sea surface, which denotes the sediment-limestone interface for this model case. It is noted that the penetration depths for modes 8 and lower do not reach to the layer interface and these modes are not expected to be influenced by the presence of the limestone layer. The shear-wave velocity in limestone is approximately 1600 m/s. Unfortunately this value is too high to be modelled using the complex density approximation and therefore shear cannot be included in this model case. To investigate the consequences of this neglect of shear, ORCA was also used to compute the mode functions without including shear, these are plotted in the right hand panel of Figure 5.8. The mode functions for the first 8 modes do not change with the exclusion of shear. The goal of this analysis is to consider the field at 10 km range, which is expected to be dominantly composed of contributions from modes 1 through 8. Since these modes are not influenced by the neglect of shear in the limestone, for the purposes of this simulation it is considered acceptable to neglect shear in the limestone layer.

The model parameters that were applied for this model case C are shown in Table 5.5.

Table 5.5: Geoacoustic parameters used for model case C for the Florida Strait test environment with a limestone layer beneath 50 m of sediment.

Case	depth (m)	ρ (g/cm^3)	c_p (m/s)	α_p (dB/λ)	c_s (m/s)	α_s (dB/λ)
C	0	1.779	1676.0	0.05	0.0	0.0
	50	**2.4**	**3000**	**0.1**	0	0
	650	**2.4**	**3000**	**0.1**	0	0
	1000	**2.4**	**3000**	**5.**	0	0

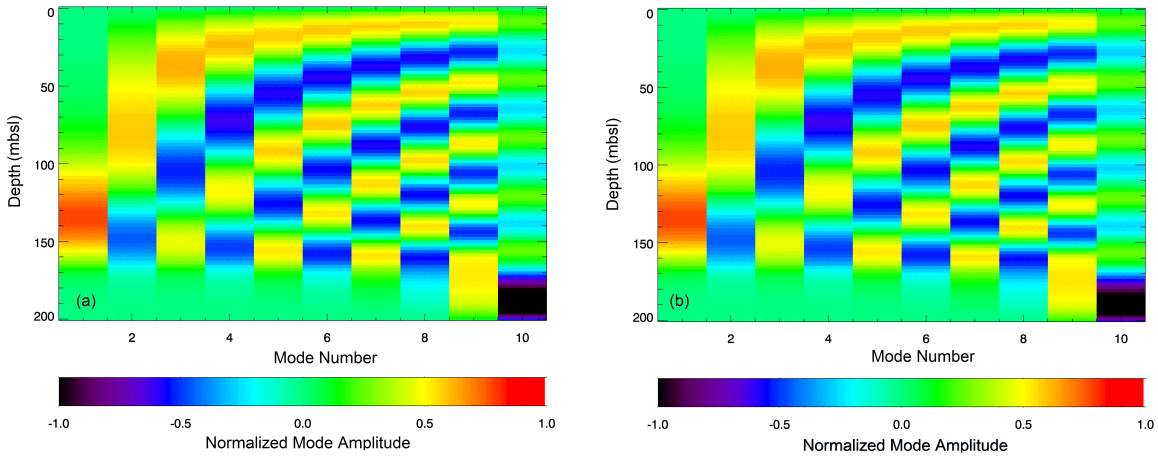

Figure 5.8: Mode functions for the first 10 propagating modes for model case C with 50 m of sediment over limestone with shear (a) and without shear (b).

Model Case D

Finally, it was considered that natural sediment sorting is likely to occur as a function of range from the shore and location along the slope, with coarser sediment expected closer to shore at the top of the slope. In this case, rather than applying range-independent geoacoustic parameters, a model was configured in which these parameters were allowed to vary with range in the up-slope direction. In this interpretation the Jiang et al. inversion results would be appropriate within the source-receiver plane but would not necessarily apply to propagation paths that travel up-slope.

This hypothesis is supported by piston core samples collected by researchers at the University of Miami in April 2000 [37]. The cores were collected at several locations near the positions of the source and receiver from the propagation loss experiment. The core sites are numbered and indicated with red circles in Figure 5.9. A row of cores aligned approximately parallel to the source-receiver plane lies along the 30 m isobath, roughly 2 km inshore of the source and receiver (specifically, consider cores 1,4,7,10,13, and 16). These will be referred to as the 'near-shore cores'. Another row of cores, to be referred to as the 'in-plane cores', sits very slightly offshore from the source-receiver plane approximately along the 170 m isobath (cores 2, 5, 8, 11, 14 and 17).

The sediment descriptions provided here follow the modified Dunham classification as used in the core data report. Refer to Appendix B for details on the classifica-

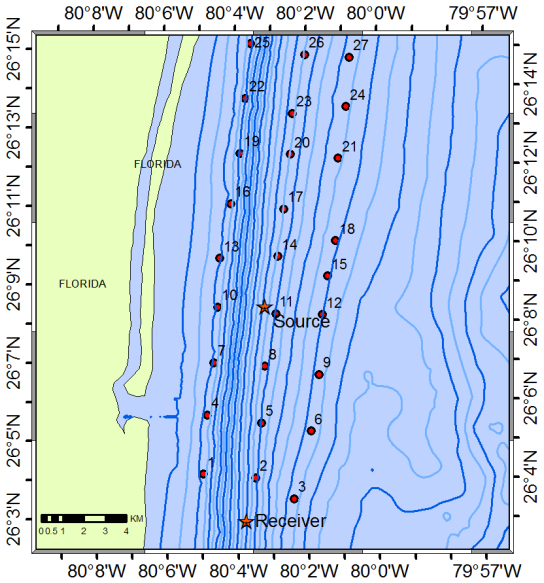

Figure 5.9: University of Miami piston core locations.

tion and for more information about the cores. Generally, the near-shore cores were consistently characterized by a thin ($\leq$ 10 cm) mud layer then approximately 10-30 cm of Grainstone overlying Rudstone and/or Floatstone. In contrast, the in-plane cores were all noted to consist of a thin mud layer overtop of varying thicknesses of Grainstone and/or Packstone but did not contain the coarse Rudstone/Floatstone layers. The data report showed mean compressional sound speed values of 2200 m/s for Rudstone and Floatstone, 1770 m/s for Grainstone and 1800 m/s for Packstone. Therefore the two regimes (near-shore and in-plane) are distinguishable by grain size and by compressional sound speed value, with the near-shore cores consisting of coarser, faster sediment.

With this experimental evidence to support the idea of shoreward range-dependence of the seafloor properties, Model case D was defined with the environment divided into three geoacoustic provinces as shown in the map in Figure 5.10. Each province consists of a single layer, that is, the limestone layer from model case C is not included in this case. The parameter values for each province are listed in Table 5.6. Each province also contains the artificial absorbing layer between 650 and 1000 m defined above. The province boundaries were selected to demarcate the stepped slope of the seafloor. 'Province 1' corresponds with the shallow-slope bathymetry segment from Section 5.1.2; it contains the source-receiver plane and consists of the 'base case'

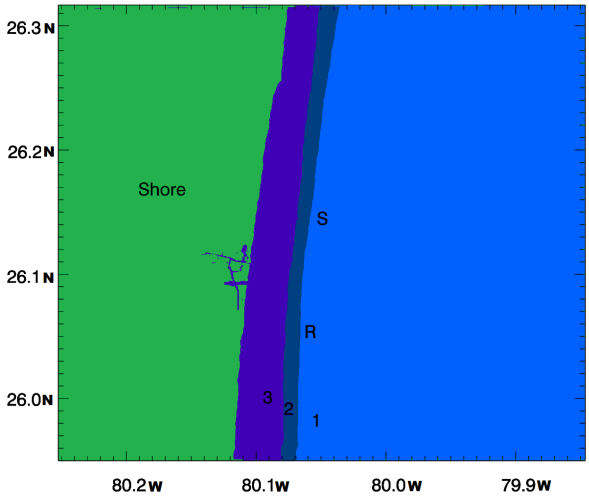

Figure 5.10: Geoacoustic provinces used for the range-dependent model Case D.

model parameters. 'Province 2' contains the steep segment of the slope where it is assumed that the sediment type is coarser. To represent coarser sediment, parameter values have been chosen that are appropriate for sediment with decreased porosity and increased grain size compared to the base case. With a decrease of porosity (or increase of grain size) there is a corresponding increase of the compressional-wave velocity ratio that relates the sediment sound speed to the pore water sound speed. The sound speed, density and attenuation have all been increased to values that are reasonable for a sound speed ratio of 1.19 and a porosity of 35% according to the regressions provided in Chapter 5 of Jackson and Richardson [31]. Shear parameters have also been introduced. This profile is consistent with a sediment description in between the types found in the near-shore and in-plane piston cores. Finally 'Province 3' lies at the top of the steep slope and is an extreme case defined to be representative of sediment with very low porosity, with compressional sound speed and density values consistent with the values from the near-shore piston core samples.

The mode propagation angles steepen with the increase of sound speed across geoacoustic provinces. This means that the ray paths shown in Section 5.1.2 above do not apply for the paths that travel through the steep-slope segment under the Province 2 parametrization. The propagation angles for the modes in the local environment

Table 5.6: Geoacoustic parameters used in the three-province model Case D.

Province	ρ (g/cm^3)	c_p (m/s)	α_p (dB/λ)	c_s (m/s)	α_s (dB/λ)
1	1.779	1676.0	0.05	0.0	0
2	1.9	1820.0	0.4	350.0	5.0
3	2.1	1950.0	0.8	490.0	6.5

at the Province 2 boundary were computed using Kraken and an updated ray path diagram is shown in Figure 5.11. It is noted that the horizontal ray paths in Province 2 experience greater refraction compared to the steep-sloped paths with the range-independent base case parametrization. The out-of-plane interference at 10 km for mode 7 is now attributed only to (black) paths from the shallow-slope segment (i.e. Province 1). This receiver range is in the shadow zone of the steep-slope (Province 2) paths. The refracted contribution of mode 7 at 10 km can therefore be expected to be weaker for this model case.

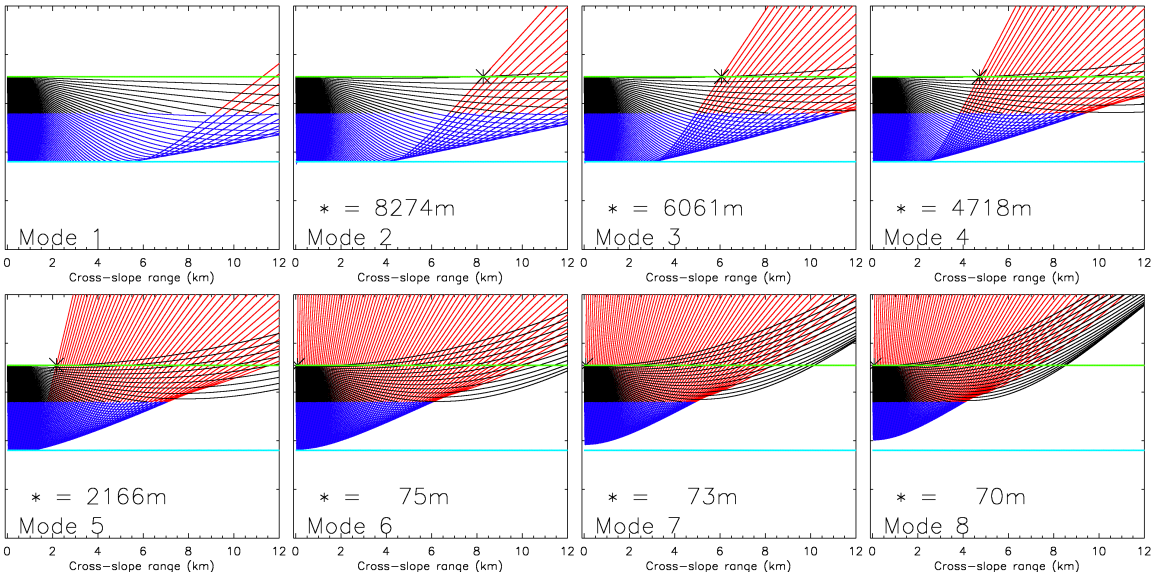

Figure 5.11: Horizontal propagation paths for each mode in the range-dependent Florida Strait test environment for paths travelling up-slope from the source-receiver plane (dark green line) and turning at the top of the steepest part of the shoreward slope (light blue-green line).

5.2 Approach

The goal for this modelling study is to characterize the out-of-plane propagation paths in the Florida Strait environment and to assess the strength of the 3D effect under different environment parameterizations. This is not an inversion study but an investigation into how these paths are influenced by the seafloor parameters that were weakly constrained in the Jiang et al. inversion [33]. The five geoacoustic models described in Section 5.1.3 were considered, they are as follows:

- Base Case: Current best knowledge of the geoacoustic environment with parameters taken from the studies of Jiang et al. [33] and Sturm et al. [46].
- Case A: Modification of base case parameters to include increased compressional attenuation.
- Case B: Modification of base case parameters to include shear parameters.
- Case C: Modification of base case parameters to include a deep limestone layer (excluding shear).
- Case D: Range-dependent geoacoustic model with sediment becoming coarser toward shore.

5.2.1 Model Configuration

MONM3D was configured to compute 3D calculations using the Fourier azimuthal operator with an initial radial count of 256. A 100 Hz omni-directional point source was placed at a depth of 107 m at location 26°8.29N, 80°3.20W (the source position from the 1999 deFerrari measurements [38]) where the water depth is 155 m. The model grid spacings are defined to be 10 m in range and 0.5 m in depth and the maximum arc-length separation (Δs_{max}) between radials is set to 12 m, a value determined through convergence testing to be appropriate for the ranges considered in this problem (see Section A.1). Using this value for Δs_{max}, there are 8192 radial paths at a range of 10 km.

5.2.2 Presentation of Results

Single frequency results at 100 Hz for each model case will be presented using plots of transmission loss as a function of range and depth and with mode spectrum plots.

Broadband results will be presented as waveform traces, and vertical beam patterns generated as described in Section 3.3. The source function used to generate the waveform traces is a Gaussian cosine pulse centered at f_c = 100 Hz. The source pulse, shown in Figure 5.12, has a 50 Hz bandwidth and is defined by the function $S(t) = \cos(2\pi f_c t)\exp[-(\sigma\pi t)^2]$ where $\sigma = 12$. This is the same function that was used in the Sturm analysis [46]. The spectrum of the M-sequence used for the experimental source is a sinc function [5] with nulls spaced at $1/T_d = 1/0.04$s= 25 Hz, thus the main lobe has the same bandwidth as the source function used in the simulation.

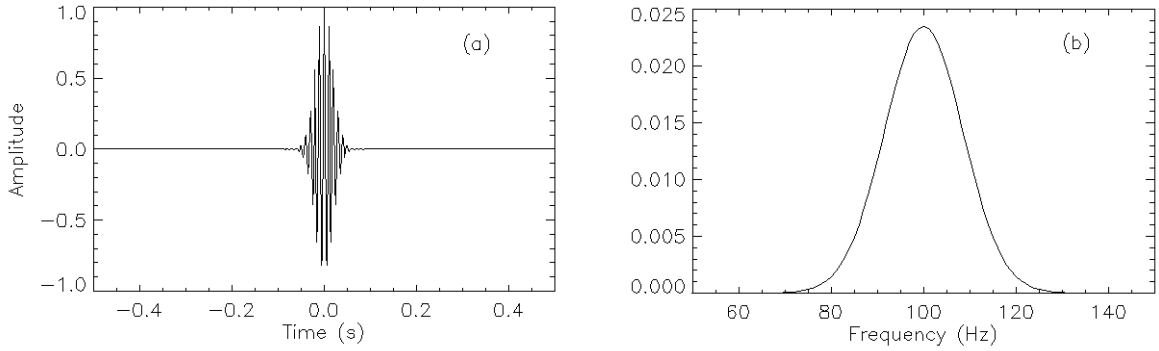

Figure 5.12: Time domain source function (a) and the real part of its spectrum (b) used for Fourier synthesis.

5.3 Results

5.3.1 Base Case Geoacoustics

MONM3D output for the base case geoacoustic model contains the expected presence of 3D propagation effects and these effects will be explored in this section. A plot of TL versus range in the cross-slope direction (i.e. in the source-receiver plane) at 100 Hz is shown in Figure 5.13 for a single receiver depth of 54 m (the depth of one of the receiving hydrophones in the deFerrari experiment). In this figure the black curve shows the results based on a 2D model calculation and the blue curve shows the full 3D model result, both using the base case geoacoustic parametrization.

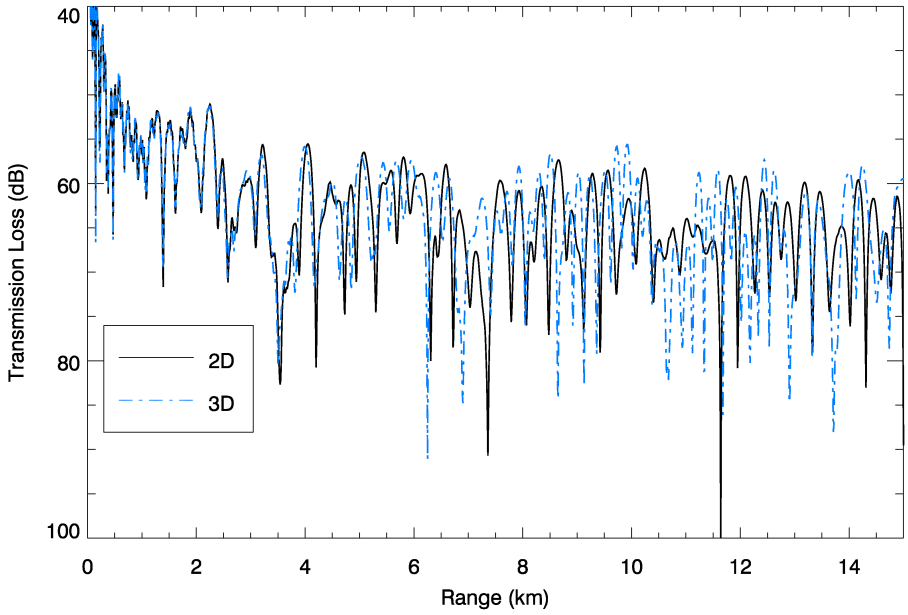

Figure 5.13: 100 Hz TL as a function of range at 54 m depth for the Florida Strait test case from 2D calculations (black curve) and 3D calculations (blue curve) for the base case geoacoustic model

The curves are very similar at ranges less than approximately 3 km, indicating that out-of-plane propagation paths do not influence the field at close ranges in the source-receiver plane. The curves begin to exhibit differences beyond 3 km and are very dissimilar at ranges of 9 km and greater. At these ranges there are regions where the 3D TL curve contains a more rapidly varying interference structure. These

differences are expected to be due to the interference of out-of-plane arrivals which are not accounted for in the 2D result. This is now investigated.

Consider the horizontal ray path diagram in Figure 5.5 from Section 5.1.2. The ray paths indicate that modes 6, 7 and 8 couple into the source-receiver plane at ranges less than 3 km. However, at these ranges the path lengths for the refracted arrivals is much greater than those for the 'direct paths' so the refracted paths experience greater propagation loss. Based on the TL curves, these paths do not appear to contribute significantly to the 3D field. As the range increases the path-length differences between the refracted and direct paths shorten and these refracted modes provide a more important contribution to the field. Additionally, beyond 3 km range modes 5, 4, 3, and 2 refract progressively into the source-receiver plane and strengthen the 3D effect with increasing range. Beyond 9 km range the source-receiver plane is exposed to interference from all modes greater than 1 and the 3D effect is most strongly observed at these longer ranges.

A plot showing TL versus cross-slope range at all depths is presented for 2D model results in Figure 5.14 and for full 3D calculations in Figure 5.15. The range-depth TL plot for the 2D calculation shows progressive propagation loss with range since the sound attenuates with each interaction with the sandy seafloor. In contrast, the 3D interference pattern contains more variable structure. A plot showing the difference between the 2D and the 3D fields in decibels is shown in Figure 5.16. At some depths, very small differences of a couple of dB are noted at ranges less than 3 km. These differences can be attributed to refracted arrivals of modes 6, 7, and 8 that are expected from the horizontal ray path diagram, as explained above. The 3D effect is most notable at ranges greater than approximately 5 km in this plot. The field differences could be attributed to the presence of refracted arrivals that are not present in the 2D result.

To better understand the behaviour of the individual modes in this environment, the PE field was decomposed into its modal components using the approach described in Section 3.3.1. The modal composition of the PE field was extracted at every kilometre along a track in the source-receiver plane and the resulting wavenumber spectra are shown in Figures 5.17 and 5.18 for 2D and for 3D model results respectively. These plots present the magnitude of the modes as a function of wavenumber and range in the source-receiver plane. Mode 1 has the largest wavenumber and is at the top of the plot in the lower panel. The top panel of each figure shows the local water depth corresponding to the range at which each spectrum was computed. The results from

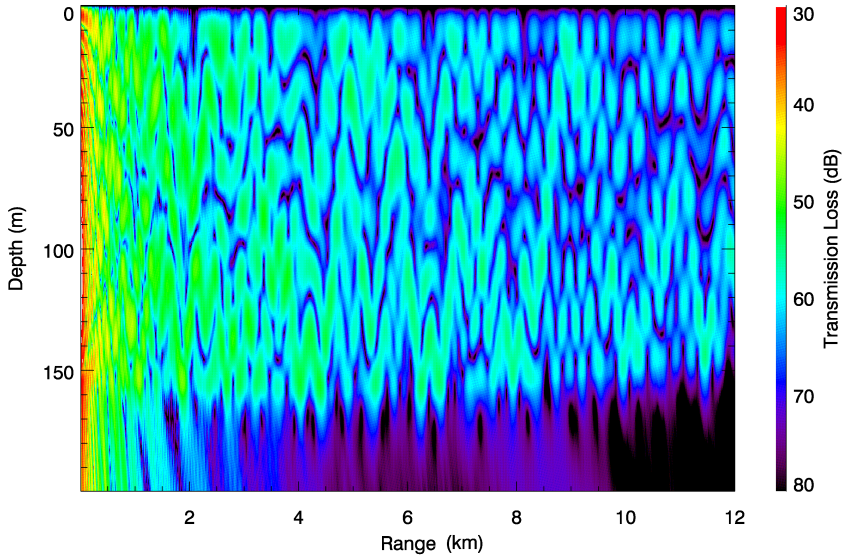

Figure 5.14: Transmission loss as a function of range and depth, computed using 2D calculations with the base case geoacoustic model.

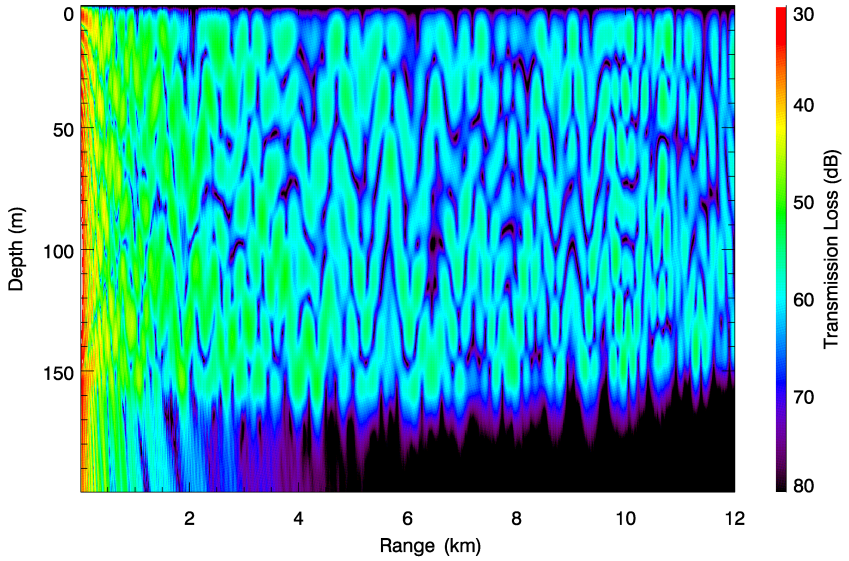

Figure 5.15: Transmission loss as a function of range and depth, computed using full 3D calculations with the base case geoacoustic model.

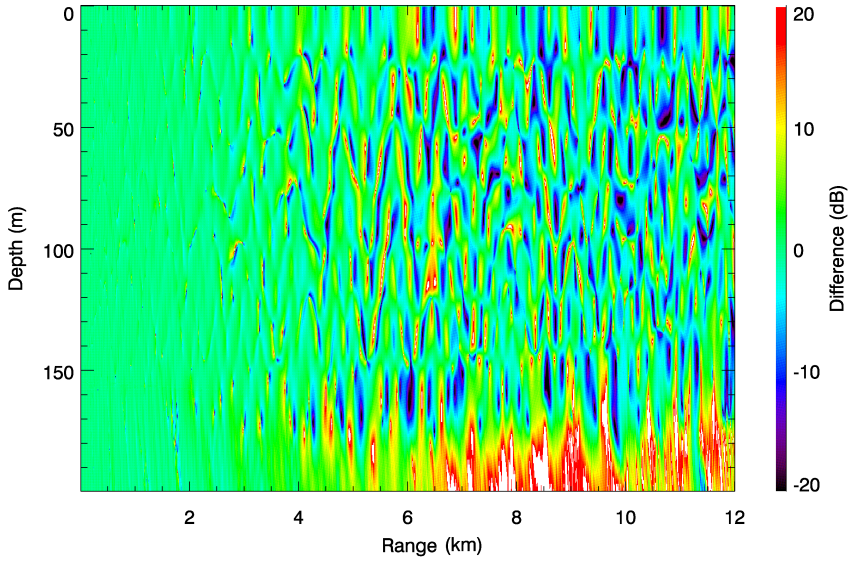

Figure 5.16: Difference between the field obtained from 3D calculations and that from 2D calculations (2D-3D), for the base model case.

both the 2D and the 3D calculations produce mode wave numbers that depend weakly on range due to the small bathymetry changes that occur between the source and the receiver. It is noted that modes 5, 8, 9, and 10 are weakly excited and contribute minimally to the field at 10 km range.

The 2D and 3D mode spectra look very similar at close ranges, but begin to illustrate noticeable differences at approximately 6 km range. Whereas the magnitude of individual modes in the spectra from the 2D calculations gradually decrease with range, the spectra from the 3D calculations show many modes with increased amplitude at range due to the interference of the different horizontally refracted arrival paths. This effect is observed to progress through the modes with increasing range; that is, the higher-order modes demonstrate this interference at shorter ranges than the lower-order modes. This is because the higher-order modes are more strongly refracted by the sloping seafloor and the refracted paths are introduced into the source-receiver plane at shorter ranges than those for the low order modes. This has been discussed above and shown in the horizontal ray path diagram. Also, since horizontal refraction toward the down-slope direction causes the modes to turn out of the source-receiver plane there is a spatial envelope for each mode in the 3D results beyond which the mode amplitudes die off. Again, this effect is noted at shorter

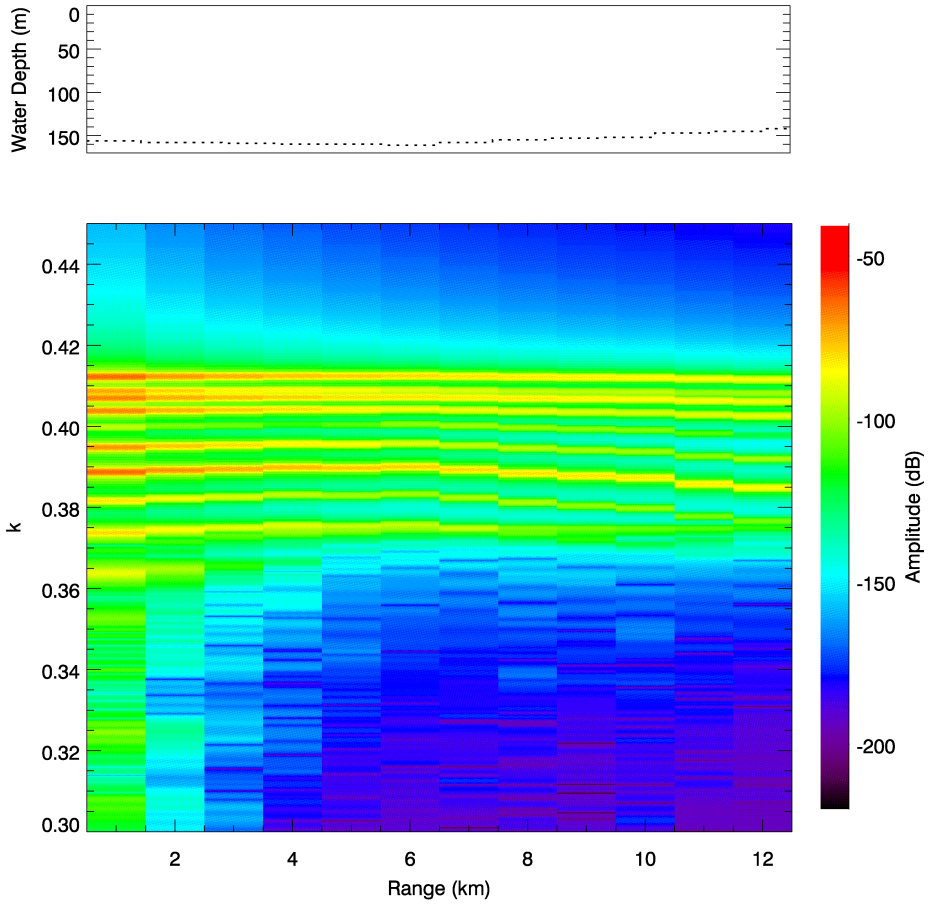

Figure 5.17: Wavenumber spectra as a function of range in the source-receiver plane from PE fields computed using 2D calculations, base model case.

ranges for higher order modes.

The 3D wavenumber spectra indicate that mode 7 ($k \approx 0.388$ m^{-1}) provides the strongest contribution to the 3D field at the 10 km receiving array range. The contribution of mode 6 ($k \approx 0.394$ m^{-1}) is also very strong at this range. This differs from the mode composition based on the 2D calculations which shows only a weak contribution from mode 7 and a minimal contribution from mode 6 at this range. Again this indicates a contribution from horizontally refracted arrivals that couple into the source-receiver plane but are not accounted for in the 2D model. This is consistent with the hypothesis of Sturm et al. that the secondary arrivals in the experimental data were dominantly composed of modes 6 and 7 [46]. At ranges beyond 10 km, modes 6 and higher experience a more rapid amplitude decay in the

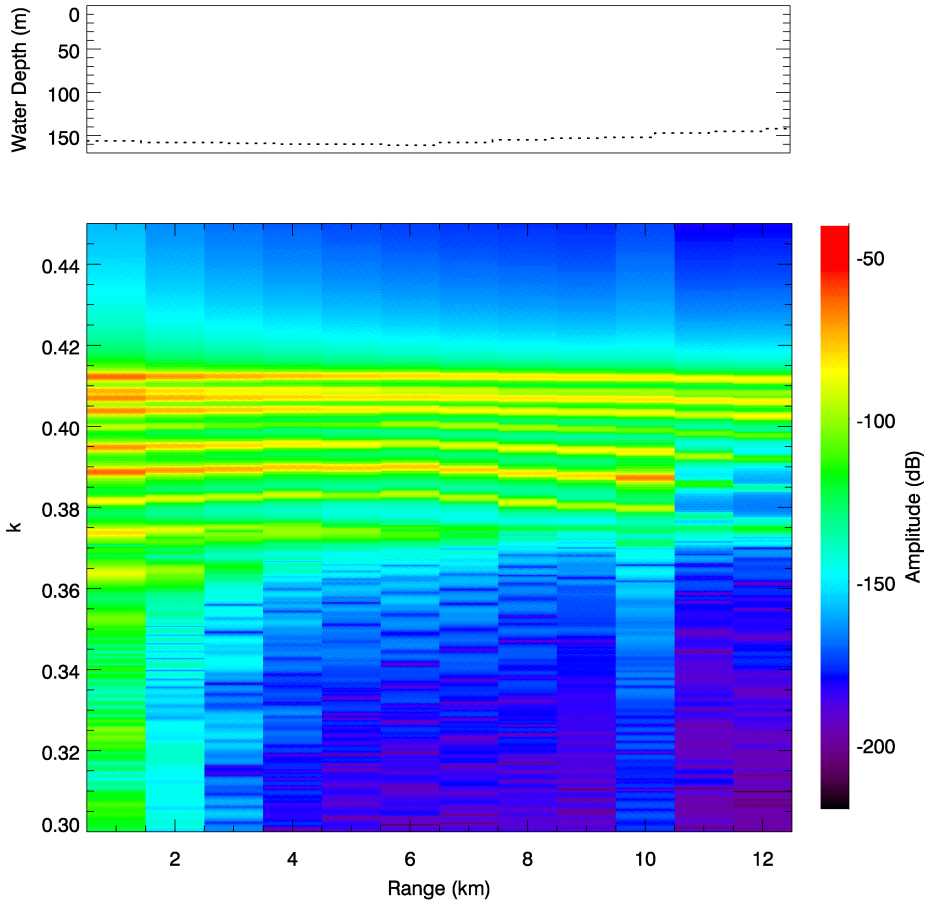

Figure 5.18: Wavenumber spectra as a function of range in the source-receiver plane from PE fields computed using 3D calculations, base model case.

3D case compared to the 2D case as the modes turn out of the source-receiver plane. Again, this behaviour is predicted in the ray path diagram.

The modelled sound fields for this non-idealized environment are not easily interpreted due to the complexities of the properties of the study environment. Specifically, the structure of the water column sound speed profile and the non-uniformly sloping bathymetry complicate an intuitive understanding of the behaviour of the individual modes. The mode shapes and amplitudes are altered as they travel through different environmental regimes and are particularly influenced by the shoaling water depth and the truncation of the sound speed profile in shoreward directions. To examine the behaviour of the modes as they travel toward shore, wave-number spectra were also extracted every 500 m in the up-slope direction (perpendicular to the source-receiver

plane). A plot of the spectra thus obtained from the 3D PE calculation is shown in Figure 5.19. Here the local water depth as well as the local shape of the sound speed profile are plotted in the top two panels of the figure.

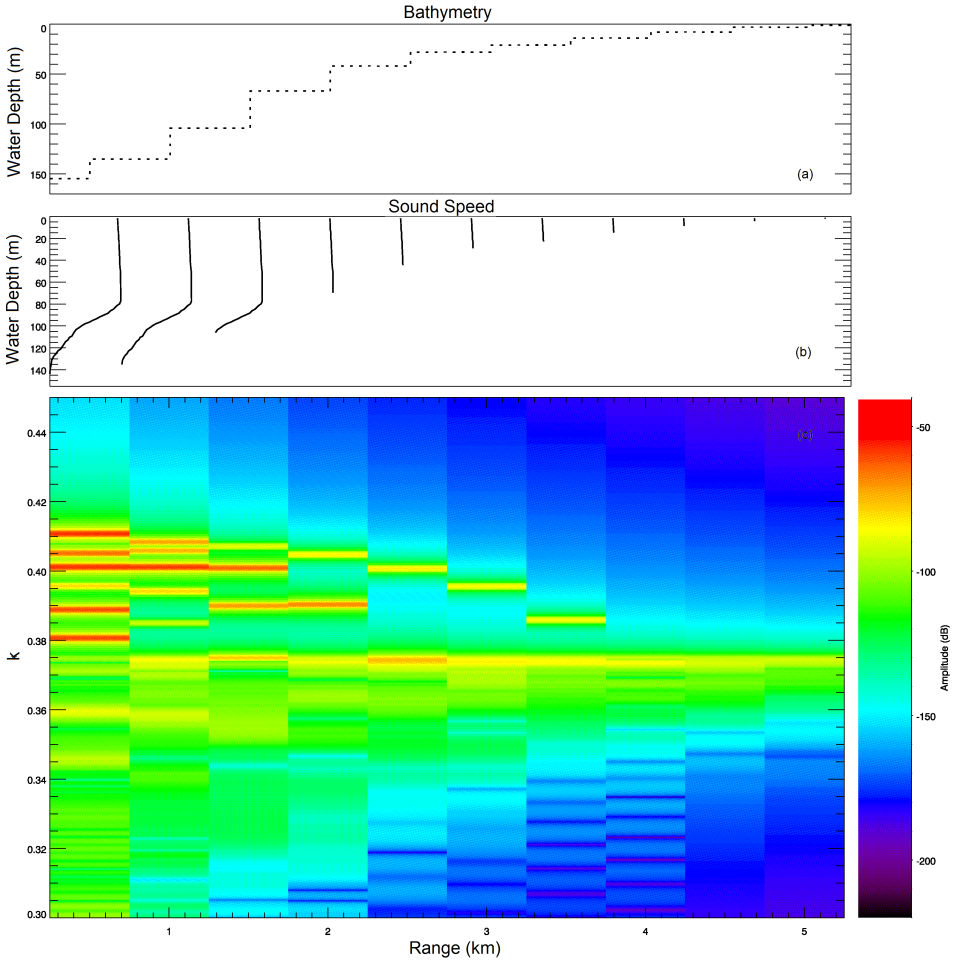

Figure 5.19: Local bathymetry (a), truncated sound speed profile (b) and wavenumber spectra (c) as a function of range in the up-slope plane from PE fields computed using 3D calculations, base model case.

Of note in this figure is the shift of the wavenumbers to lower values (steeper propagation angles) as the modes travel up-slope and compress to fit into the shallower waveguide. The higher-order mode amplitudes are strongly attenuated at up-slope ranges where the mode propagation angles increase beyond the critical angle for the sediment material. Thus, each mode has a maximum up-slope range to which it can travel, dictated by the local bathymetry, though a mode travelling obliquely up-slope may be horizontally refracted before reaching the cutoff depth where its propagation

angle exceeds the critical angle. These are the paths that continue down-slope and are observed to interfere in the cross-slope plane. Mode 7 ($k_7 = 0.388043$ m^{-1} at the source) appears to persist to approximately 2 km range in the up-slope direction, so mode 7 paths that couple into the source-receiver plane have not travelled more than approximately 2 km up-slope.

Also of note in this spectrum plot is evidence of mode coupling at ranges where the number of peaks decreases with increasing up-slope range. For example, at 1 km range there are seven peaks in the spectrum for k values between 0.42 and 0.35 m^{-1}. At 1.5 km range there are only four peaks in the spectrum, some of which have an increased amplitude compared to the value at 1 km. It appears that mode 2 has coupled into mode 3, mode 3 has coupled to mode 4 and so on.

The wavenumbers and mode shapes also change as they travel up-slope due to the varying structure of the sound speed profile. As the water depth decreases the influence of the downward-refracting portion of the sound speed profile is reduced. Since the downward-refracting profile only traps Mode 1 at the source-receiver plane, the influence of the changing sound speed profile is assumed to be secondary in its influence on the mode behaviour compared to the effect of the shoaling bathymetry.

Thus far it has been shown that there is a 3D effect in the environment and that modes 6 and 7 contribute dominantly to the 3D effect at 10 km range. It is evident from the horizontal ray path diagram that the refracted arrival path lengths, and hence the arrival times for the refracted paths, will vary as a function of source-receiver range and will be different for each mode at a given receiver range. The PE field results do not contain information pertaining to the arrival times of the refracted mode paths since there is no time-domain information contained in these single frequency PE calculations. Therefore MONM3D calculations were computed for a band of frequencies between 75 and 125 Hz (at 1 Hz resolution) such that waveform traces could be simulated through Fourier synthesis (ref Section 3.3.2). The resulting waveforms for signals at 10 km range are shown in Figure 5.20 for both 2D and 3D calculations. In these plots, the envelope of the measured data is over-plotted with a red curve that was generated by digitizing the waveforms presented in Sturm et al. [46] which, in turn, were derived from the deFerrari data. Each trace is normalized to the maximum level for that depth. There are thirteen traces shown, corresponding to the hydrophone depths for which high sensitivity measured data were available. Recall that these receiver depths are not evenly spaced in the water column; the depths of the 13 receivers were listed in Table 5.1. At the top of waveform

plots are mode numbers, placed at the expected arrival time for the 'direct-path' (or 'in-plane') arrivals of the corresponding modes. These are aligned according to the relative time delay expected between modes based on the group velocities computed by Kraken at a frequency of 100 Hz.

The waveforms from the full-3D MONM3D results do contain large amplitude 'second arrivals' that appear at approximately 7.1 seconds in the 3D waveform plot and arrive after the expected direct-path arrivals. These secondary arrivals are not observed in the results from the 2D calculations. However, as was found in the Sturm results [46], the modelled second arrivals experience a greater time delay compared to the measured arrivals.

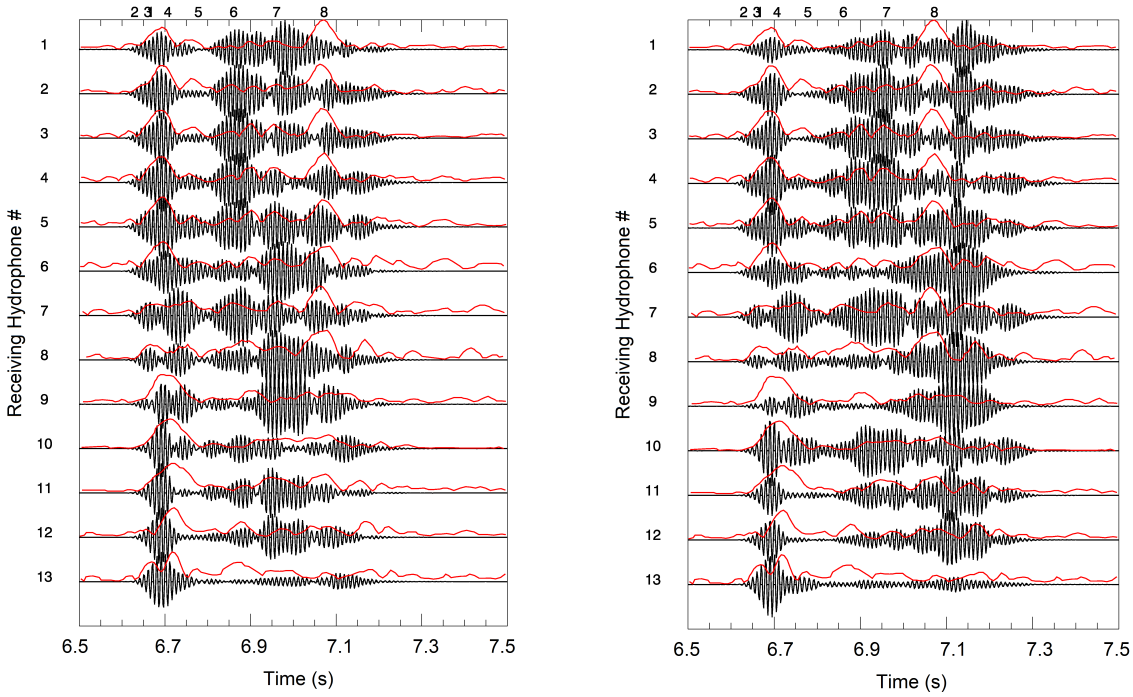

Figure 5.20: Simulated waveforms obtained through Fourier synthesis of PE fields computed using (left) 2D calculations and (right) 3D calculations, base model case. Red curves present the envelope of the measured data from the deFerrari experiment.

Vertical beamforming was applied to investigate the vertical arrival structure of the modelled waveforms which gives an indication of the mode arrival times. The vertical beam patterns are shown in Figure 5.21 for both 2D and 3D calculations. The 2D and 3D results look very similar in the early part of the signal (at times <6.9 s) and both indicate that the first arrivals are composed of low-angle vertical beams <12°, that is, low order modes. Since the 2D and 3D results agree for the

early part of the signal, this part of the waveform must be composed of propagation paths that travel dominantly in the source-receiver plane.

In both cases the beam angle increases with arrival time since the waveform is composed of the time-delayed arrivals of individual modes that travel at different group velocities. Higher-order modes have higher beam angles and travel at slower group velocities. For times >6.9 s the 2D and 3D beam patterns differ since the 3D signal also contains contributions from out-of-plane modes that have coupled into the source-receiver plane. These arrivals are delayed from the first arrivals since they have travelled longer propagation paths. The strong second arrivals are denoted by the bright spot in the 3D beam pattern at around 7.1 s that is dominated by arrival angles between 15-20°, corresponding to the propagation angles for modes 6 and 7. These second arrivals dominate the beam pattern in this case. Finally, it is noted that the 2D beam pattern contains low amplitude in-plane arrivals that appear at times just beyond 7.1 s with vertical beam angles >20°; that is, modes higher than mode 7. From the 3D spectra plot in Figure 5.18, and from the horizontal ray diagram, it was noted that such modes begin to turn out of the source-receiver plane at ranges shorter than 10 km, therefore these arrivals are much weaker in the 3D beam pattern.

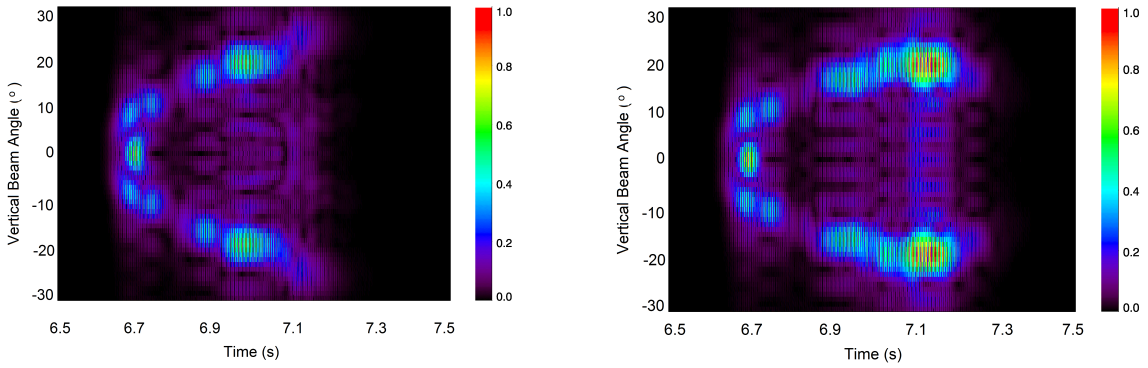

Figure 5.21: Vertical directionality of the modelled waveform from (left) 2D calculations and (right) 3D calculations, base model case.

5.3.2 Model Case A: High compressional attenuation

MONM3D was run with the model case A parametrization to investigate the effect of increasing the compressional attenuation in the seafloor. Figure 5.22 shows TL as a function of range at 54 m depth computed for this model case with full 3D calculations; the plot also shows TL for the base case as a comparison. The two curves are very similar in the first 2-3 km range, beyond which there is generally increased TL for model case A due to the increased attenuation in the seafloor. The TL curves also differ in their structure at longer ranges in that the curve for case A has lower amplitude oscillations indicative of weaker modal interference.

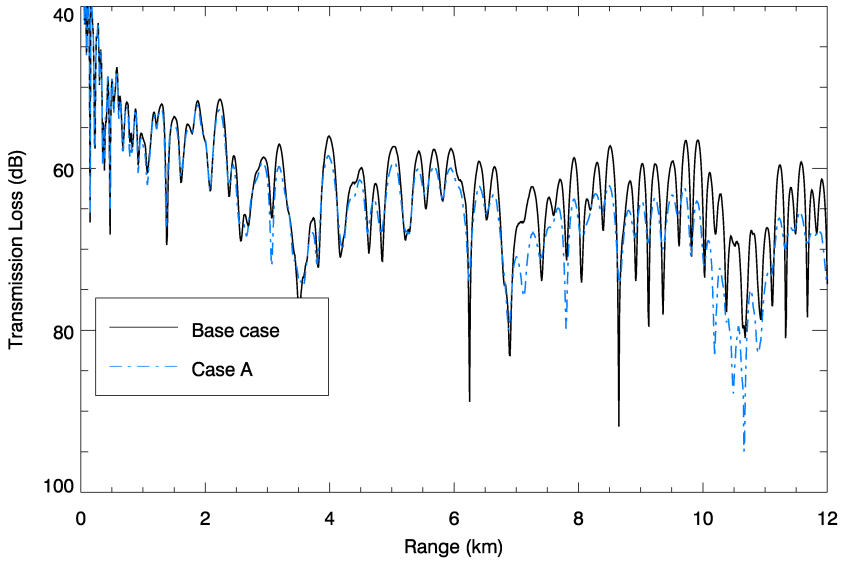

Figure 5.22: Transmission loss as a function of range at 54 m depth, computed using 3D calculations with geoacoustic model case A (blue) and for the base case (black).

Figure 5.23 presents a plot of the 3D TL as a function of cross-slope range and depth for case A. This figure also exhibits increased long-range TL compared to the base case (Figure 5.15) and there is less structure in the interference pattern at long ranges compared to what was observed for the base model case. Figure 5.24 shows the dB difference of the field for model case A subtracted from base case field which shows that the fields are similar at close ranges but differ in structure and amplitude at longer ranges. The greatest differences are observed mostly at ranges beyond 9 km. There are two factors that contribute to the differences in the interference

patterns. The first is that the increased attenuation reduces the individual mode amplitudes and changes their relative contributions as a function of range. Recall from the reflection coefficient plot in Figure 5.6 that the higher-order modes are more strongly attenuated than the lower-order modes. Secondly, the 3D effect is reduced in model case A since the out-of-plane paths have experienced greater loss in this case and provide a weaker contribution to the field compared to the base case.

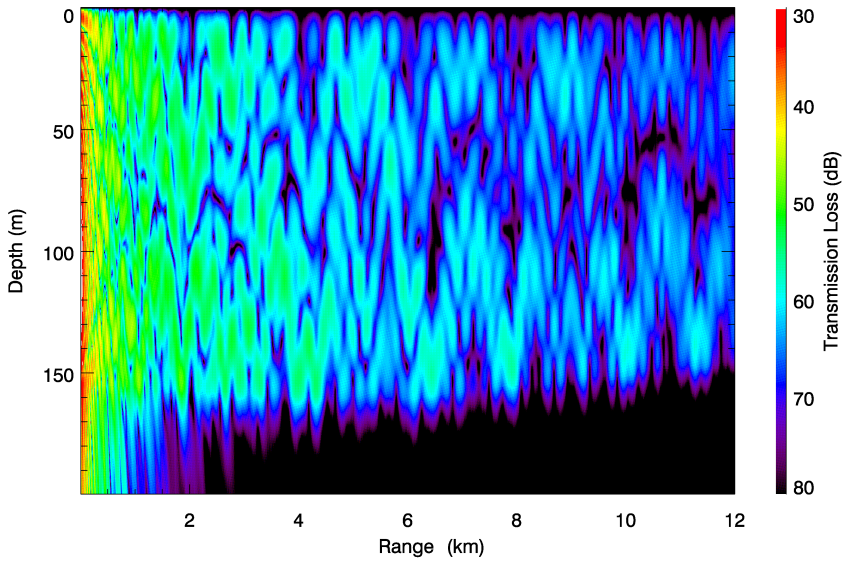

Figure 5.23: Transmission loss as a function of range and depth, computed using 3D calculations with geoacoustic model case A.

Modal decomposition of the full 3D field for this model case reveals the effect that the increased attenuation has on the behaviour of individual modes. The wavenumber spectra versus range for this model case, shown in Figure 5.25, show a decrease of the model amplitudes when compared to those shown previously for the base case in Figure 5.18. This plot does not show the strengthening of the mode amplitudes that was observed in the 3D base case mode spectra as the out-of-plane paths were introduced into the source-receiver plane. Horizontal refraction of the propagation paths does occur in the model case A environment, evidenced by the fact that the high order mode amplitudes are still noted to cutoff sharply with range as they turn out of the plane. But, since the longer up-slope paths interact more frequently with the seafloor compared to the direct paths, they are more strongly attenuated. These paths contribute much less energy to the field in the source-receiver plane and the

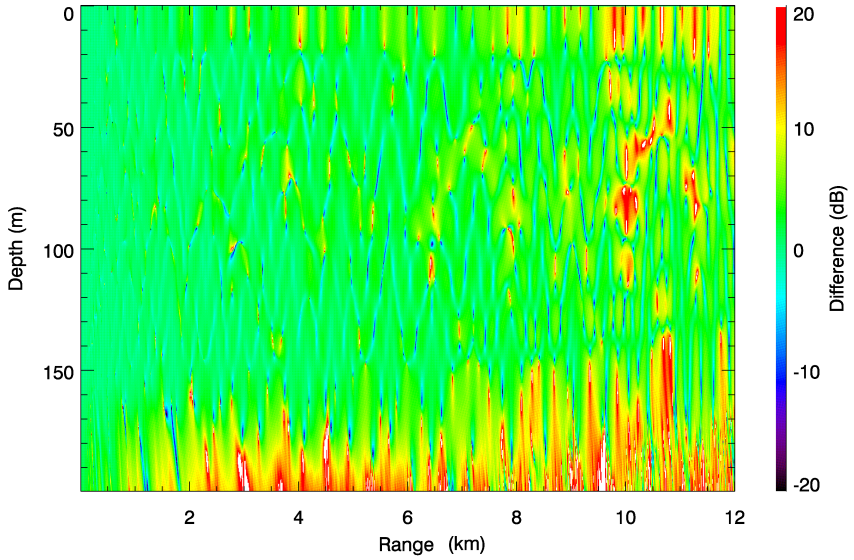

Figure 5.24: Difference between the field for geoacoustic model case A and that for the base model case.

strength of the 3D effect is reduced. In this case, the contribution of modes 6 and 7 at 10 km is weaker than the more dominant contributions from the lower-order modes.

Comparing Figure 5.25 with Figure 5.18 it is also noted that with increased compressional attenuation the higher-order mode amplitudes are more strongly affected than the low-order modes. Again, this can be explained by considering the effect that compressional attenuation has on the reflection coefficient (see Figure 5.6 in Section 5.1.3) noting that the higher order modes are more strongly attenuated. Modes 6 and 7 have propagation angles of 17° and 20° which correspond to reflection coefficient values of 0.93 and 0.92, respectively, for case A. The reflection coefficient has a value 0.99 for these angles in the base model case. This difference, from the increase of the compressional attenuation, results in the reduced 3D influence of modes 6 and 7 in the calculations for model case A.

Again, 3D fields for all frequencies from 75 to 125 Hz were computed for this model case in order to simulate the signals received at 10 km range. The resulting waveforms are shown on the right side in Figure 5.26, where the base case result is shown on the left for comparison. The strong second arrivals are not evident in the 3D result for this case, again due to the absence of the strong out-of-plane arrivals of modes 6 and 7. The time delayed vertical beam patterns for these waveforms

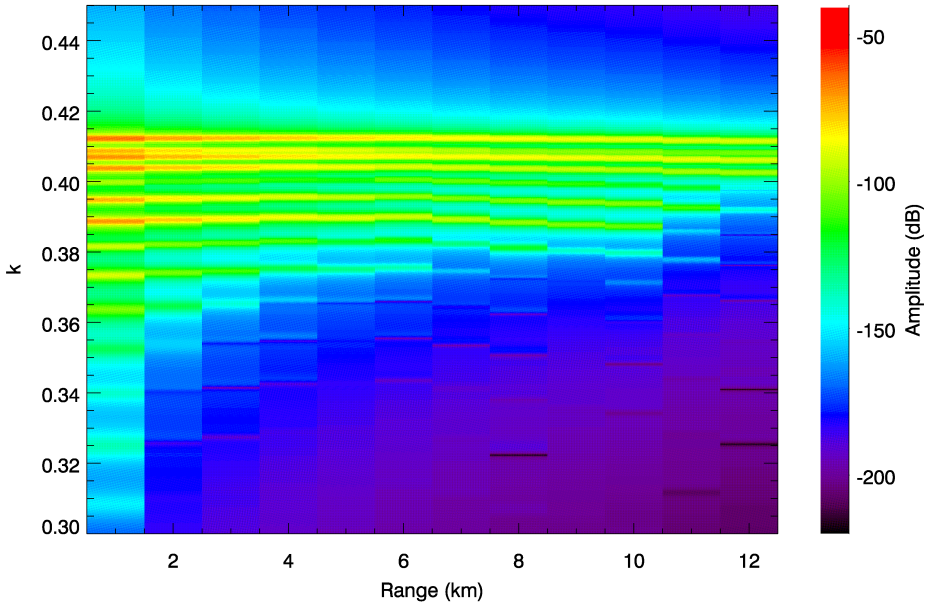

Figure 5.25: Wavenumber spectra as a function of range in the source-receiver plane from PE fields computed using 3D calculations, model case A.

are shown in Figure 5.27. In this case the structure looks the same as it did in the base case, but the amplitude of the later arrivals is greatly reduced and the primary arrivals of the low-order modes are dominant in the waveforms.

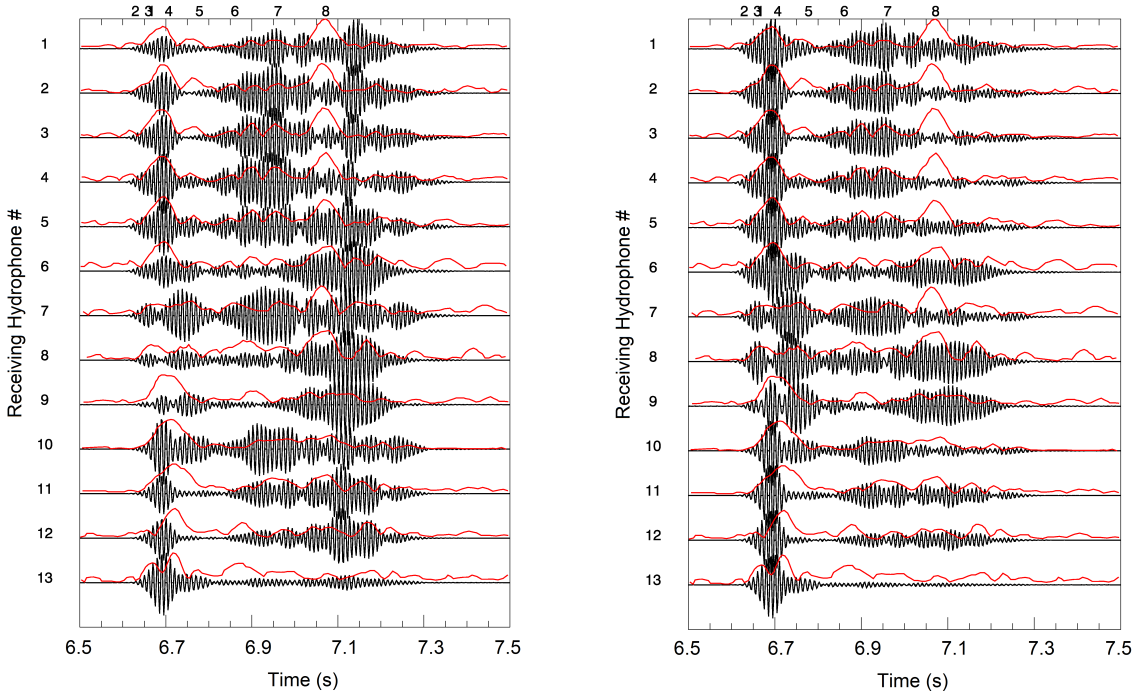

Figure 5.26: Simulated waveforms obtained through Fourier synthesis of PE fields computed using 3D calculations for the base model case (left) and for model case A (right). Red curves present the envelope of the measured data from the deFerrari experiment.

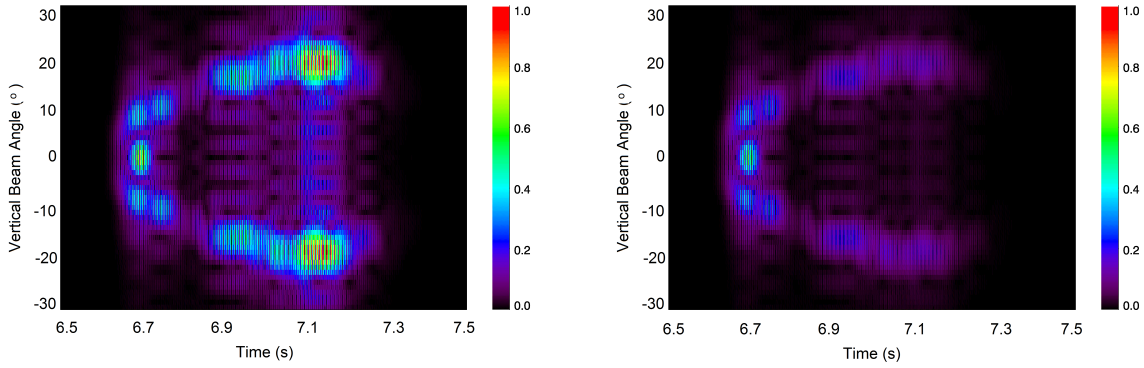

Figure 5.27: Vertical directionality of the modelled waveform from 3D calculations for (left) the base model case and (right) model case A.

5.3.3 Model Case B: Elastic sediment with shear

The model case B parametrization was applied in MONM3D to investigate the effect of including shear in the seafloor. Figure 5.29 contains a plot of TL versus range (from 3D calculations) at a depth of 54 m for this model case; for comparison, TL curves for the base case and for model case A are also shown. The curves for all the model cases are very similar to a range of approximately 2 km. Beyond 2 km the curve for model case B contains more structure from modal interference in comparison to that for case A, but the amplitude is reduced compared to the base case. This indicates that there is slightly increased transmission loss due to conversion to shear propagation, but that this effect is not as strong as the effect from the increased compressional attenuation in case A.

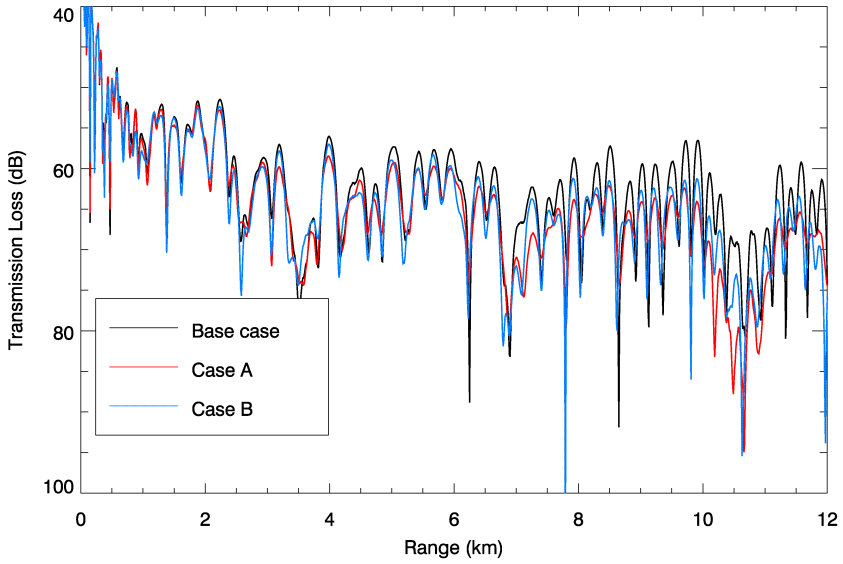

Figure 5.28: Transmission loss as a function of range at 54 m depth, computed using 3D calculations with geoacoustic model case B (blue), for the base case (black) and for case A (red).

Figure 5.29 presents TL as a function of cross-slope range at all depths for this model case, computed with full 3D calculations. The structure of the interference pattern in the cross-slope field for model case B more closely matches that of the base case field. The difference of the field for model case B subtracted from the base model case is shown in Figure 5.30. The greatest differences are again observed beyond

approximately 9 km range, but the magnitude of the differences are smaller than they were when comparing model case A with the base case. Again, this indicates that the effect of the shear parameters in case B is weaker than the effect of the increased compressional attenuation in case A. The structure of the field differs from the base case since the out-of-plane paths that couple into the source-receiver plane have been attenuated and their contributions to the field have been reduced.

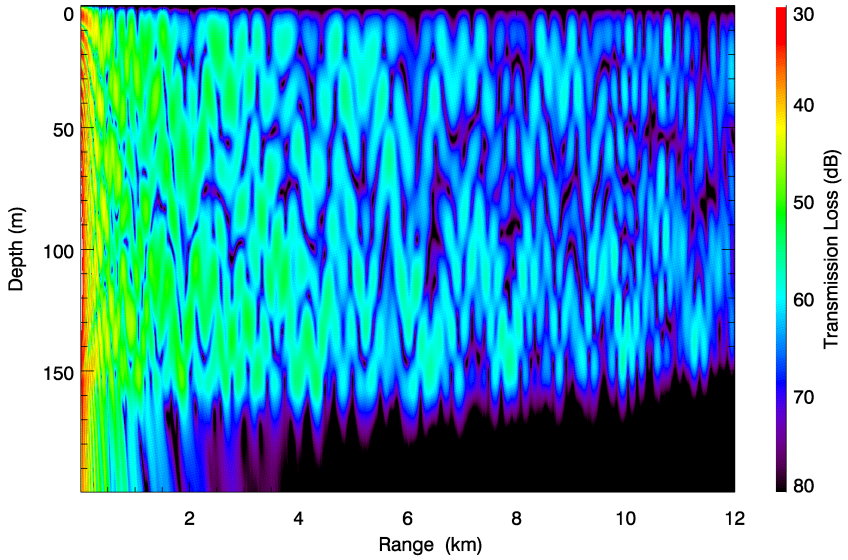

Figure 5.29: Transmission loss as a function of range and depth, computed using 3D calculations with geoacoustic model case B.

To investigate the structure of the cross-slope field for this model case, the full 3D field was again decomposed into its modal constituents. The resulting spectra are plotted in Figure 5.31. In this case, at 10 km range the amplitudes of modes 6 and 7 are greater than were observed in model case A, but lower than was observed for the base case. The contributions of modes 6 and 7 are comparable to those of the lower-order modes in this case. Considering the reflection coefficient for the geoacoustic model of case B, plotted in Figure 5.7, it is noted again that not all modes are equally affected by this parameter change. The case B reflection coefficients for modes 6 and 7 are 0.94 and 0.95, respectively, and these modes will experience less loss compared to model case A. It is also noted that the reflection coefficient for mode 7 is greater than that for mode 6; therefore, refracted mode 7 paths will contribute slightly more to the field than mode 6 paths.

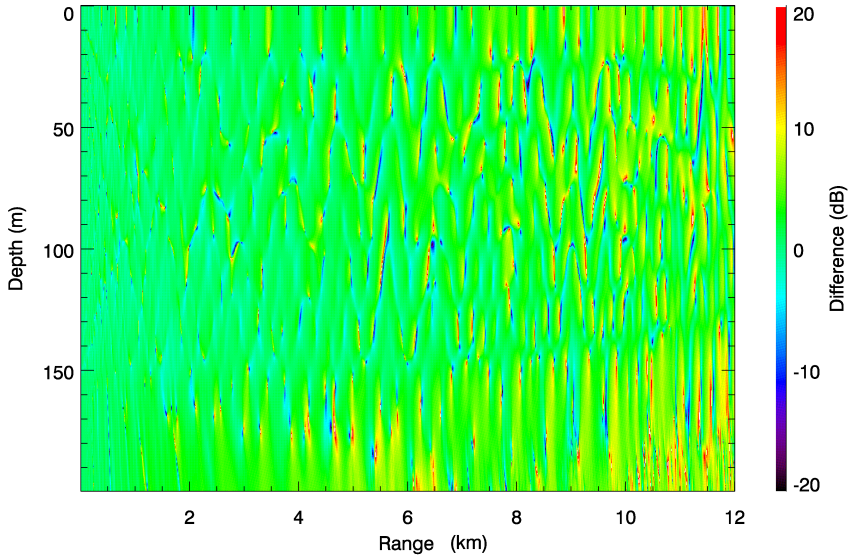

Figure 5.30: Difference between the field for geoacoustic model case B and that for the base model case.

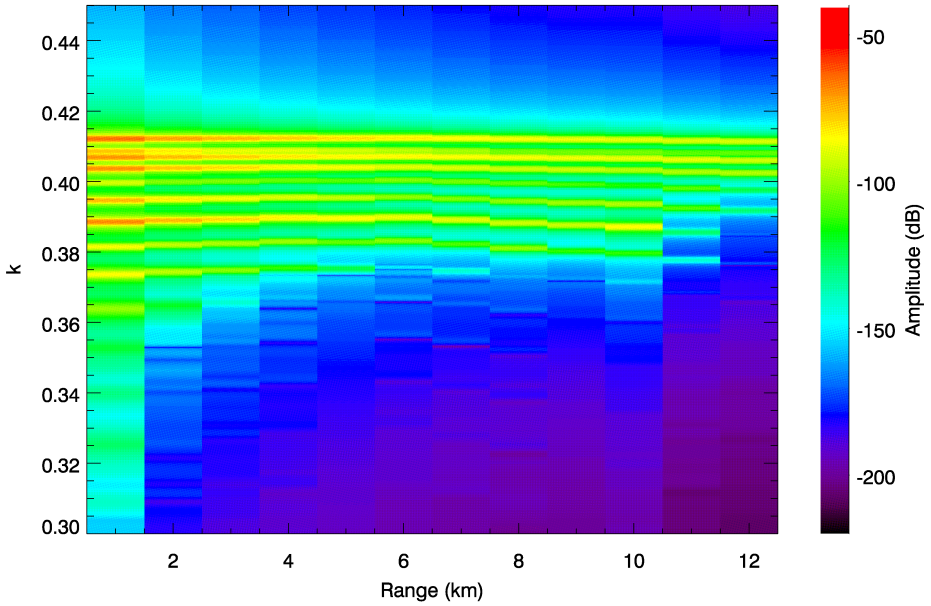

Figure 5.31: Wavenumber spectra as a function of range in the source-receiver plane from PE fields computed using 3D calculations, model case B.

The waveforms generated for this model case are plotted in Figure 5.32 along side the base model case waveforms as comparison. Since mode 6 and mode 7 are only weakly attenuated by the introduction of the shear parameters, the waveforms do contain strong secondary arrivals that follow the expected first arrival modes. However, it is noted that there is a mismatch in timing for the second arrivals compared to the measured data as there was in the base case. The vertical beam pattern for model case B is presented in the right-hand panel of Figure 5.33 (the base case pattern is on the left for comparison). Here the arrivals at 7.1 s are accentuated compared to case A but are diminished compared to the base case. Now the primary, low-angle arrivals and the later, higher-angle arrivals are comparable in magnitude. The second arrivals are again noted to occur at beam angles that correspond with the vertical propagation angles of modes 6 and 7.

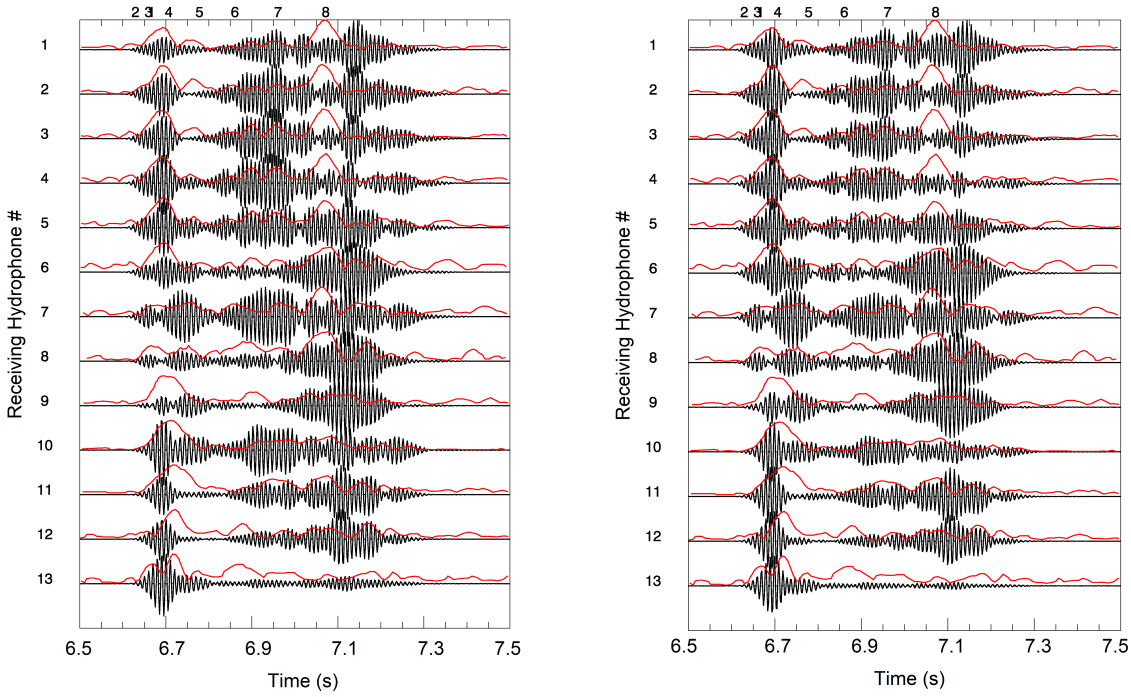

Figure 5.32: Simulated waveforms obtained through Fourier synthesis of PE fields computed using 3D calculations for the base model case (left) and for model case B (right). Red curves present the envelope of the measured data from the deFerrari experiment.

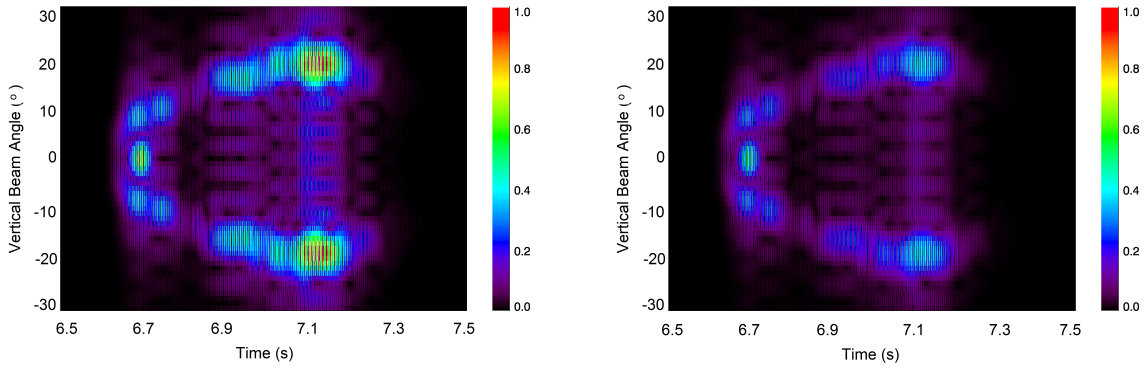

Figure 5.33: Vertical directionality of the modelled waveform from 3D calculations for (left) the base model case and (right) model case B.

5.3.4 Model Case C: Layered seafloor with limestone

The influence of deeper seafloor structure was investigated in model case C. TL versus range at 54 m depth is plotted in Figure 5.34 for this model case and for the base model case as comparison. These curves are very different in the first 8 km which is due to the increased number of modes that are supported in the model with the deep limestone layer. Beyond 8 km range the two curves are very similar. It is noted that the exclusion of shear in the limestone for this case limits the validity of the simulation for the modes greater than mode 8. Therefore the field at ranges less than 8 km in this model case is likely highly inaccurate. As previously discussed, modes greater than mode 8 have refracted out of the source-receiver plane at ranges greater than 8 km (modes refract out of the plane at shorter ranges as the mode number increases) and the field at ranges greater than 8 km should not be affected by the exclusion of shear in the limestone. As the higher-order modes exit the plane the transmission loss curve better matches that for the base model case in which those modes are not supported. A color plot of transmission loss versus range and depth is shown in Figure 5.35. Again this plot is very different from the base model case at close ranges and more similar to the base case at longer ranges. A plot of the difference between the fields is shown in Figure 5.36.

The wavenumber spectrum (for k values between 0.30 and 0.44 m^{-1}) obtained through modal decomposition of the field for this model case is shown in Figure 5.37. There is an increased number of peaks in this spectrum compared to the base case due to the increased number of supported modes in this case. The higher-order modes disappear with range as these modes refract out of the source-receiver plane. The part

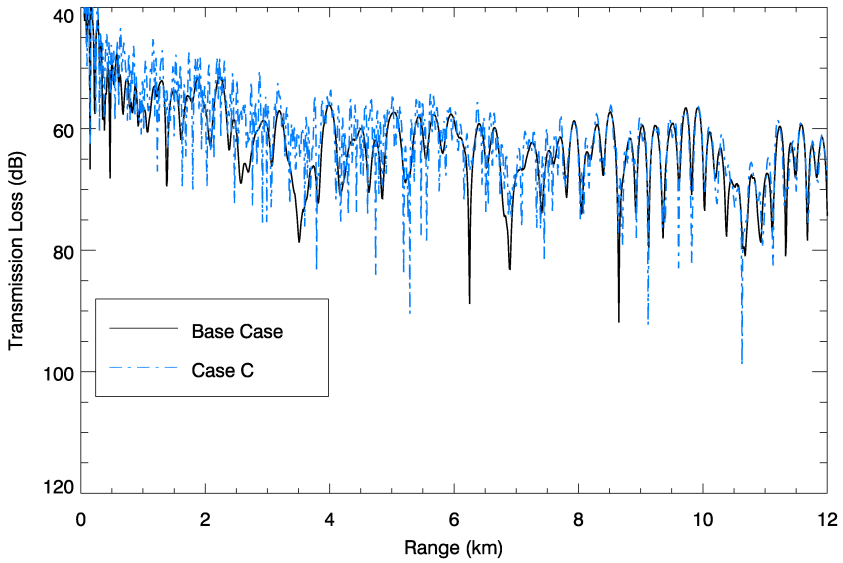

Figure 5.34: Transmission loss as a function of range at 54 m depth, computed using 3D calculations with geoacoustic model case C (blue) and for the base case(black).

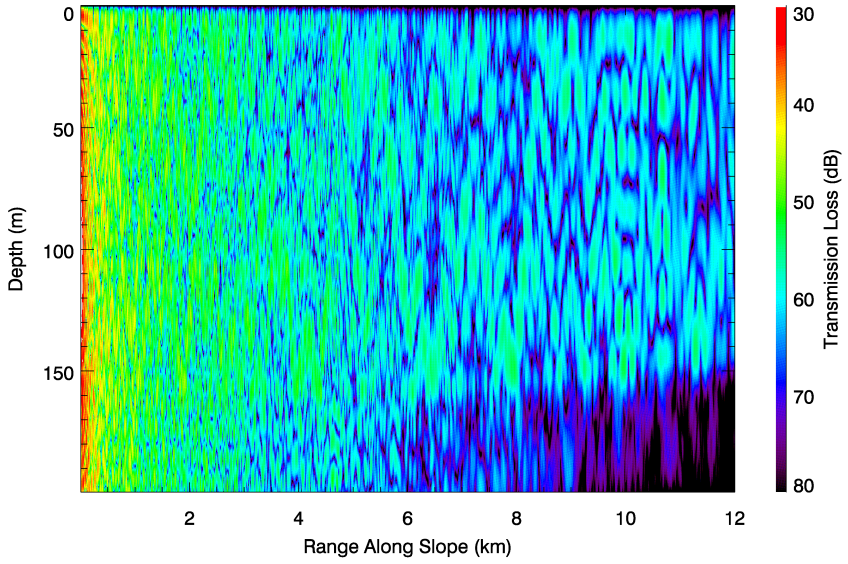

Figure 5.35: Transmission loss as a function of range and depth, computed using 3D calculations with geoacoustic model case C.

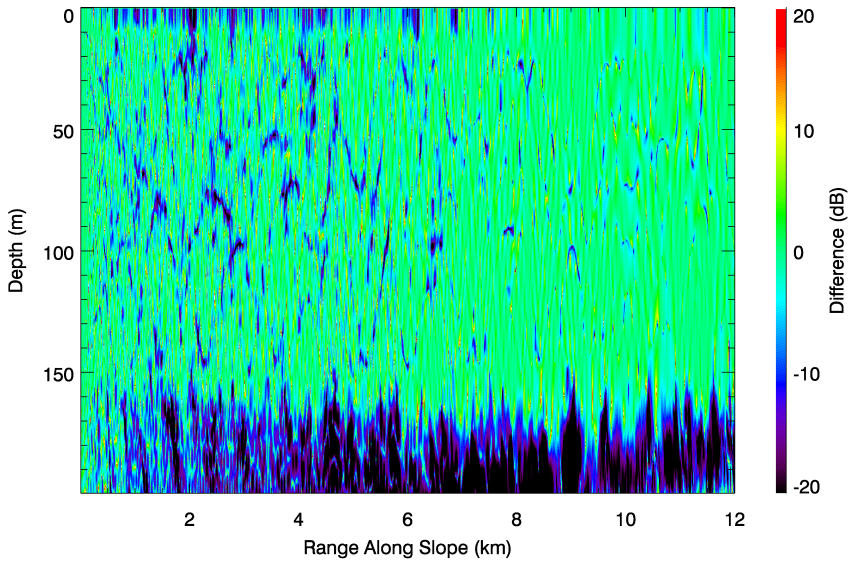

Figure 5.36: Difference between the field for geoacoustic model case C and that for the base model case.

of the spectrum corresponding to the lower-order modes is very similar compared to that for the base case, with the dominant modes at 10 km range again being modes 6 and 7.

Waveforms were generated for this model case and are shown in Figure 5.45 with the base model case waveforms plotted for comparison. The vertical beam pattern associated with these waveforms is shown in Figure 5.38 with the base model case beam pattern shown for comparison. The beam patterns are very similar. The model case C and the base model case waveforms are also very similar, particularly for times less than 7.1 s, indicating that the presence of the deep limestone layer has not had a strong influence on the received signals at 10 km range. This is because the important modes (modes less than mode 8) do not extend deep enough into the seafloor to sense the presence of the limestone as was shown in the mode function plots in Section 5.1.3. The addition of this layer has not improved the model-data mismatch in the arrival time of the later arrivals.

The addition of the limestone layer has not significantly altered the 3D simulated waveforms compared to the base model case parametrization. Waveforms from 2D PE calculations with the model case C parametrization were also generated and are shown in Figure 5.40. Here significant later arrivals of the higher order modes (with

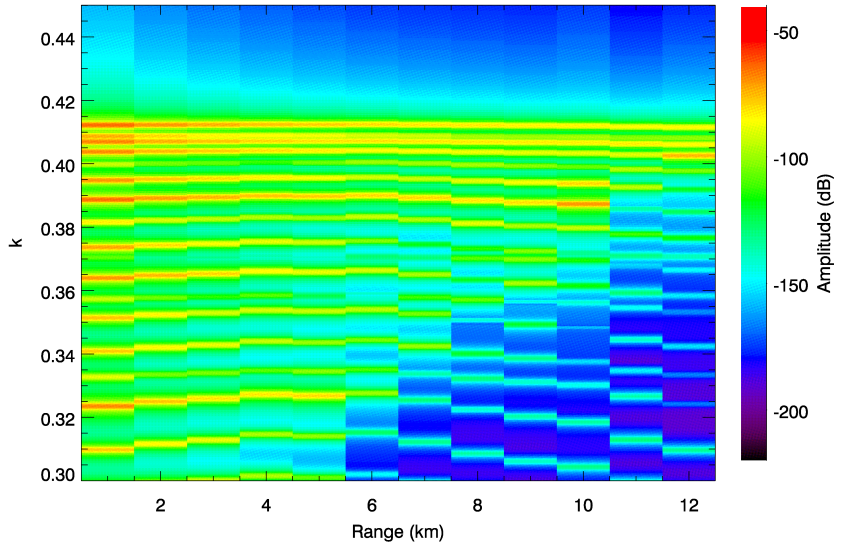

Figure 5.37: Wavenumber spectra as a function of range in the source-receiver plane from PE fields computed using 3D calculations, model case C.

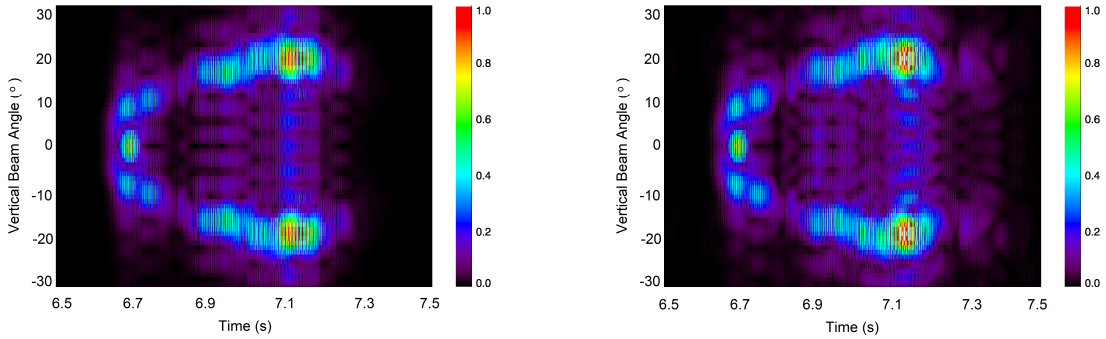

Figure 5.38: Vertical directionality of the modelled waveform from 3D calculations for (left) the base model case and (right) model case C.

slower group velocities) are observed at times greater than 7.1 s. These arrivals extend the signal in time and are not well matched to the data. As previously stated, these late-arrival modes are refracted down-slope and do not contribute significantly to the 3D field at 10 km range.

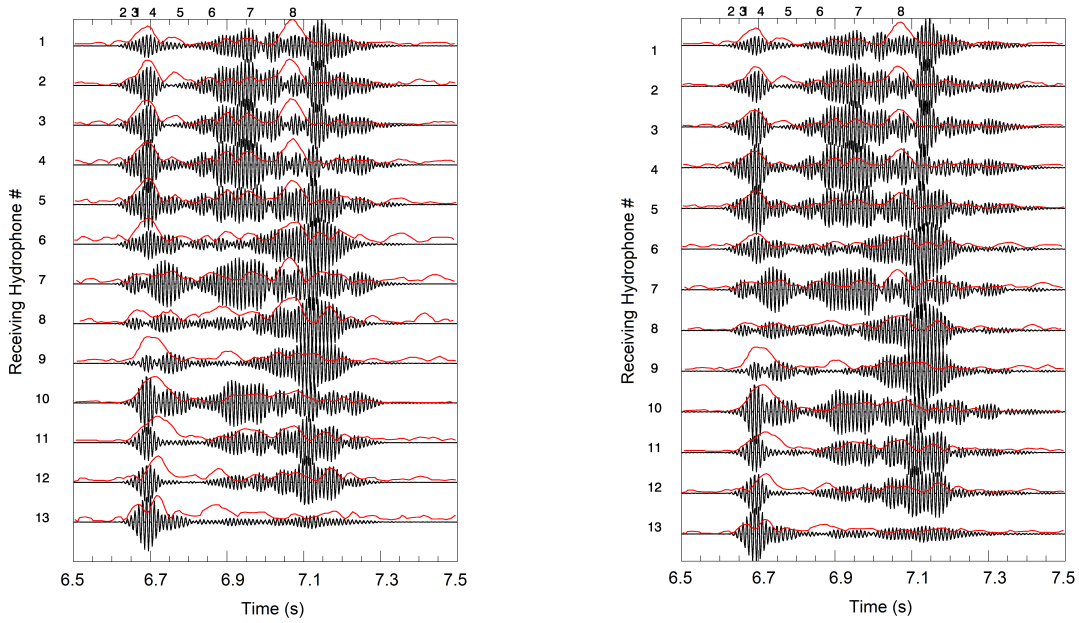

Figure 5.39: Simulated waveforms obtained through Fourier synthesis of PE fields computed using 3D calculations for the base model case (left) and for model case C (right). Red curves present the envelope of the measured data from the deFerrari experiment.

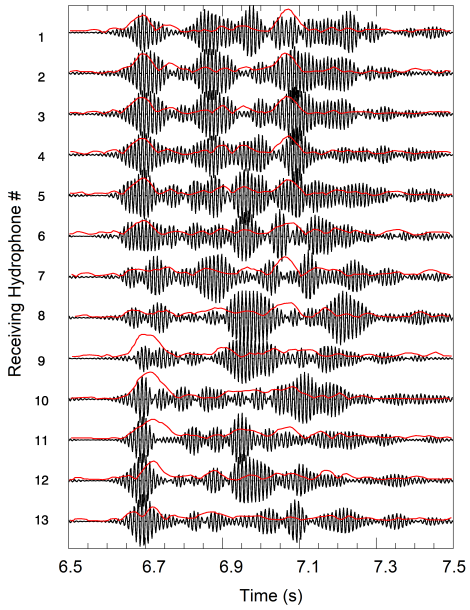

Figure 5.40: Simulated waveforms obtained through Fourier synthesis of PE fields computed using 2D calculations for model case C. Red curves represent the envelope of the measured data from the deFerrari experiment.

5.3.5 Model Case D: Range-dependent geoacoustic model

Finally MONM3D was run with range-dependent geoacoustics in the 3-province arrangement described in Section 5.1.3. In this case, in-plane propagation paths travel wholly within the base case environment of Province 1. Paths travelling slightly out of the source-receiver plane also remain within Province 1, but paths that travel further up-slope pass through the lossy environment of Province 2. Refracted paths that travel further up-slope couple into the source-receiver plane at longer ranges. Therefore, the field in the source-receiver plane will be influenced at close ranges by paths that have travelled only within Province 1 and at further ranges by paths that have also passed through Province 2.

It was shown in model case A that increased compressional attenuation reduces the high-order mode amplitudes; in fact, in model case A the modes were reduced to such a degree that the 3D effect was eliminated. The results from model case B have shown that the inclusion of shear also results in a reduction of mode amplitudes, but does not affect the higher order modes to such a strong degree. For model case D, the value for compressional attenuation in Province 2 is lower than the value used in model case A but it is expected that the amplitudes of modes 6 and 7 will be reduced as they pass through this province, particularly from the combined effect of the addition of shear. It is noted that modes 6 and 7 will not travel through Province 3 since they both reach their cutoff depth within 2 km range in the up-slope direction (see Figure 5.19).

Figure 5.41 presents the computed 3D TL for a receiver depth of 54 m in model case D; the base case results are also shown for comparison. Here the two curves are in very good agreement to a range of approximately 9 km, indicating that out-of-plane paths that couple into the plane at ranges $\leq$9 km have only travelled within Province 1. Beyond 9 km range significant differences in the TL curves are observed. This is because the paths that travel through Province 2 are more strongly refracted compared to the amount of refraction for the base model case as was shown in Figure 5.11. As was discussed previously, at this range there is a shadow zone in the source-receiver range for the mode 7 paths from Province 2. Refracted paths that couple into the plane at ranges beyond 9 km are only the paths which have remained in Province 1. In the base model case paths from the steep part of the slope (corresponding to Province 2) also couple into the plane at these ranges enhancing the 3D effect.

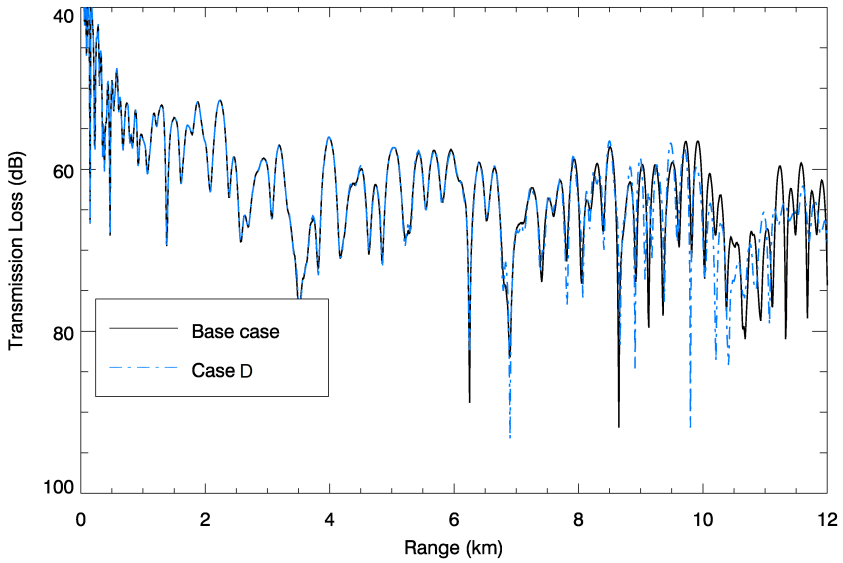

Figure 5.41: Transmission loss as a function of range at 54 m depth, computed using 3D calculations with geoacoustic model case D (blue), and for the base case(black).

A plot showing 3D TL versus cross-slope range at all depths for model case D is shown in Figure 5.42. The interference pattern contains the type of structure that was observed for the base case, attributed to interference of horizontally refracted sound paths that couple into the source-receiver plane. This 3D effect appears clearly up until about 9-10 km range for this model case, but beyond 9-10 km the effect is weaker compared to the base case. Again, this is because paths that couple into the source-receiver plane at these ranges have travelled through Province 2, where they have been more strongly refracted.

This comparison is more easily observed in the plot of Figure 5.43 which shows the difference of the field for model case D subtracted from the base case model. The fields are identical to a range of approximately 4 km and exhibit only very small differences to a range of 8 km. The field differences at ranges beyond 8 km are caused by the influence of paths which have travelled through Province 2.

The cool colors in this difference plot between 8 and 10 km range indicate areas where the field in model case D is of higher amplitude than the base case field. This is because the mode 7 paths from Province 2 create a caustic at these ranges in the model case D parametrization (see Section 5.1.3). Beyond 10 km range the warm colors in the plot indicate that the base case results are of higher amplitude than those

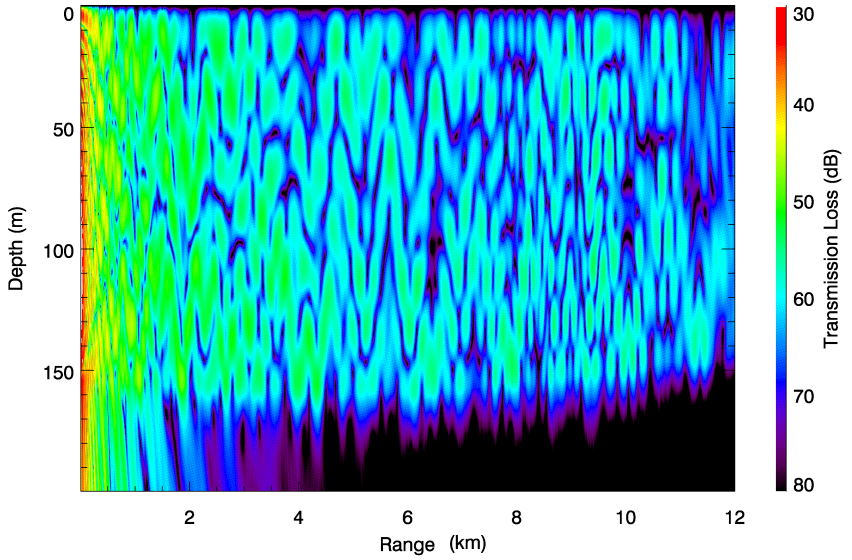

Figure 5.42: Transmission loss as a function of range and depth, computed using 3D calculations with model case D.

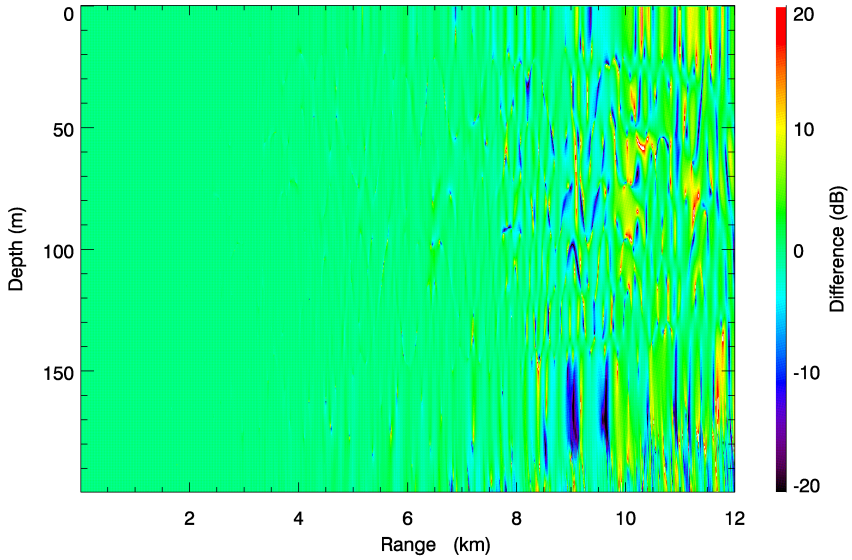

Figure 5.43: Difference between the field for geoacoustic model case D and that for the base model case.

of case D indicating that in this region the field is only influenced by the Province 1 paths.

The mode spectra for this model case, plotted in Figure 5.44, show that modes 6 and 7 contribute to the field at 10 km range, but with lower amplitude compared to the base case. The strongest contribution of mode 7 is now noted to occur at 9 km range and the amplitude of mode 7 at this range is greater than it was in the base case.

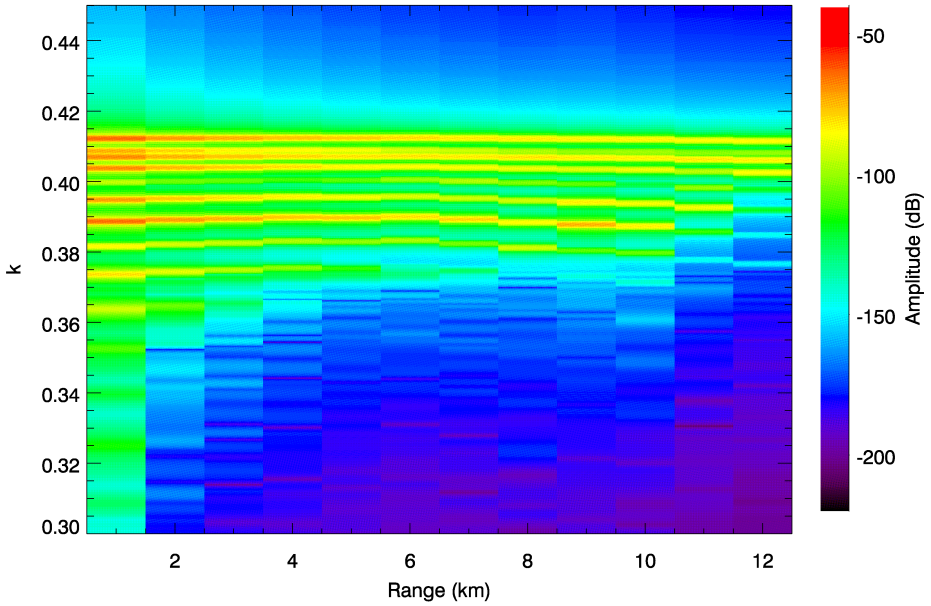

Figure 5.44: Wavenumber spectra as a function of range in the source-receiver plane from PE fields computed using 3D calculations, model case D.

Waveform plots for receivers at 10 km range for model case D are shown in the right-hand side of Figure 5.45, with the base case results shown on the left for comparison. The strong second arrivals are now apparent in the waveform plot between 7.0 and 7.1 s. This differs from the secondary arrival signals in the base case waveforms which are of longer-duration and occur between 7.0 and 7.2 s. The paths that contribute to the later part of the second arrival signal in the base case (at times >7.1 s) are from the steep-slope section of the slope and have been reduced in this case because they have refracted more sharply in 'Province 2' changing the shadow zone ranges for the modes. The case D result is in better agreement with the measured data since the later portion of the base case secondary arrival signal has been eliminated but, unlike model case A, the early part of the secondary arrival signal has been preserved.

The vertical beam pattern corresponding to these waveforms is plotted in Figure 5.46. Here the dominant bright spot of the secondary arrivals occurs at 7.1 s and corresponds to propagation angles of modes 6 and 7. The arrival time and duration of this late-arrival signal is in better alignment with the measured signal compared to the base case.

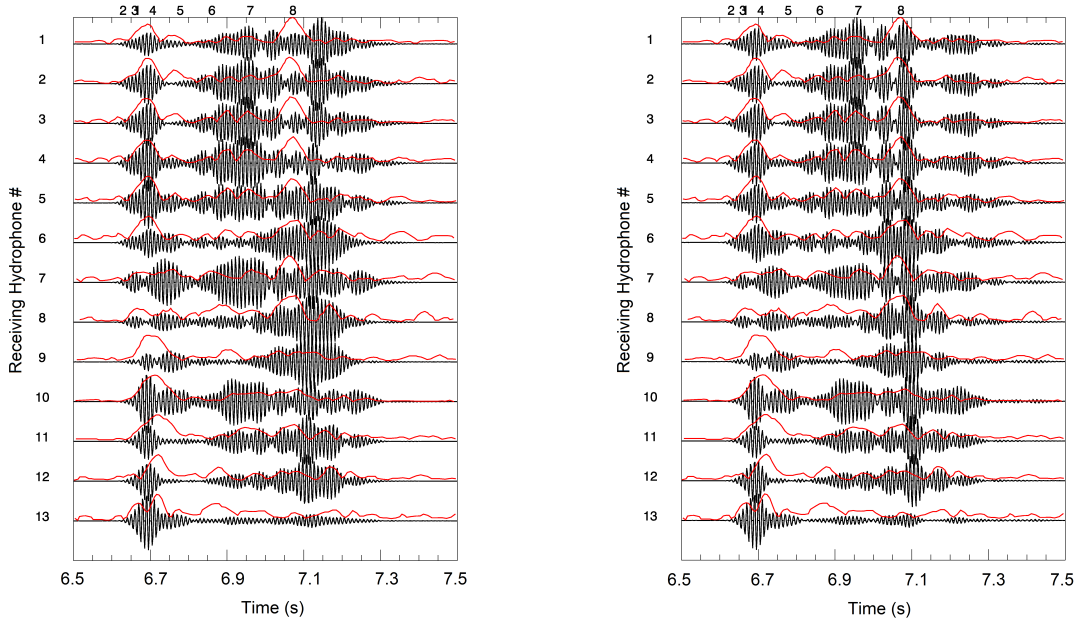

Figure 5.45: Simulated waveforms obtained through Fourier synthesis of PE fields computed using 3D calculations for the base model case (left) and for model case D (right). Red curves present the envelope of the measured data from the deFerrari experiment.

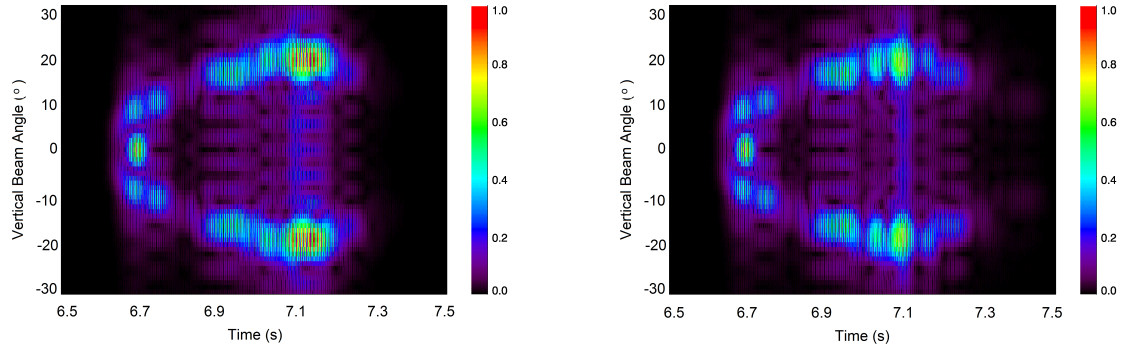

Figure 5.46: Vertical directionality of the modelled waveform from 3D calculations for (left) the base model case and (right) model case D.

The findings from these investigations can be summarized as follows:

- Strong secondary arrivals were observed in the simulated waveforms using the results of full 3D calculations. These arrivals were attributed mainly to refracted arrivals of modes 6 and 7. The arrivals were not present when 2D calculations were applied or when using a geoacoustic model that strongly attenuates modes 6 and 7.

- Model case D, with range-dependent geoacoustics, was the only model case that was able to provide a possible explanation for the model-data mismatch in the timing of the simulated second arrivals. In this case the received signal does not contain contributions from propagation paths of modes 6 and 7 that travel up the steep part of the slope where the sediments are more coarse. But, the contribution of the mode 6 and 7 paths that do not travel as far up-slope before coupling into the source-receiver plane are preserved.

- Introduction of a deeper seafloor layer of limestone, consistent with the expected geology of the area, did not improve the model-data timing mismatch. This is because the modes that dominantly contribute to the received waveforms do not extend deep enough into the seafloor to sense the presence of a deep limestone layer.

- The simulated first arrivals were well matched to the data and were composed of lower-order modes. The model-data agreement for the early arrivals of the waveform was not influenced by the 3D effect with the first arrival being fairly well matched by all model cases, including the 2D calculations. Therefore the low order modes are weakly influenced by the horizontal refraction and do not contribute dominantly to the secondary arrivals.

- The base case model provides a good match to the data that travels mostly within the source-receiver plane but the geoacoustic environment most likely varies in the up-slope direction.

Chapter 6

Summary

An important advancement in sound propagation modelling has been the development of methods to account for three-dimensional sound propagation effects. The 3D parabolic equation model (MONM3D) that has been presented in this work takes advantage of these methods to provide researchers at JASCO Applied Sciences with a valuable leading-edge tool for noise impact assessment in environments with complicated bathymetry. Though the 3D calculations are still very computationally intensive, the unique definition of the model grid in MONM3D has been shown to improve the computational efficiency of the model by approximately 30% [2]. MONM3D has been shown to be consistent with benchmark results and has also been shown to be appropriate for the study of propagation effects in a realistic ocean environment.

MONM3D has been shown to be effective as an analysis tool for the Florida Strait environment. This exercise demonstrated the ability of MONM3D to model sound propagation (in fact, to simulate pulse propagation) in a complicated environment. Interpretation of the MONM3D output allowed an analysis of the characteristics of the environment specific to the Florida Strait test facility. Based on this analysis it is assumed that the geoacoustic properties at the test case site are likely range-dependent in the shoreward direction. It was found that the low-order modes in the considered dataset are not affected by 3D propagation effects. These modes propagate at small grazing angles and do not carry information about the deeper seafloor structure. The higher-order modes with steeper angles of propagation are influenced by 3D propagation effects and can be influenced by changes of the geoacoustic model parameters. Examination of the behaviour of these higher order modes provides insight into the characteristics of the deeper seafloor structure and of the environment outside of the source-receiver plane. This sort of analysis is important to others con-

ducting experiments at the South Florida Ocean Measurement Center and could be useful for site selection for future experiments.

This work incorporated several useful forms of analysis that can be applied directly to the output from a PE model to assist in the interpretation of modelled fields and measured datasets containing the influence of 3D propagation effects. Of particular importance in this investigation was the consideration of the behaviour of individual modes. The modal decomposition approach applied in this analysis allowed the range evolution of the wave-number spectra to be obtained directly from the full PE field without requiring the need to model the mode functions with a separate normal mode code or to propagate individual modes separately through the environment. This type of analysis had been previously only applied to 2D PE fields [49]. At the outset it was not known if the 3D effects would hinder this analysis technique, but in fact the technique was found to provide useful information describing the behaviour of the modes. This allowed the relative contributions of the different modes to be studied as a function of range from the source. Consideration of the horizontal ray path diagrams for this environment assisted in definitive interpretation of the computed mode spectra. Simulation of propagated pulse waveforms, combined with vertical beamforming applied at the receiving array, provided insight into the mode arrival times and aided in the interpretation of the influences that the environment parameters had on each mode. These analysis techniques can be used in future for interpreting modelled sound fields.

In terms of noise impact assessment, this work has shown that 3D propagation effects can be important in non-radially symmetric environments. Examination of the Florida Strait test case has shown that horizontal refraction can give rise to multiple arrivals of pulsed sound. This can affect the duration and the total sound energy in the received pulses. This could be important in assessing noise impacts from pulsed sounds such as airgun signals, an industrial noise source that is often considered in noise impact assessments. Limitations of the model for its use in noise assessment include the large amount of memory required for model grids that extend far in range, particularly at high frequencies where fine grid resolution is required. It is expected that continued improvement of the model's efficiency will take place as it is applied for real world problems.

Bibliography

[1] J. I. Arvelo and A. P. Rosenberg. Three-dimensional effects on sound propagation and matched-field processor performance. *Journal of Computational Acoustics*, 9(1):17–39, 2001.

[2] M. E. Austin and N. R. Chapman. The use of tessellation in three-dimensional parabolic equation modeling. *Journal of Computational Acoustics*, 19(3):221–239, 2011.

[3] M. Badiey, B. G. Katsnelson, J. F. Lynch, S. Pereselkov, and W. L. Siegman. Measurement and modeling of three-dimensional sound intensity variations due to shallow-water internal waves. *Journal of the Acoustical Society of America*, (2):613–625, 2005.

[4] R. N. Baer. Propagation through a three-dimensional eddy including effects on an array. *Journal of the Acoustical Society of America*, 69, number =.

[5] T. G. Birdsall and Jr. K. Metzger. M-sequence signal tutorial. Technical report, Naval Oceanographic Office, 1988.

[6] G. Botseas, D. Lee, and D. King. For3d: A computer model for solving the lss three-dimensional wide anlge wave equation. Technical Report 7934, Naval Underwater Systems Center, New London, CT, 1987.

[7] G. H. Brooke, D. J. Thomson, and G. R. Ebbeson. PECan : A Canadian parabolic equation model for underwater sound propagation. *Journal of Computational Acoustics*, 9(1):69–100, 2001.

[8] NOAA National Geophysical Data Center. U.S. Coastal Relief Model. http://www.ngdc.noaa.gov/mgg/coastal/crm.html, Retrieved March 2011.

[9] W. B. Charm, W. D. Nesteroff, and S. Valdes. Detailed stratigraphic description of the joides cores on the continental margin off florida. Technical report, United States Department of the Interior, Geological Survey, 1965.

[10] L.Y.S. Chiu, Y.-T. Lin, C.-F. Chen, T. F. Duda, and B. Calder. Focused sound from three-dimensional sound propagation effects over a submarine canyon. *Journal of the Acoustical Society of America*, 129(6):EL260–EL266, May 2011.

[11] M. D. Collins. Higher-order Padé approximations for accurate and stable elastic parabolic equations with application to interface wave propagation. *Journal of the Acoustical Society of America*, 89(3):1050–1057, 1991.

[12] M. D. Collins. A split-step Padé solution for the parabolic equation method. *Journal of the Acoustical Society of America*, 93(4):1736–1742, 1993.

[13] M. D. Collins. *Users Guide for RAM versions 1.0 and 1.0p*. Naval Research Lab, Washington, DC, 1995.

[14] M. D. Collins, R. J. Cederberg, D. B. King, and S. A. Chin-Bing. Comparison of algorithms for solving parabolic wave equations. *Journal of the Acoustical Society of America*, 100(1):178–182, 1996.

[15] M. D. Collins and S. Chin-Bing. A three-dimensional parabolic equation model that includes the effects of rough boundaries. *Journal of the Acoustical Society of America*, 87(3):1104–1109, 1990.

[16] M. D. Collins and S. A. Ching-Bing. A three-dimensional parabolic equation model that includes the effects of rough boundaries. *Journal of the Acoustical Society of America*, 87(3):1104–1109, 1990.

[17] M. D. Collins and R. B. Evans. A two-way parabolic equation for acoustic backscattering in the ocean. *Journal of the Acoustical Society of America*, 91(3):1357–1368, 1992.

[18] J. A. Davis, D. White, and R. C. Cavanagh. NORDA parabolic equation workshop. Technical Report 143, NORDA Surveillance Environmental Acoustic Support (SEAS) Project, 31 March - 3 April 1982.

[19] T. F. Duda. Initial results from a cartesian three-dimensional parabolic equation acoustic propagation code. Technical Report WHOI-2006-14, Woods Hole Oceanographic Institution, 2006.

[20] G. R. Ebbeson, D. J. Thomson, and B. H. Maranda. Spectral decomposition of underwater sound received on a vertical line array. In *IEEE Oceans Proceedings 3*, pages 1336–1343, 1991.

[21] J. A. Fawcett. Modelling three-dimensional propagation in an oceanic wedge using parabolic equation methods. *Journal of the Acoustical Society of America*, 93(5):2627–2632, 1993.

[22] M. D. Feit and J. A. Fleck. Computation of mode properties in optical fiber waveguides by a propagating beam method. *Applied Optics*, 19:1154–1164, 1980.

[23] S. D. Frank, M. Badiey, J. F. Lynch, and W. L. Siegmann. Experimental evience of three-dimensional acoustic propagation caused by nonlinear internal waves. *Journal of the Acoustical Society of America*, 118(2):723–734, 2005.

[24] E. L. Hamilton. Geoacoustic modelling of the sea floor. *Journal of the Acoustical Society of America*, 68:1313–1340, 1980.

[25] D. E. Hannay and R. G. Racca. Acoustic model validation. Technical Report 0000-S-90-04-T-7006-00-E, Sakhalin Energy Investment Company, 2005.

[26] C. H. Harrison. Three-dimensional ray paths in basins, troughs, and near seamounts by use of ray invariants. *Journal of the Acoustical Society of America*, 62(6):1382–1388, 1977.

[27] C. H. Harrison. Acoustic shadow zones in the horizontal plane. *Journal of the Acoustical Society of America*, 65(1):56–61, 1979.

[28] C. H. Harrison. Some rules-of-thumb for calculatoing 3d ray paths, modal refraction and modal shadow zones in shallow water. *Proceedings of the 3rd International Conference and Exhibition of Underwater Acoustic Measurements, Technologies and Results*, June 2009.

[29] K. D. Heaney and J. J. Murray. Measurements of three-dimensional propagation in a continental shelf environment. *Journal of the Acoustical Society of America*, 125(3):1394–1402, 2009.

[30] J. M. Hovem. (sin x)/x interpolation of sampled signals. Technical Report No 196, North Atlantic Treaty Organization Sclant ASW Research Centre, La Spezia, Italy, 1971.

[31] D. R. Jackson and M. D. Richardson. *High-Frequency Seafloor Acoustics*. The underwater acoustics series. Springer Science and Business Media, New York, NY, 2007.

[32] F. B. Jensen and C. M. Ferla. Numerical solutions of range-dependent benchmark problems in ocean acoustics. *Journal of the Acoustical Society of America*, 87(4):1499–1510, 1990.

[33] Y. Jiang, N. R. Chapman, and H. A. DeFerrari. Geoacoustic inversion of broadband data by matched beam processing. *Journal of the Acoustical Society of America*, 119(6):3707–3716, 2006.

[34] D. Lee, G. Botseas, and W. L. Siegmann. Examination of three-dimensional effects using a propagation model with azimuthal-coupling capability (for3d). *Journal of the Acoustical Society of America*, 91(6):3192–3202, 1992.

[35] D. Lee and A. D. Pierce. Parabolic equation development in recent decade. *Journal of Computational Acoustics*, 3:95–173, 1995.

[36] Y.-T. Lin, T. F. Duda, and J. F. Lynch. Acoustic mode radiation from the termination of a truncated nonlinear internal gravity wave duct in a shallow ocean area. *Journal of the Acoustical Society of America*, 126(4):1752–1765, 2009.

[37] D. F. McNeill. Sedimentology, physical properties, and acoustic response of sediment from piston cores at the south florida test facility. Data report, Comparative Sedimentology Laboratory, Division of Marine Geology and Geophysics, Rosenstiel School of Marine and Atmospheric Science, University of Miami, 2001.

[38] H. B. Nguyen, H. A. DeFerrari, and N. J. Williams. Ocean acoustic sensor installation at the South Florida Ocean Measurement Center. *IEEE Journal of Oceanic Engineering*, 27:235–244, 2003.

[39] M. B. Porter. The kraken normal mode code. Technical report, SACLANT Undersea Research Centre, 1989.

[40] M. B. Porter, F. B. Jensen, and C. M. Ferla. The problem of energy conservation in one-way models. *Journal of the Acoustical Society of America*, 89(3):1058–1067, 1991.

[41] C. E. Shannon. Communication in the presence of noise. *Proceedings of the IEEE*, 72:1192, 1984.

[42] K. B. Smith. A three-dimensional propagation algorithm using finite azimuthal aperture. *Journal of the Acoustical Society of America*, 106(6):3231–3239, 1999.

[43] K. B. Smith. Convergence, stability, and variability of shallow water acoustic predicitions using a split-step fourier parabolic equation model. *Journal of Computational Acoustics*, 9(1):243–285, 2001.

[44] F. Sturm. Numerical study of broadband sound pulse propagation in three-dimensional oceanic waveguides. *Journal of the Acoustical Society of America*, 117(3):1058–1079, 2005.

[45] F. Sturm and J. Fawcett. On the use of higher-order azimuthal schemes in 3d pe modeling. *Journal of the Acoustical Society of America*, 113(6):3134–3145, 2003.

[46] F. Sturm, S. Ivansson, Y. Jiang, and N. R. Chapman. Case study concerning 3-d out-of-plane sound propagation in shallow water. In M. Taroudakis and P. Papadakis, editors, *Proceedings of the 8th International Conference on Theoretical and Computational Acoustics, Herakion Crete Greece*, pages 299–309, July 2007.

[47] F. Sturm, A. Korakas, and J.-P. Sessarego. Results of matched-field inversion in a three-dimensional wedge-like environment. In *10th European Conference on Underwater Acoustics*, Istanbul, Turkey, July 2010.

[48] F. D. Tappert. The parabolic approximation method. In J. B. Keller and J. S. Papadakis, editors, *Wave Propagation and Underwater Acoustics, Lecture Notes in Physics*, volume 70, chapter V, pages 224–287. Springer-Verlag, New York, 1977.

[49] D. J. Thomson and G. H. Brooke. *Parabolic equation techniques in underwater acoustics*, pages 135–173. Chapman and Hall/CRC, 2008.

[50] A. Tolstoy. 3d propagation issues and models. *Journal of Computational Acoustics*, 4(3):243–271, 1996.

[51] H. Weinberg and R. Burridge. Horizontal ray theory for ocean acoustics. *Journal of the Acoustical Society of America*, 55(1):63–79, 1974.

[52] D. E. Weston. Guided propagation in a slowly varying medium. *Proceedings of the Physical Society*, 73:365–384, 1959.

[53] E. K. Westwood. Ray model solutions to the benchmark wedge problems. *Journal of the Acoustical Society of America*, 87(4):1539–1545, 1990.

[54] E. K. Westwood, C. T. Tindle, and N. R. Chapman. A normal mode model for acousto-elastic ocean environments. *Journal of the Acoustical Society of America*, 100(6):3631–3645, 1996.

[55] Y. Zhang and C. Tindle. Improved equivalent fluid approximations for a low shear speed ocean bottom. *Journal of the Acoustical Society of America*, 98(6):3391–3396, 1995.

Appendix A

Model Performance

The overall performance of MONM3D as it has been applied in this research is considered in this Appendix. Consideration is given to the validity of the results and the potential sources of error. The performance of the model including tessellation is also examined and computation times are assessed.

A.1 Convergence - Azimuthal Grid Spacing

The computational grid for a 3D numerical model in spherical coordinates is discretized according to defined spacings in depth (Δz), in range (Δr), and in azimuth ($\Delta\varphi$). The value for Δz should be chosen to provide an appropriate depth sampling for the model frequency. A general rule of thumb for models based on the split-step Padé approach is to select Δz to be on the order of tenths of a wavelength ($\frac{\lambda}{100} < \Delta z < \frac{\lambda}{10}$) [1]. Values for the grid spacings in range and azimuth depend on the operator approximations that are being applied and should be appropriate for the strength of the environmental variability. For example, Δr and $\Delta\varphi$ can be quite large (several wavelengths) for weakly range-dependent environments but smaller values of Δr or $\Delta\varphi$ are often required for model environments with steeply sloped seafloors [13].

For sloped environments, Arvelo and Rosenberg [1] proposed that Δr and $\Delta\varphi$ can be related to a ratio of the vertical grid spacing and the maximum radial or azimuthal slope of the seafloor. Since these relationships for Δr and $\Delta\varphi$ depend on the vertical grid spacing Δz they also indirectly relate to the frequency, as might be expected.

The equation they proposed for the radial grid spacing is:

$$\Delta r = \frac{\Delta z}{S_{r,max}} \tag{A.1}$$

where $S_{r,max}$ is the maximum slope of the seafloor along any radial path in the computation grid [1]. This says that the ratio of the vertical to radial grid spacings should be comparable to the maximum radial slope of the seafloor. This equation is valid for models based on the split-step Padé approximation with a small number (1 or 2) of Padé terms. If more Padé terms are included then the approximation is accurate to higher order so this relationship can be relaxed and larger spacing in range can be used.

Similarly, Arvelo and Rosenberg suggest the following relationship for the azimuthal grid spacing (expressed as an angular separation, in radians):

$$\Delta \varphi = \frac{\Delta z}{R S_{\varphi,max}} \tag{A.2}$$

where R is the maximum range of computation and $S_{\varphi,max}$ is the maximum seafloor slope in the azimuthal direction. While these rules of thumb are useful as a starting point for determining appropriate grid spacings, truly it is prudent to conduct convergence testing with each model in each new environment.

For the Florida Strait test environment considered in this research, the depth spacing was set to $\Delta z = 0.5$ m$= \frac{\lambda}{30}$ and the range spacing was $\Delta r = 10$ m which is appropriate for a seafloor with a radial slope of $\sim 3^\circ$ according to the relationship shown above. These values are consistent with those used in the Sturm analysis [46] and with values that would be typically applied in MONM to model 2D propagation at 100 Hz. The azimuthal grid spacing Δs_{max} (the arc-length separation between adjacent points in azimuth) was selected through convergence testing based on the Base Case model parameters. Several realizations of the model were compared using various values for Δs_{max}. Model simulations were computed using the Fourier approach to implement the azimuthal operator and separately using the 4^{th}-order finite-difference approach. First, the maximum acceptable arc-length separation was set to $\Delta s_{max} = 25$ m, the value from the Fawcett wedge benchmark test. Then the value for Δs_{max} was decreased to a value of 12 m and the models were re-run.

Curves of TL versus range in the source-receiver plane for each of these calculations are shown in Figures A.1 (all ranges) and A.2 (zoomed to ranges from 7-11 km) .

The blue and green curves show the results for the Fourier approach with Δs_{max} = 12 and 25 m respectively. There are some ranges for which the curves are very slightly out of phase but in general these curves are in excellent agreement with only small discrepancies (around 1-2 dB) out to the 10 km receiver range. The solution is considered to have converged for this operator approximation. The black and red curves present the data resulting from the finite difference approximation, again for Δs_{max} = 12 and 25 m respectively. These curves show greater discrepancies, both from each other and also from the results based on the Fourier approximation and the solution has not yet converged for this operator. Based on this analysis, the results presented in Chapter 5 were all generated using the Fourier approach in azimuth, with Δs_{max} = 12 m.

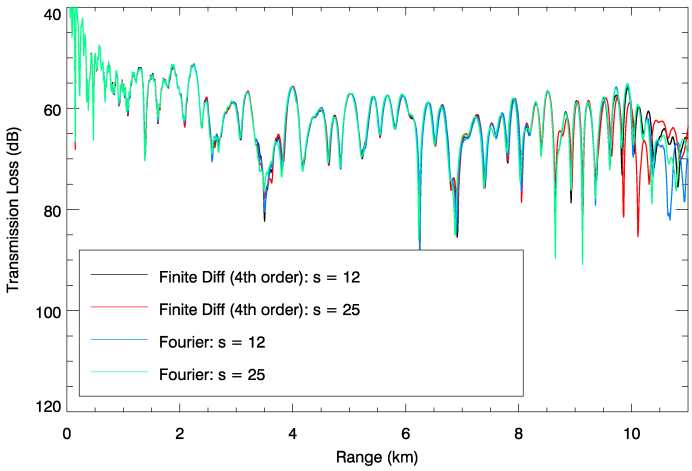

Figure A.1: Transmission loss as a function of range [0 to 11 km] computed using 3D calculations showing convergence for different azimuthal operators.

The maximum azimuthal slope at 10 km range in the Florida Strait test case is $S_{\varphi,max}$ = 0.084. With Δz = 0.5 m, the Arvelo and Rosenberg relationship in Equation (A.2) would suggest an acceptable azimuthal step size of:

$$\Delta\varphi = \frac{\Delta z}{RS_{\varphi,max}} = \frac{0.5}{(10000)(0.084)} = 0.000595 \text{ rad} = 0.034^{\circ} \tag{A.3}$$

This angular separation equates to an arc-length separation at 10 km range of:

$$\Delta s_{max} = R\Delta\varphi = (10000)(0.000595) = 5.95\ m \tag{A.4}$$

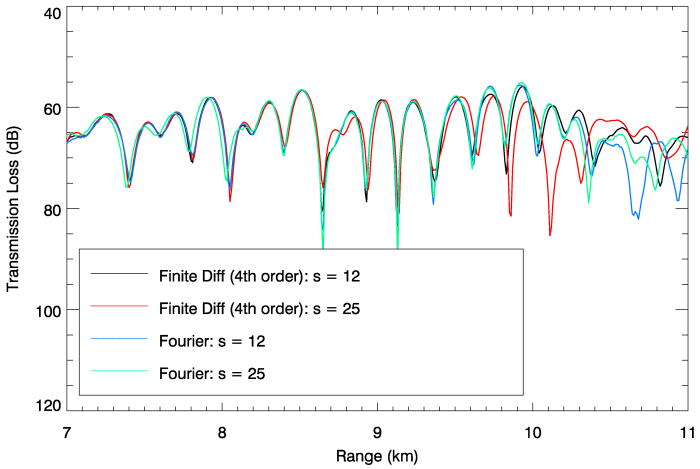

Figure A.2: Transmission loss as a function of range [7 to 11 km] computed using 3D calculations showing convergence for different azimuthal operators.

Therefore it is not surprising that the finite-difference approximation has not converged for the Florida Strait test environment at 100 Hz with $\Delta s_{max} = 12$ m.

Convergence was obtained, however, using the Fourier operator approach with $\Delta s_{max} = 12$ m, in which case there were 8192 radials in the grid at 10 km range. This equates to a slightly wider acceptable azimuthal spacing expressed as an angular separation of:

$$\Delta\varphi = \frac{360}{8192} = 0.044^{\circ} \tag{A.5}$$

This indicates that the relationship in Equation (A.2) is overly conservative for the Fourier approach applied in MONM3D. This is consistent with the assumption that the Fourier approach permits wider azimuthal spacing over finite difference approaches, as was discussed in Section 3.1.2. This testing has shown that the relationship could perhaps be modified for the Fourier operator approach to be:

$$\Delta\varphi = \frac{5\Delta z}{4RS_{\theta,max}} \tag{A.6}$$

as a first approximation for the azimuthal grid spacing. Again, convergence testing should be conducted for each new test environment to ensure an appropriate grid discretization.

It is interesting to note the relationship between the azimuthal grid spacing and frequency. Consider that the Fawcett Wedge test runs at 25 Hz frequency (Section 4.2)

were consistent with published (converged) model results using the 4^{th}-order finite-difference approach with an azimuthal grid spacing $\Delta s_{max} = 27$ m (5760 radials at 25 km range). Assuming that there is an inverse relationship between azimuthal spacing and wavelength, one could expect that for calculations at 100 Hz the acceptable azimuthal grid spacing would need to reduce from 27 by approximately a factor of 4 (100 Hz / 25 Hz). This would give

$$\Delta s_{max} = \frac{27}{4} = 6.75\ m \tag{A.7}$$

or

$$\Delta\varphi = \frac{\Delta s_{max}}{R} = \frac{6.75}{10000} = 0.000675 rad = 0.039^{\circ} \tag{A.8}$$

which is consistent with (though slightly larger than) the Arvelo relationship shown above.

Convergence testing was also applied separately for the model case D parameters (using only the Fourier operator approach) to ensure that the spacing was appropriate in the case where the geoacoustic parameters vary with range. As was done using the base case parameters, the model was run using the case D parameters with $\Delta s_{max} = 25$ and again with $\Delta s_{max} = 12$ for comparison. The results are shown in Figures A.3 and A.4. the two curves are still in excellent agreement and the spacing of $\Delta s_{max} = 12$ m is considered appropriate for this test case.

A.2 Sources of Error

The approximations inherent in the derivation of the parabolic equation can lead to accuracy limitations of the model results in certain environments. This section will consider some of the key approximations which underly the MONM3D algorithm and the consequences these approximations have for the test cases contained in this manuscript.

Without correction, the one-way (outgoing) parabolic approximation is known to be susceptible to errors that arise from the approximate representation that is used to model environments with range-dependent bathymetry [40]. A sloping seafloor is represented approximately using a stair-step approach to divide the slope into range-independent segments with constant bathymetry (see Figure A.5). In this stair-step representation there are vertical boundaries along the 'rise' of the steps at the inter-

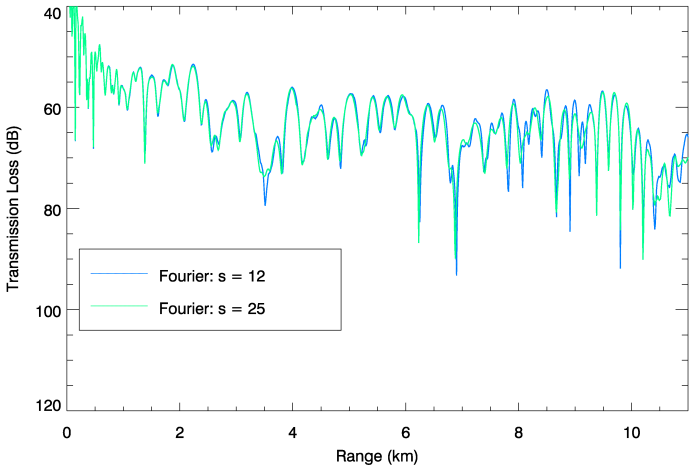

Figure A.3: Transmission loss as a function of range [0 to 11 km] computed using 3D calculations for the Florida Strait test environment, case D, for different azimuthal spacing.

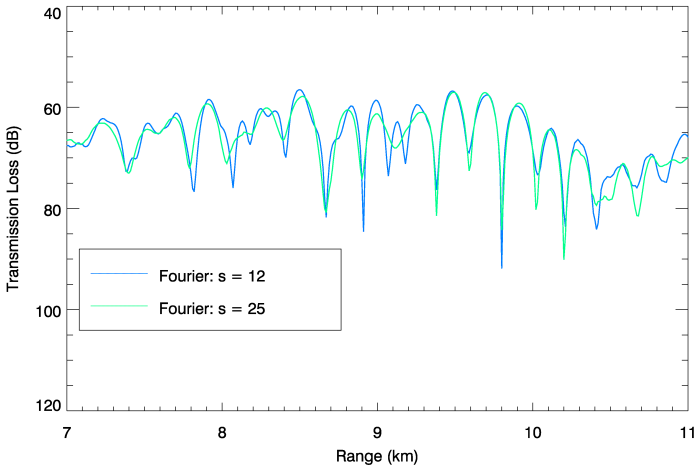

Figure A.4: Transmission loss as a function of range [7 to 11 km] computed using 3D calculations for the Florida Strait test environment, case D, for different azimuthal spacing.

faces between range-independent regions. The boundary conditions at the interfaces require the displacement and normal stress to be continuous across the boundary. The parabolic equation contains only a single derivative in range; therefore only a single boundary condition can be satisfied and energy is not conserved through the

field [40]. As is done in RAM, MONM3D addresses this known energy conserving issue by propagating an 'impedance reduced pressure' $p/\sqrt{\rho c}$ rather than p. The reduced pressure is properly matched across the vertical interfaces in most problems [13, 7].

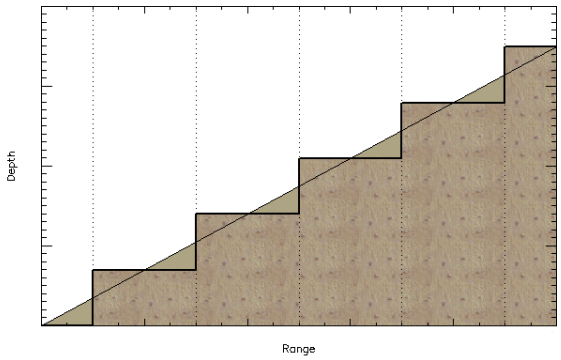

Figure A.5: Stair-step approximation of a sloped seafloor.

Backscattered energy is necessarily neglected in the parabolic approximation. Errors arising from the neglect of this backscattered energy have been previously considered for a test environment with a simple sloped seafloor [53]. Results from a two-way model were used to show that this approximation is not a significant source of error, at least for the ASA wedge benchmark, with backscattered levels being much lower than the levels propagating in the forward direction. The slope of the Florida Strait seafloor is similar to that of the ASA wedge, so the effect of backscatter is also assumed not be important for the case presented in this work.

In this work the MONM3D calling engine was adapted to take advantage of the ability for RAM to consider range-dependent geoacoustics in addition to variable bathymetry. There will be vertical interfaces between different geoacoustic provinces which are also susceptible to errors of energy conservation. Since these fluid-fluid interfaces are similar to those along the rises of the stair-step bathymetric approximation, the issue of energy conservation is again dealt with by propagating the reduced pressure through the field. As well, there is potential for reflection from these interfaces that would not be captured in the outgoing PE model. In the absence of a benchmark against which to test for errors of this nature, it is assumed that backscatter from the inter-province interfaces would be negligible as is the backscatter from the stair-step approximation for bathymetry.

To investigate potential errors strictly due to the implementation of range-dependent geoacoustics in MONM3D, results in the up-slope direction were compared with RAM

calculations using the same geoacoustic range dependence (note that in the up-slope direction the propagation effects are fully 2D enabling this comparison with a 2D model). A modified version of RAM was used for this comparison that includes the complex density approximation to account for shear that is contained in MONM3D. The two models are in excellent agreement as is shown in Figure A.6. Since the azimuthal operator in MONM3D does not contain any terms that depend on the properties of the environment, the geoacoustic range dependence is assumed to influence only the 'range stepping' part of the MONM3D algorithm, which has been here shown to be consistent with RAM.

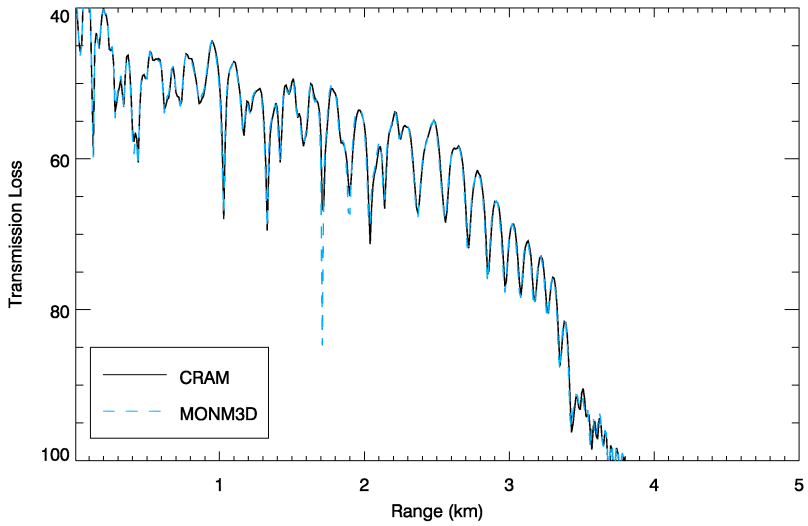

Figure A.6: Transmission loss as a function of upslope range computed using MONM3D and CRAM for Florida Strait test environment, model case D.

A.3 Model Performance - Tessellation

This section will examine the efficiency gain achieved through application of a tessellated model grid by comparison of the computation time required for a tessellated

and a non-tessellated model run. The example shown is based on 3D calculations at 100 Hz for the Florida Strait test environment from Chapter 5. Calculations were performed with an Intel Core i5 M540 2.53GHz processor on a 32-bit Windows Operating system with 3GB of RAM.

Non-tessellated MONM3D results were obtained with the maximum acceptable arc-length separation, Δs_{max}, set to 100000 m (a very large number to ensure that no tessellation would occur) and the number of radials set to $N_\varphi = 8192$. With this configuration the computation grid contained a fixed number of points in azimuth for all ranges. The value $N_\varphi = 8192$ is appropriate to achieve an acceptable separation between radials at 10 km, the maximum range of interest for this test case (see Section A.1).

Table A.1: Tessellation points for the Florida Strait test case with $\Delta s_{max} = 12$ m.

	N_φ	Range (km)	Computation Time
Tessellated	256	0.0 - 0.47	0h00m40s
	512	0.48 - 0.96	0h01m14s
	1024	0.97 - 1.94	0h05m31s
	2048	1.95 - 3.90	0h23m06s
	4096	3.91 - 7.81	1h29m22s
	8192	7.82 - 12.0	3h40m13s
		Total	**5h40m06s**
Non-tessellated	8192	0.0 - 12.0	7h35m34s

Tessellated MONM3D results were obtained with Δs_{max} set to 12 and the grid was initiated with $N_\varphi(r_0) = 256$ at the source range. The ranges of tessellation (i.e. ranges where the azimuthal grid size was doubled) are indicated in Table A.1 for this configuration. The first tessellation occurred at 480 m range, and the range increment doubled between subsequent tessellations. The elapsed times for 3D calculations in each tessellated segment are provided in the table, as are the total computation times for the tessellated and non-tessellated runs. A 25% increase in efficiency was achieved through application of the tessellated model grid for the Florida Strait test case at 100 Hz, modelled over a 12 km^2 region of interest. This equated to a computational savings of 1.92 hours for this example. Calculations for the Fawcett wedge test case found a 33% increase in efficiency for simulations at 25 Hz on a 2.66 GHz Intel Xenon X3350 processor [2].

Transmission loss at 55 m depth as a function of range in the source-receiver plane

is shown in Figure A.7. This plot compares the tessellated result (plotted in solid black) with the non-tessellated result (in dashed blue) as was shown in Section 4.2 for the truncated wedge validation test case. The two results are indistinguishable, again confirming that the application of the tesselated model grid (and the associated radial interpolation scheme) does not affect the results.

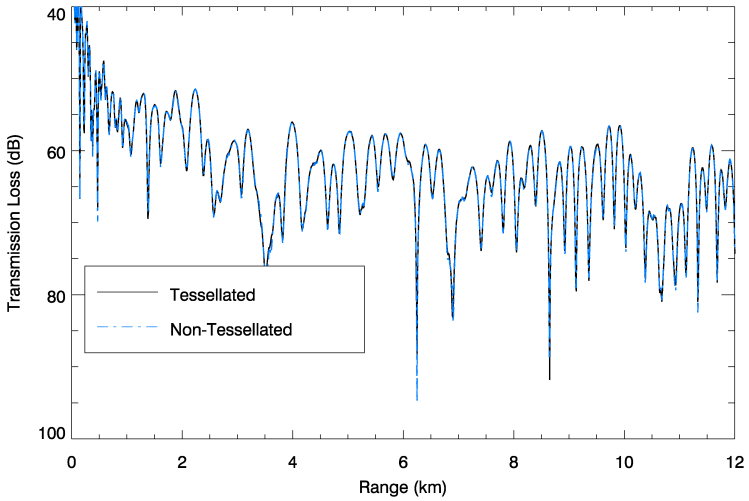

Figure A.7: Transmission loss as a function of range at 54 m depth in the source-receiver plane for the Florida Strait test environment.

Appendix B

Sediment Types for Florida Strait Test Environment: Dunham Classification

The definition of the Florida Strait Test Environment Model Case D was supported by piston core data [37], characterized based on sedimentological descriptions which referred to the modified Dunham classification. Broadly, the Dunham classification considers carbonates in terms of whether they are matrix- or grain-supported. The modified Dunham classification also takes grain size into account. Figure B (taken from the McNeill data report [37]) provides an overview of the classification. The measured p-wave velocities for the different sediment classifications are summarized in Figure B.

The information in the data report [37] have been reduced to the summary shown in Table B, grouped as 'near-shore' and 'in-plane' cores (refer to the map in Figure 5.9 from Section 5.2 for the locations of the numbered cores). The near-shore cores all contained a layer consisting of Rudstone and/or Floatstone. These are sediments made up with $> 10\%$ of components larger than 2 mm (e.g. coarse skeletal sand, gravel, shell fragments, coral fragments etc). These coarser grained sediments are characterized with high sound speeds and densities. In contrast, the in-plane cores consisted of finer grained layers of Packstone, Grainstone, Wackestone in various combinations (e.g. mud, fine skeletal sand etc). These sediments support lower velocity p-waves and have slightly lower density values compared to the sediments of the near-shore cores.

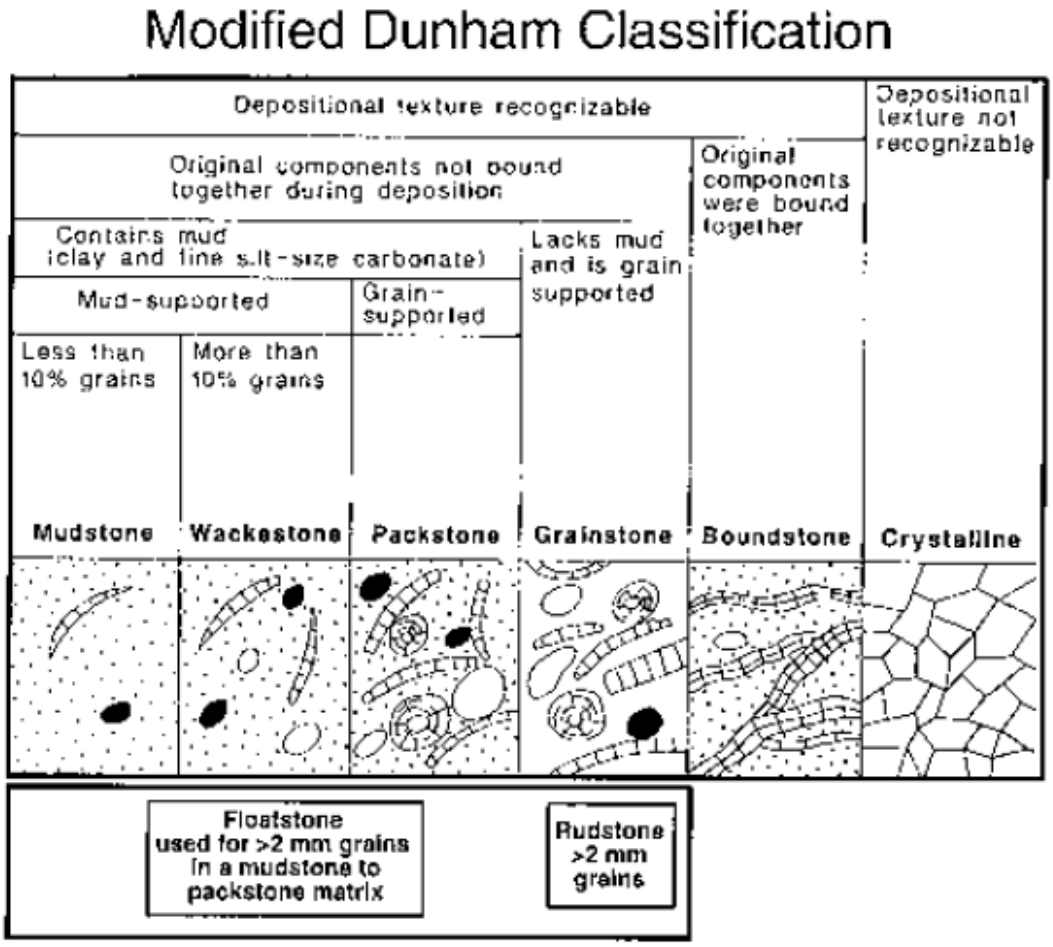

Figure B.1: Modified Dunham Classification for carbonate rocks. Source: McNeill, 2001.

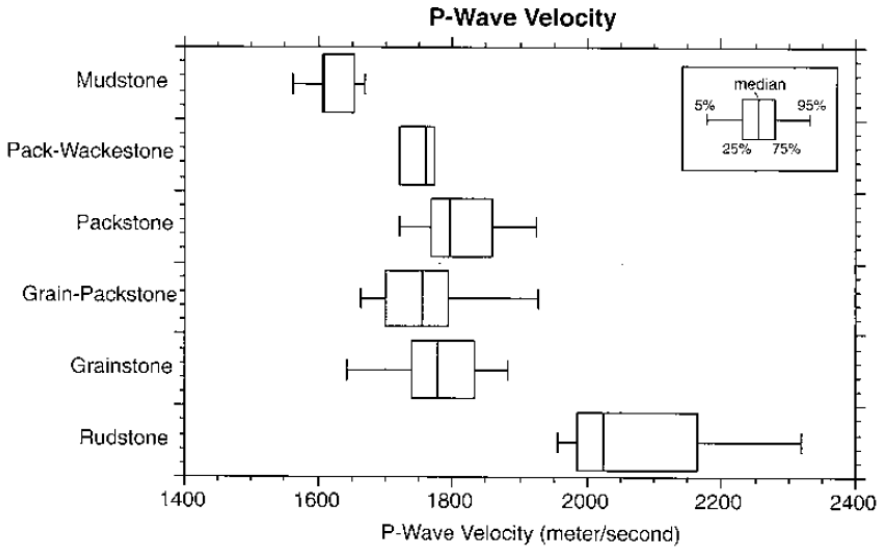

Figure B.2: P-wave velocities associated with the Modified Dunham Classification as measured from piston core samples. Source: McNeill, 2001.

	Core #	Munsell Color	Description* (depth range, in cm)	(nominal)		(just below mudstone)	
				c_p(m/s)	ρ (g/cm^3)	c_p(m/s)	ρ(g/cm^3)
Near-shore	1	light gray	M(6) / G(6-40) / R-F (40-70)	1900	1.96	1701	1.884
	4						
	7	light gray	M(2) / G (2-12) / R-F (12 - 32)	2050	2.06		1.831
	10	light gray	M(2) / G-R(2-9) / R-F (9-32)	2050	2.14	2027	2.09
	13	light gray	F(8) / G (8-30) / R (30-55)	1900	2.06	1797	1.963
	16	light gray / pale yellow	M (5) / G (5-28) / RF (28-65)	1900	2.16	1783	2.007
In-plane	2	pale green/pale olive/olive	M(8)/G(8-40)/W-P(40-83)/GP(83-300)	1775	1.97	1650	1.692
	5	pale olive/olive	M(10) / G(10-75) / P (75-250) / G (250-340)	1790	2.09	1676	1.779
	8						
	11						
	14	pale ylw/pale olive/ olive gray	M(8) / G (8-55) / P (55-230) / G (230-330)	1785	2.08	1754	1.713
	17						

* M = Mudstone, G = Grainstone, R-F = Rudstone-Floatstone, F = Floatstone, P = Packstone, W-P = Wackestone-Packstone, GP = Grainstone-Packstone

Figure B.3: Summary description of the near-shore and in-plane cores based on the McNeill data report[37].